

Investigation of the carbon dioxide sorption properties of selected organic macrocycles

By

Jeanice L. Basson

*Thesis presented in partial fulfilment of the requirements for
the degree of Master of Science*



UNIVERSITEIT
iYUNIVESITHI
STELLENBOSCH
UNIVERSITY

at
100
1918 · 2018

Stellenbosch University

Supervisor: Prof. Leonard J. Barbour
Faculty of Science
Department of Chemistry and Polymer Science

March 2018

Declaration

By submitting this thesis/dissertation electronically, I declare that the entirety of the work contained therein is my own, original work, that I am the sole author thereof (save to the extent explicitly otherwise stated), that reproduction and publication thereof by Stellenbosch University will not infringe any third party rights and that I have not previously in its entirety or in part submitted it for obtaining any qualification.

March 2018

Copyright © 2018 University of Stellenbosch

All rights reserved

This work is dedicated to my mother, Tanya Basson.

Acknowledgements

I would like to take this opportunity to thank the following people for their contribution to the work discussed in this dissertation:

First and foremost, I would like to thank my supervisor, Prof. Len Barbour, for the opportunity to be part of his research group. Thank you for the freedom to explore my own ideas in research. I have learned a great number of skills having had the chance to get practical experience on world-class instrumentation. With the wide range of equipment available to us, you have made sure to set no limits in research. I am grateful for the various opportunities that you created for attending conferences and workshops to broaden my knowledge on supramolecular chemistry. Thank you for your kindness, guidance and support. It has truly been a pleasure working in your research group.

I would also like to thank Dr Prem Lama for teaching me the ropes. Thank you for the countless editing of documents and for your patience both in and outside the lab. I knew I could always count on you to guide me in the right direction when I ran into problems in my research. You have been an amazing mentor and I have learnt so much from you.

Thank you to all my colleagues and friends in the Supramolecular Materials Research Group. I'm especially thankful to Charl Bezuidenhout, Marike du Plessis, Vincent Smith, Leigh Loots, Jan Costandius and Dewald van Heerden for their technical and moral support. I am grateful to my family, Tanya Basson, Greg Jessop, Dewald Basson, Jean Basson, Tahlita Nel and Ben Nel for their love and support throughout my MSc studies.

Finally, I would like to thank Stellenbosch University and the National Research Foundation for funding, without which this dissertation would not have been possible.

Abstract

The inclusion of guest molecules within host compounds has been an ever-growing interest in supramolecular chemistry. Host-guest chemistry has attracted much attention due to potential applications in drug delivery, catalysis and the separation and storage of natural gases. As a result, a large variety of porous systems such as porous coordination polymers (PCPs), porous molecular systems, covalent organic frameworks (COFs) and supramolecular organic frameworks (SOFs) have been developed. In this study, three well-known organic macrocycles, namely *p*-*tert*-butylcalix[4]arene (TBC4), cucurbit[6]uril (CB[6]) and cucurbit[8]uril (CB[8]) were investigated as hosts for gaseous carbon dioxide (CO₂). The aim of this study was to gain insight into the properties of these hosts and gain a better understanding of the inclusion of CO₂ in these materials.

The first section discusses TBC4 as a host for CO₂. The guest-free low density polymorph of TBC4 contains discrete pockets (zero-dimensional porosity) and captures CO₂ in a stepwise fashion. The system undergoes a gas-induced single-crystal to single-crystal (SC-SC) transformation to a more porous phase with an increased CO₂ loading capacity. The CO₂ inclusion compounds were investigated *in-situ* using single-crystal X-ray diffraction (SCXRD). The gas-induced phase transformation was further investigated using variable-pressure powder X-ray diffraction (VP-PXRD) and pressure-ramped differential scanning calorimetry (P-DSC). Interestingly, this porous phase is preserved when the CO₂ molecules are removed. However, the original guest-free phase can be regenerated under mild activation conditions. The study was extended by investigating CO₂ uptake by the high density polymorph of TBC4. Despite being a close-packed structure, CO₂ molecules are able to diffuse through the host to instigate a gas-induced transformation at high pressure, and a possible mechanism is discussed.

The second section describes the porosity of the well-known host, CB[6]. This host undergoes various phase transformations in order to produce a framework with permanent one-dimensional porosity. The various phases were subjected to thermal and structural analysis, where possible. This host, like most molecular organic hosts, produces a more close-packed phase when activated, and it expands upon CO₂ loading. The CB[6] host framework displays a large affinity for CO₂ and does not undergo a structural change at high CO₂ pressure. *In-situ* SCXRD was used to investigate the CO₂ inclusion compounds at various gas pressures to study the host-guest interactions.

The final section discusses CB[8] as a CO₂ adsorbent. Due to the high CO₂ affinity demonstrated by CB[6], CB[8] was studied as a solid-state host. This host undergoes a phase transformation during desolvation to produce a more stable polycrystalline phase of CB[8]. Although the host could not be characterized structurally, it was evident from the CO₂ sorption analysis that the host framework is porous. CB[8] displays stepwise uptake and release of CO₂ molecules and has a larger affinity for CO₂ as compared to methane and nitrogen gas. VP-PXRD was used to investigate the dynamic nature of the host with respect to CO₂ uptake and release. Several attempts at preserving the single crystallinity of CB[8] during desolvation are also discussed.

Opsomming

Die insluiting van gas molekules in gasheerverbindings is van belang in die area van supramolekulêre chemie weens verskeie potensiële toepassings. Hierdie toepassings sluit dwelm aflewering, katalise en die skeiding en berging van natuurlike gasse in. 'n Groot verskeidenheid poreuse sisteme soos poreuse koördinasie polimere (PCPs), poreuse molekulêre stelsels, kovalente organiese raamwerke (COFs) en supramolekulêre organiese raamwerke (SOFs) was ontwikkel om hierdie toepassings te bewerkstellig. In hierdie studie was drie bekende organiese makrosiklusse, naamlik *p*-tert-butielcalix[4]areen (TBC4), cucurbit[6]uril (CB[6]) en cucurbit[8]uril (CB[8]), ondersoek as gasheer vir koolstofdoksied (CO₂) gas. Die doel van hierdie studie was om eienskappe van hierdie gasheer in die vaste toestand te ondersoek en om die insluiting van CO₂ in hierdie materiale beter te verstaan.

In die eerste afdeling word TBC4 as 'n gasheer vir CO₂ bespreek. Die gasvry lae digtheid polimorf van TBC4 bevat diskrete porieë (nul-dimensionele porositeit) en absorbeer CO₂ stapsgewys. Die stelsel ondergaan 'n gas-geïnduseerde enkel-kristal (SC-SC) transformasie na 'n meer poreuse fase van TBC4 wat 'n verhoogde CO₂ laai kapasiteit het. Die CO₂-ingeslote verbinding was ondersoek *in-situ* deur gebruik te maak van enkel-kristal X-straal diffraksie (SCXRD) analise. Die gas-geïnduseerde fase transformasie was verder ondersoek deur gebruik te maak van drukversnelling poeier X-straal diffraksie (VP-PXRD) analise en drukversnelling differensiële skanderings kalorimetrie (P-DSC). Hierdie meer poreuse fase van TBC4 word behou selfs wanneer al die CO₂ molekules verwyder word. Die oorspronklike gasvrye fase kan egter onder ligte aktiveringstoestande geregenereer word. Die studie was uitgebrei deur ook die opname van CO₂ deur die hoë digtheid polimorf van TBC4 te ondersoek. Ten spyte van die feit dat dié polimorf geen porieë bevat nie, kan CO₂ molekules steeds deur die gasheer diffundeer om 'n gas-geïnduseerde transformasie by hoë druk in werk te stel. Moontlike meganismes was die opname van CO₂ deur die twee TBC4 polimorfe word bespreek.

Die tweede afdeling beskryf die porositeit van die bekende gasheer, CB[6]. Hierdie gasheer ondergaan verskeie fase transformasies om 'n raamwerk te skep met permanente een-dimensionele porositeit. Die enkel-kristal struktuur en termiese stabiliteit van die verskeie fases was, waar moontlik, geanaliseer. Hierdie gasheer, soos meeste molekulêre organiese gasheer, produseer 'n meer diggepakte fase wanneer dit geaktiveer word en brei weer uit wanneer dit met CO₂ gelaai word. Die CB[6] raamwerk toon 'n groot affiniteit vir CO₂ en

ondergaan geen strukturele verandering onder hoë CO₂ druk nie. *In-situ* SCXRD analise was gebruik om die CO₂-ingeslote verbindings by verskeie gasdruk te ondersoek om die gas-gasheer interaksies te bestudeer.

Die laaste afdeling bespreek CB[8] as 'n CO₂ adsorbens. As gevolg van die hoë CO₂ affiniteit wat deur CB[6] getoon word, het ons besluit om CB[8] as 'n potensiële gasheer vir CO₂ te ondersoek. Hierdie gasheer ondergaan 'n fase transformasie tydens die aktiveringsproses om 'n meer stabiele polikristallyne fase van die CB[8] te lewer. Alhoewel die gasheer nie struktureel gekenmerk kon word nie, was dit duidelik vanaf die CO₂ sorpsie analise dat die gasheerraamwerk poreus is. CB[8] vertoon 'n stapsgewyse opname en vrylating van CO₂ molekules en het 'n hoër affiniteit vir CO₂ gas in vergelyking met metaan gas en stikstof gas. VP-PXRD was gebruik om die dinamiese aard van die gasheerraamwerk te ondersoek onder verskillende drukke van CO₂. Die verskeie pogings om die kristalliniteit van CB[8] te bewaar tydens die aktiveringsproses word ook bespreek.

Publication

- J. L. Basson, P. Lama, L. J. Barbour, *Chem. Commun.*, **2017**, xyz. (in preparation)

Conference

- **ICCOSS XXIII – The 23rd International Conference on the Chemistry of the Organic Solid State**

Stellenbosch, South Africa, 2-7 April 2017

Poster presentation – J. L. Basson, P. Lama, L. J. Barbour, *INVESTIGATION OF THE INTERACTIONS BETWEEN CO₂ AND P-TERT-BUTYLCALIX[4]ARENE IN THE SOLID STATE.*

Abbreviations

0D	Zero-dimensional
1D	One-dimensional
2D	Two-dimensional
3D	Three-dimensional
ASU	Asymmetric unit
CB[6]	Cucurbit[6]uril
CB[8]	Cucurbit[8]uril
CIF	Crystallographic Information File
COFs	Covalent Organic Frameworks
CSD	Cambridge Structural Database
DSC	Differential Scanning Calorimetry
IR	Infrared Spectroscopy
MOF	Metal-Organic Framework
PCPs	Porous Coordination Polymers
P-DSC	Pressure-ramped Differential Scanning Calorimetry
PXRD	Powder X-ray Diffraction
SC-SC	Single-Crystal to Single-Crystal
sCO ₂	Supercritical carbon dioxide
SCXRD	Single-Crystal X-ray Diffraction
SOFs	Supramolecular Organic Frameworks
TBC4	<i>p</i> - <i>tert</i> -butylcalix[4]arene
TGA	Thermogravimetric Analysis
VP-PXRD	Variable-Pressure Powder X-ray Diffraction

Atomic color key



Hydrogen



Carbon



Oxygen



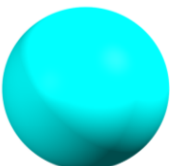
Nitrogen



Chlorine



Lead



Cadmium

Table of contents

Declaration.....	i
Acknowledgements.....	iii
Abstract.....	iv
Opsomming.....	vi
Publication.....	viii
Conference.....	viii
Abbreviations.....	ix
Atomic color key.....	x
Chapter 1 Introduction.....	1
1.1. Supramolecular chemistry.....	1
1.2. Crystal engineering.....	1
1.3. Intermolecular interactions.....	2
1.3.1. Hydrogen bonds.....	3
1.3.2. Coordination bonds.....	4
1.3.3. Dipole-dipole interactions.....	5
1.3.4. π - π interactions.....	5
1.3.5. Van der Waals interactions.....	6
1.4. Host-guest chemistry.....	7
1.4.1. Inclusion compounds.....	7
1.4.2. Selectivity.....	9
1.5. Crystal packing phenomena.....	9
1.5.1. Close packing.....	9
1.5.2. Supramolecular isomerism.....	10
1.5.3. Polymorphism.....	10
1.6. Porosity.....	11
1.7. Gas sorption.....	13
1.8. Single-crystal to single-crystal transformations.....	16
1.9. Aims.....	16

1.10. Thesis outline.....	17
References.....	19

Chapter 2 Experimental Techniques.....23

2.1. Single-crystal X-ray diffraction (SCXRD).....	23
2.2. Gas sorption.....	24
2.2.1. Volumetric sorption analysis	24
2.2.2. Gravimetric sorption analysis	25
2.3. Environmental gas cell	25
2.4. Powder X-ray diffraction (PXR)	26
2.5. Variable pressure PXR (VP-PXR).....	26
2.6. Thermogravimetric analysis (TGA)	27
2.7. Differential scanning calorimetry (DSC)	27
2.8. Pressure-ramped DSC (P-DSC)	27
2.9. Supercritical drying	28
2.10. Electron density calculations (SQUEEZE)	28
References.....	29

Chapter 3 *p-tert*-Butylcalix[4]arene.....30

3.1. Low density polymorph of <i>p-tert</i> -butylcalix[4]arene.....	32
3.1.1. Synthesis and crystallization	32
3.1.2. Structural analysis.....	32
3.1.3. Thermal analysis.....	34
3.1.4. Volumetric sorption analysis	35
3.1.5. Investigating the phase transformation.....	37
3.1.6. Structural analysis of the CO ₂ inclusion compounds	41
3.1.7. Structural analysis of the apohost.....	44
3.1.8. Proposed mechanisms for CO ₂ transport through the host.....	45
3.2. High density polymorph of <i>p-tert</i> -butylcalix[4]arene	46
3.2.1. Preparation of the high density polymorph of TBC4	46
3.2.2. Structural analysis.....	47
3.2.3. Thermal analysis.....	48
3.2.4. Interactions between the HDP of TBC4 and CO ₂	49

3.2.5.	Structural analysis of 1b_o under CO ₂ pressure	52
3.2.6.	Proposed mechanism for CO ₂ -induced phase transformation	53
3.3.	Summary.....	54
	References.....	56

Chapter 4 Cucurbit[6]uril58

4.1.	Synthesis and crystallization	60
4.2.	CB[6] hydrochloride hydrate.....	61
4.2.1.	Structural analysis.....	61
4.2.2.	Thermal analysis.....	63
4.3.	CB[6] hydrate	65
4.3.1.	Preparation of 3a	65
4.3.2.	Structural analysis.....	65
4.3.3.	Thermal analysis.....	67
4.3.4.	Activation of 3a to produce a porous material	68
4.4.	Porous CB[6].....	71
4.4.1.	Structural analysis.....	71
4.4.2.	Gravimetric sorption analysis	72
4.4.3.	Structural analysis of CO ₂ inclusion compounds	73
4.4.4.	Proposed mechanism for the uptake of CO ₂	75
4.5.	Summary.....	75
	References.....	77

Chapter 5 Cucurbit[8]uril78

5.1.	Synthesis and crystallization	78
5.2.	As-synthesized CB[8].....	79
5.2.1.	Structural analysis.....	79
5.2.2.	Thermal analysis	80
5.3.	Guest-free CB[8]	83
5.3.1.	Volumetric sorption analysis	84
5.3.2.	Phase transformations under gas pressure	85
5.3.3.	Proposed mechanism for CO ₂ uptake and release	86

5.4. Attempts to preserve the crystallinity of CB[8]	88
5.4.1. Supercritical drying	88
5.4.2. Solvent exchange	89
5.4.3. Recrystallization of CB[8] with different acids.....	90
5.4.4. Preserving the anionic species	92
5.5. Summary.....	96
References.....	98
Chapter 6 Concluding remarks	99
References.....	106
Appendix	107

Chapter 1

Introduction

1.1. SUPRAMOLECULAR CHEMISTRY

The term ‘supermolecule’ or ‘supramolecule’ was first introduced in 1937 to describe a hydrogen-bonded acetic acid dimer.¹ By then, the phenomenon of molecular association was known and had been studied for a long time. In 1967, Charles J. Pedersen² discovered that crown ethers have the ability to bind to certain alkali metal cations. Shortly thereafter Jean-Marie Lehn³ started his work on cation cryptands, followed by the discovery of cation spherands by Donald J. Cram⁴. In 1987 the Nobel Prize in Chemistry was awarded jointly to Cram, Lehn and Pedersen “*for their development and use of molecules with structure-specific interactions of high selectivity*”. Cram, Lehn and Pedersen thus became the “founding fathers” of the new field of supramolecular chemistry. Jean-Marie Lehn first termed supramolecular chemistry as “*the chemistry of molecular assemblies and of the intermolecular bond*” and later famously referred to it as “*chemistry beyond the molecule*”.⁵ Thus, supramolecular chemistry is the study of molecular assemblies held together by relatively weak, non-covalent interactions.

1.2. CRYSTAL ENGINEERING

Crystal engineering is the rational design of new materials with desired physical and chemical properties by applying the knowledge of supramolecular interactions.⁶ A crystal engineer uses molecules as building blocks in order to construct a packing arrangement resulting in specific material properties. Crystal engineers rely on the recurring patterns of intermolecular interactions between functional groups in order to predict the molecular packing arrangement.⁶ The repeating intermolecular motifs between functional groups of molecular components are referred to as supramolecular synthons (Figure 1).⁷ In essence, it is the combination of a set of supramolecular synthons that defines the crystal structure. It is important to understand the intermolecular interactions between molecular units so that they can be utilized during the design process to construct a functional material. Some of the most common intermolecular interactions are discussed in Section 1.3.

Chapter 1 - Introduction

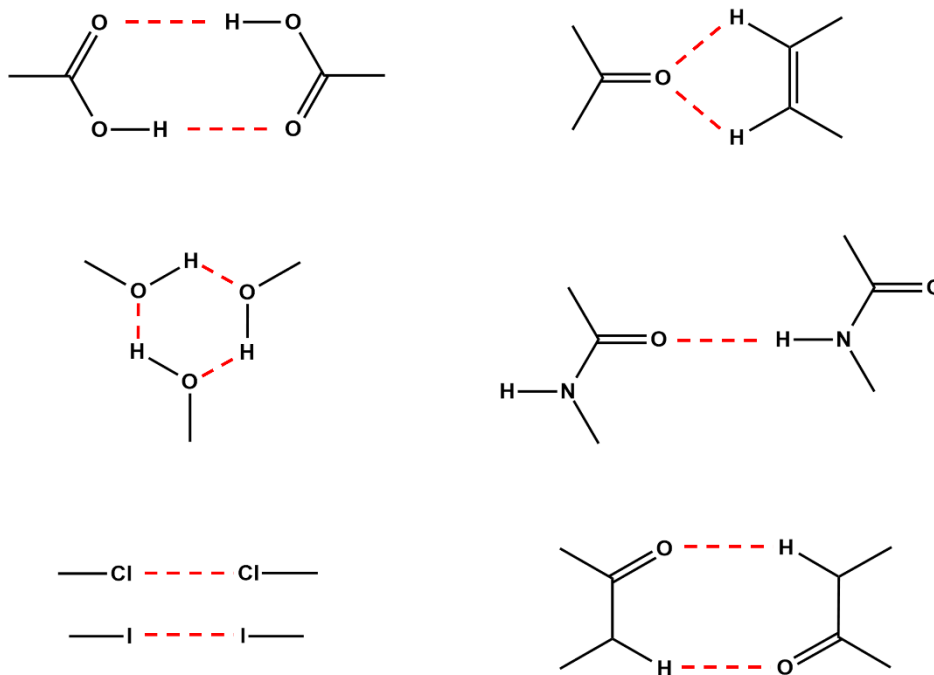


Figure 1. Examples of supramolecular synthons, as described by Desiraju.⁷

1.3. INTERMOLECULAR INTERACTIONS

Supramolecular chemistry is concerned with relatively weak non-covalent interactions, as opposed to the much stronger covalent interactions used in classical organic chemistry. The energies of non-covalent interactions (Table 1) are considerably lower than those associated with a covalent bond ($150\text{--}450\text{ kJ mol}^{-1}$).⁸ Although individual intermolecular interactions are weak, they become significant when considered in large numbers.

There are two groups of intermolecular interactions, namely medium-range isotropic (non-directional) forces and long-range anisotropic (directional) forces. Isotropic forces include $\text{C}\cdots\text{C}$, $\text{H}\cdots\text{H}$ and $\text{C}\cdots\text{H}$ interactions that define the shape, size and close packing of molecules. On the other hand, anisotropic/electrostatic forces occur between partially charged heteroatoms (oxygen, nitrogen, phosphorus, sulphur and chlorine) as well as between partially charged heteroatoms and carbon or hydrogen atoms.⁹ Intermolecular interactions are considered important synthons in crystal engineering. Some of these interactions are listed in Table 1.

Table 1. Strengths of intermolecular interactions.

Intermolecular interaction	Strength (kJ mol ⁻¹)	Interaction type
Hydrogen bonds	4-120	Anisotropic
Coordination bonds	50-200	Anisotropic
Dipole-dipole interactions	5-50	Anisotropic
π - π interactions	0-50	Isotropic
van der Waals interactions	< 5*	Isotropic

* This value may vary depending on the surface areas of the molecules. Table reproduced from Steed *et al.*⁸

1.3.1. Hydrogen bonds

It has been said that the hydrogen bond is perhaps the most important intermolecular interaction in terms of crystal engineering due to its strength and directionality.⁸ The significance and extensive occurrence of the hydrogen bond was well-known before it was first described as a weak bond by Latimer and Rodebush in 1920.¹⁰ They proposed that a lone pair of electrons on one water molecule could exert a force on a hydrogen atom of another water molecule to bind the molecules together. However, it was only with the publication of Linus Pauling's book *The Nature of the Chemical Bond*,¹¹ in 1939, that this phenomenon was described as hydrogen bonding. Furthermore, Pauling described that the hydrogen atom, with only one stable orbital, can only form one covalent bond, and as a result the hydrogen bond must be due to ionic forces between the involved species.

For many years the hydrogen bond was considered to occur with only highly electronegative atoms, excluding bonding to groups of atoms. A new definition of what constitutes a hydrogen bond appeared in 2011 as the outcome of an IUPAC project: "*The hydrogen bond is an attractive interaction between a hydrogen atom from a molecule or a molecular fragment, X-H...A in which X is more electronegative than H, and an atom or group of atoms in the same or different molecule (A), in which there is evidence of bond formation*".¹² In this definition a hydrogen atom covalently bonded to X is attracted to A and acts as a bridge between X and A. The strongest hydrogen bonds occur when X and A are highly electronegative. However, relatively weaker hydrogen bonding interactions such as C-H...O, C-H...N and C-H... π can exist when X and A are less electronegative. Hydrogen bonds vary in strength between 4 and 120 kJ mol⁻¹, with the majority being under 60 kJ mol⁻¹.⁸

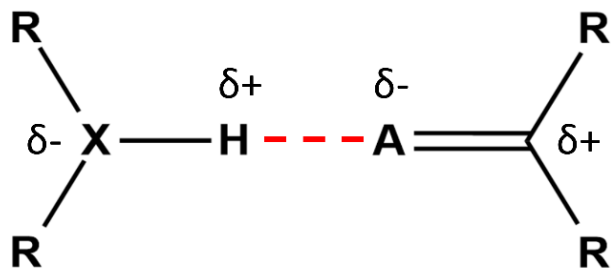


Figure 2. A hydrogen bond formed by two molecular fragments, wherein HXR_2 acts as the hydrogen bond donor and AR_2 acts as the hydrogen bond acceptor.

1.3.2. Coordination bonds

A coordination bond arises from ion-dipole interactions between a metal cation and an organic ligand. In this interaction, the organic ligand donates an electron pair to the metal cation in order to form a bond. Coordination bonds are the strongest directional non-covalent interactions and typically range between $50\text{-}200\text{ kJ mol}^{-1}$ depending on the species involved.⁸ Due to the strength and rigidity of these directional bonds they are an important tool for crystal engineers in constructing coordination polymers and metal-organic frameworks (MOFs) (see Section 1.6.2).^{13,14} The coordination bonds present in a lead-based MOF are indicated in Figure 2.

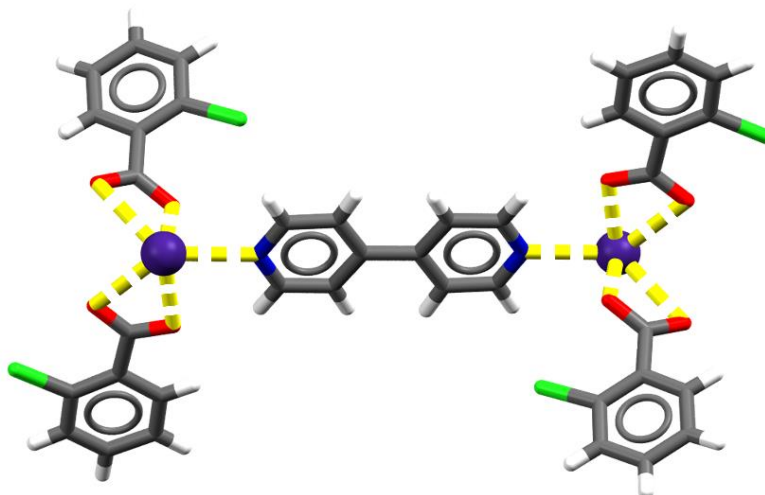


Figure 3. Coordination bonds between Pb(II) (purple sphere) and the nitrogen atom of a 4,4'-bipyridine linker and the carboxylate of 2-chlorobenzoate molecules are indicated as dashed yellow lines.

1.3.3. Dipole-dipole interactions

Dipole-dipole interactions are directional interactions between molecules with a permanent electric dipole moment. A molecule or group with a partial positive charge is stabilized by an adjacent molecule or group with a partial negative charge. The strength of the interaction depends on the species involved as well as the distance between them, and the relative orientation of their dipoles.¹⁵ Although dipole-dipole interactions are the weakest among directional interactions, they play an essential role in the alignment of molecular species. Figure 4 displays two common arrangements of CO₂ molecules as a result of dipole-dipole interactions.

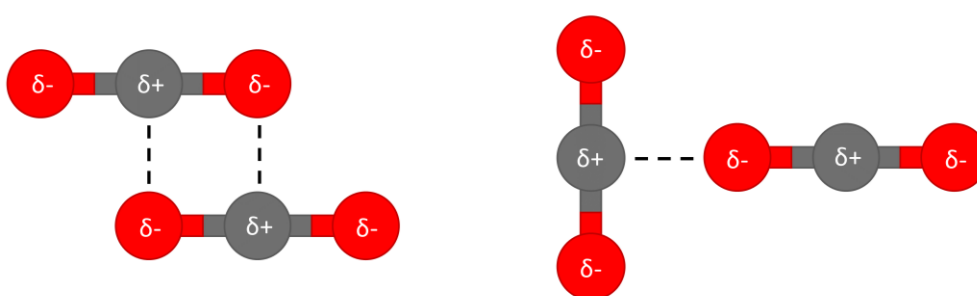


Figure 4. The slipped-parallel (left) and T-shaped (right) arrangement of two CO₂ molecules as a result of dipole-dipole interactions.

1.3.4. π - π interactions

Benzene has a strong quadrupole moment owing to the negatively charged π -electron clouds above and below the ring, and the positively charged C-H dipoles in the σ -framework. The attraction between the electron cloud of one molecule and the framework of another molecule results in weak, non-directional π - π interactions.¹⁶ These interactions are only favorable when the π - σ attraction is larger than the π - π repulsion between the molecules.

The most common types of π - π interactions include face-to-face, offset face-to-face and edge-to-face interactions. In face-to-face and offset face-to-face interactions, the aromatic rings are arranged parallel to each other in a stacked or offset fashion, respectively. When the center of a ring is arranged perpendicular with respect to a hydrogen atom from another ring, the interaction is said to be edge-to-face. The different types of π - π interactions are illustrated in Figure 5.

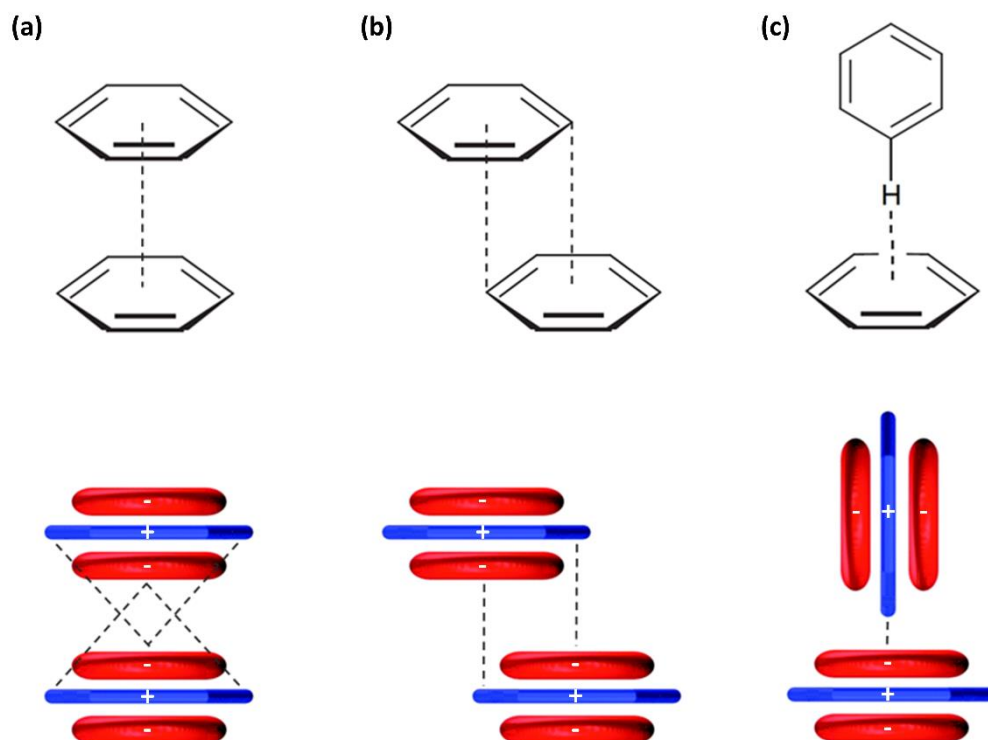


Figure 5. (a) Face-to-face, (b) offset face-to-face and (c) edge-to-face π - π stacking arrangements of aromatic rings. The quadrupole moments of the benzene molecules are used to show the interactions for each arrangement. Images adapted from Ikkanda *et al.*¹⁶

1.3.5. Van der Waals interactions

Van der Waals forces or London dispersion forces are weak, non-directional interactions between momentary or permanent electric dipole moments of uncharged species.¹⁷ When molecules move in close proximity to each other, the electron cloud of one species can induce a momentary dipole in a neighboring molecule by means of electron cloud repulsion or attraction (Figure 6). The strengths of these forces are dependent on the polarizability of the molecule and are only significant when the molecules are very close to each other. As a result, these forces are not so important when it comes to supramolecular design, but play a significant role in the formation of inclusion compounds, which will be discussed in Section 1.4.1.

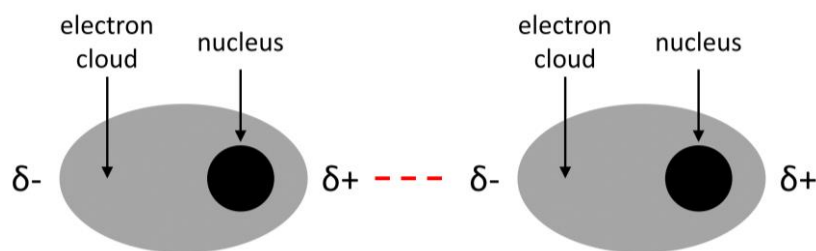
Chapter 1 - Introduction

Figure 6. The attraction between two neighboring molecules due to a temporary dipole moment caused by the shift in electron density around the nuclei. Figure reproduced from Steed *et al.*⁸

1.4. HOST-GUEST CHEMISTRY

When a molecular system is capable of trapping smaller guest molecules it is referred to as a host. Host molecules can be divided into two broad categories: (1) those that trap guests in molecular cavities and (2) those that trap guests in cavities present between host molecules.¹⁸ The resulting host-guest complex is called an inclusion complex. Cage inclusion complexes, where the guest molecules are enclosed on all sides by the host, are more specifically referred to as clathrates.¹⁹ Originally only organic systems were considered as hosts, since the known hosts at that time were naturally occurring biological systems such as copolymers of phosphoric acids and of α -amino acids.²⁰ Pedersen's work on crown ethers later inspired the expansion of inclusion compounds to include inorganic hosts.

1.4.1. Inclusion compounds

Inclusion compounds are usually formed when the host crystallizes from a solvent that can act as a guest molecule. This can be achieved through the method of slow evaporation of the solvent. The formation of an inclusion compound often depends on the temperature and the pressure. In some cases, hydrothermal or solvothermal methods have been used.²¹ In these methods, the host material and solvent are mixed and placed in a Teflon-lined autoclave. The autoclave is then heated at elevated temperature and pressure to increase the solubility of the material, which, upon cooling can form an inclusion compound.

Cucurbit[n]urils, calix[n]arenes and metal-cyclam complexes are well-known host materials. Figure 7 contains examples of the inclusion compounds formed by these hosts. Cucurbit[7]uril (CB[7]) is an example of a host that is capable of trapping guest molecules in its molecular cavity. CB[7] forms two crystallographically independent CB[7]/ferrocene complexes with different relative alignments of the guest inside the macrocyclic cavity.²²

Chapter 1 - Introduction

Similarly, the large cavity present in the bowl of a calix[5]arene derivative is capable of housing a C₆₀ fullerene molecule.²³ Unlike the previous two examples, a Ni(II)-based dioxocyclam complex lacks molecular cavities and traps water molecules in spaces present between the host molecules.²⁴

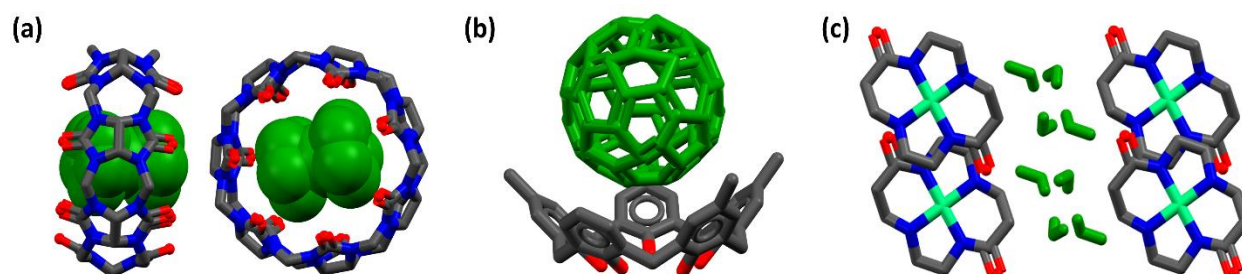


Figure 7. Inclusion complexes formed by (a) cucurbit[7]uril and ferrocene,²² (b) a calix[5]arene derivative and C₆₀ fullerene²³ and (c) a nickel(II)-dioxocyclam complex and water.²⁴

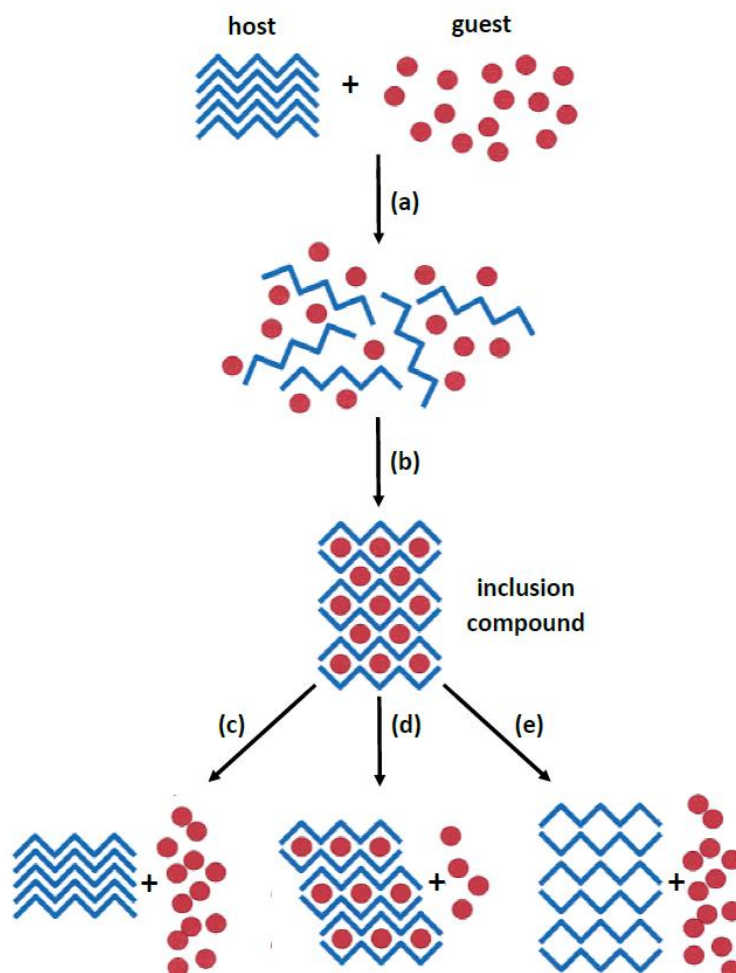


Figure 8. The formation and possible decomposition routes of an inclusion compound (a-e). Figure adapted from Nassimbeni.¹⁸

Chapter 1 - Introduction

Nassimbeni described the formation and possible decomposition routes of an inclusion compound (Figure 8)¹⁸ as taking place in two steps: (a) the host molecules are dissolved in a guest solvent and (b) a host-guest complex is formed upon crystallization. Once removed from solution the inclusion complex may either stay intact or decompose. The latter could (c) decompose to yield the original host excluding the guest molecules, (d) partially decompose to produce a new phase of the complex or (e) lose the guest molecules to yield an empty host structure.

1.4.2. Selectivity

In 1977 Cram defined a host-guest relationship as “*a complementary stereoelectronic arrangement of binding sites in (the) host and guest*”.²⁵ Thus, the host must have a suitable binding site to promote favorable intermolecular interactions with guest molecules in the cavities. A host can display a degree of selectivity towards a particular guest or family of guests. This is an important application of host-guest chemistry since a mixture of compounds can be separated based on the selectivity of the host.

The selectivity of a host depends on a number of different factors. For strong and selective binding to occur the binding site of the host must be complementary to that of the guest. In other words, the binding sites need to be similar in size and shape as well as electronically stabilizing. An example of this can be obtained from the hard-soft acid-base (HSAB) theory,²⁶ where hard metal cations show selectivity towards functional groups with hard oxygen atoms as opposed to softer nitrogen atoms. Preorganization of the host also plays a role in the selectivity. Rigid hosts containing cavities that are already of the correct size and shape to bind to guest molecules are preferred, since no energetic change in conformation is required. Most macrocycles can act as host molecules due to their rigidity and intramolecular cavities.

1.5. CRYSTAL PACKING PHENOMENA

1.5.1. Close packing

In the solid state, molecules tend to arrange themselves to minimize the void space between them and also to maximize the interactions with neighboring molecules.²⁷ Short to medium range isotropic forces are responsible for the close packing of molecules, where van der Waals interactions play the largest role. As the number of interactions between the molecules

Chapter 1 - Introduction

increases, the lattice energy of the structure decreases to produce a more stable packing arrangement.²⁸

The principle of close-packing typically defines the arrangement of molecules in the solid state. However, close-packing does not usually occur when there are strong directional interactions such as hydrogen bonds present between the molecules.¹² The principle of close-packing also fails when the molecules have an irregular shape that prevents efficient packing.²⁹ Strong non-covalent interactions are kinetically favored, whereas close-packed arrangements lead to thermodynamically favored products.¹²

The packing efficiency of a crystal refers to the volume occupied by atoms relative to the total crystal volume. The maximum packing efficiency that can be achieved for spheres in three-dimensional space is 74%.³⁰ This value usually ranges between 60-65% for organic molecules.³⁰ An increase in a crystal density of a given sample is also a good indication of a higher packing efficiency.

1.5.2. Supramolecular isomerism

Supramolecular isomerism, similar to structural isomerism at molecular level, refers to the existence of more than one network structure for the same chemical composition.³¹ This phenomenon is often encountered in organic molecules, since the individual molecules are held together by relatively weak intermolecular interactions with similar energy potentials between the isomeric structures. Coordination polymers, on the other hand, are made up of stronger coordination bonds and are therefore mostly encountered in the lowest energy form.³¹ Supramolecular isomers have been categorized into four different classes, namely structural, conformational, catenane and optical isomerism.³¹ Structural isomerism occurs when the same building block produces different network structures with the same empirical formula. Conformational isomerism occurs when different conformations of flexible ligands produce different superstructures, whereas catenane and optical isomerism are related to different degrees of interpenetration and different chirality, respectively.³¹

1.5.3. Polymorphism

Polymorphism can be described as a subset of supramolecular isomerism. It occurs when a solid material with a certain same chemical composition can exist in more than one stable packing arrangement, thus producing different possible crystal structures or phases.^{30,32} This

Chapter 1 - Introduction

definition excludes different solvates of a host compound. However pseudopolymorphism³² is used to describe polymorphs with a different number of solvent molecules, or various solvates of the host. When the same host produces different crystal structures with the same guest they are referred to a solvatomorphs.³³ It often occurs that a solid phase can convert to another phase at a specific temperature and/or pressure (inversion point),³⁴ and this is known as a polymorphic transition.

Many examples of polymorphism can be found in the literature: The Crystallographic Structural Database (CSD) contained 26 299 entries of polymorphs as of May, 2017.³⁵ New polymorphs of existing compounds are still being discovered. For example, the structure of thiosaccharin was first published in 1994.^{36a} In 2017, it was discovered that this compound undergoes a polymorphic transformation upon heating and cooling to produce two new phases^{36b} (Figure 9). Knowledge of polymorphism is important because a subtle change in the crystal structure may result in different solid-state properties.

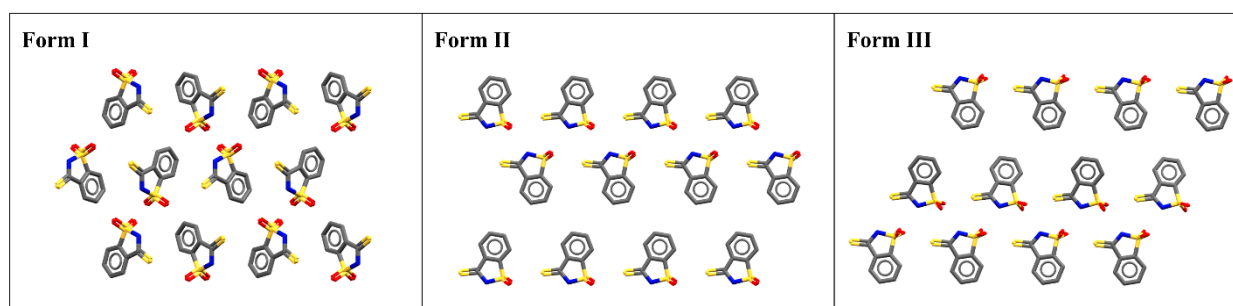


Figure 9. The three known polymorphic forms of thiosaccharin.^{35, 36}

1.6. POROSITY

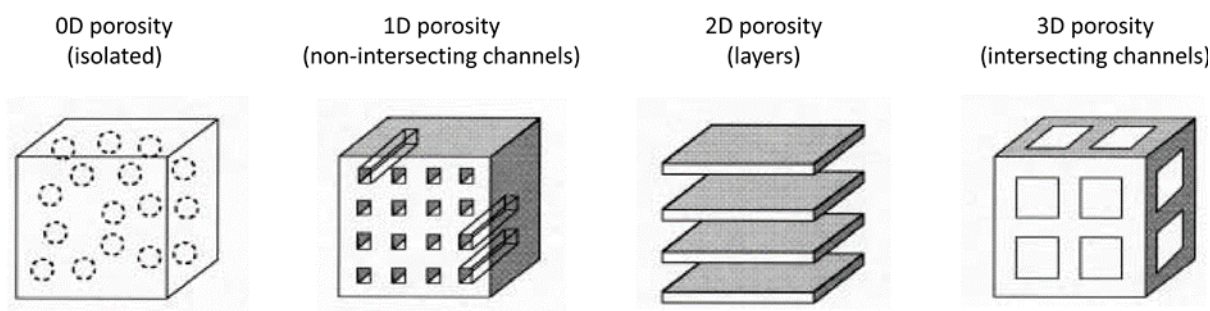
Molecules in the solid state tend to arrange in a close-packed fashion to maximize favorable intermolecular interactions. For this reason, porosity in the solid state is a rare occurrence and molecular crystals seldom contain lattice voids larger than 25 Å³.³⁷ Despite this, the number of supramolecular compounds that exhibit porosity is still increasing. A material is said to be porous when (1) it contains pores such as cavities, voids or channels that are penetrable by guest molecules and (2) the host phase remains largely unaffected by guest uptake and removal.³⁸ In other words, the term “porous” refers to the host framework and no longer applies when framework integrity is lost to produce an amorphous collection of host molecules. Porous materials can be described according to their pore size (Table 2).

Chapter 1 - Introduction

Table 2. Description of porous material based on their pore size.³⁹

Description of pores	Pore size (Å)
Ultramicropore	< 5
Micropore	5-20
Mesopore	20-500
Macropore	> 500

Kitagawa *et al.* have also suggested that porosity can be classified into four possible categories based on spatial dimensionality (Figure 10).³⁹ Zero-dimensional (0D) cavities are isolated by surrounding molecules and are only accessible by guest molecules if the host framework is flexible enough to allow the movement of the guests through the framework. One-dimensional (1D) porosity refers to non-intersecting channels, while two-dimensional (2D) and three-dimensional (3D) porosity respectively refers to layers and intersecting channels within the framework.

**Figure 10.** Classes of porous structures based on spatial dimensions. Figure adapted from Kitagawa *et al.*³⁹

Porous materials have attracted much attention due to their potential applications, such as the separation and storage of industrial by-products,⁴⁰ separation and removal of hazardous chemicals,⁴¹ storage of methane and hydrogen gas as synthetic fuel,⁴² carbon capture and sequestration,⁴³ drug delivery systems⁴⁴ as well as heterogeneous catalysis.⁴⁵ Various kinds of porous materials, such as activated carbon, zeolites, coordination polymers and MOFs, crystalline organic materials, amorphous polymeric organic materials, supramolecular organic frameworks (SOFs), and covalent organic frameworks (COFs), have been developed to realize the abovementioned applications.

Until the mid-1990s the majority of known porous materials consisted of carbon and inorganic-based systems, such as activated carbon and zeolites.³⁹ Over the past decade the

Chapter 1 - Introduction

focus has shifted to highly porous coordination polymers (PCPs) and MOFs, which have been shown to have a higher storage capacity than activated carbons and zeolites.⁴⁶ Molecular compounds have received much less attention as porous systems as compared to PCPs and MOFs. This is mainly due to difficulties associated with predicting the packing arrangement of discrete molecules. Porous organic systems also tend to collapse after the removal of guest molecules to yield amorphous or close-packed systems. Nonetheless, several organic crystals that maintain their crystal porosity after guest removal have been reported.⁴⁷

In recent years there has been renewed interest in porous organic systems. Researchers in the area of host-guest chemistry have worked towards engineering covalent organic frameworks (COFs) and supramolecular organic frameworks (SOFs). COFs are extended organic solids that consist of rigid organic building blocks linked by covalent bonds.⁴⁸ These frameworks are highly designable and several porous organic cages have been synthesized using this approach.⁴⁸ SOFs are a type of porous material in which rigid organic building blocks are held together by non-covalent interactions such as van der Waals interactions, C-H \cdots π interactions, π - π stacking and hydrogen bonding.⁴⁹ These building blocks need to be carefully designed in order to ensure that the framework is porous in nature. Organic macrocycles such as cyclodextrins,⁵⁰ calix[n]arenes,⁵¹ cucurbit[n]urils⁵² and pillar[n]arenes⁵³ have been used to construct highly porous SOFs that display both intrinsic (within the molecules) and extrinsic (between the molecules) pores. Typically, a material displays either intrinsic or extrinsic porosity, but seldom both.⁵⁴ However, the use of bulky substituent groups in the design of porous organic systems has proven to be a useful method in generating additional extrinsic pores between intrinsically porous molecules.⁵⁴

1.7. GAS SORPTION

Gas sorption can occur via two processes, namely chemisorption and physisorption. Chemisorption refers to the adhesion of gas molecules to a surface of a solid through covalent bonds, while physisorption involves the formation of non-covalent bonds between the material and gas molecules.⁵⁵ Adsorption occurs when the gas molecules are in contact with the surface layer of the sample. When the gas molecules penetrate the surface layer and enter the pores of the solid, the process is referred to as absorption. It is often found that a material displays both adsorption and absorption of a particular gas, and the collective uptake is then referred to as sorption.⁵⁵

Chapter 1 - Introduction

The amount of gas taken up by a material at a specific temperature can be described quantitatively by a sorption isotherm, which is a graphical representation of the amount absorbed as a function of equilibrium pressure. There are two known methods for determining sorption isotherms, namely volumetric and gravimetric. In the volumetric method the amount of gas taken up by a sample in a confined space of known volume is isothermally measured until an equilibrium pressure is reached. Gravimetric methods make use of a microbalance to directly measure the change in weight of the sample as the gas pressure is increased and decreased at a constant temperature.

The International Union of Pure and Applied Chemistry (IUPAC) describes six types of adsorption isotherms (Figure 11) that are characteristic of microporous (type I), macroporous and nonporous (types II, III, VI) and mesoporous (type IV, V) materials.⁵⁵ The type I (Langmuir) isotherm, is a reversible concave isotherm that approaches a maximum adsorption value at high pressure. The reversible type II isotherm represents unrestricted adsorption and does not approach a limiting value. The type III isotherm is reversible and convex over its entire pressure range. The adsorption and desorption curves do not coincide in the type IV isotherm, resulting in a characteristic adsorption hysteresis loop. The type V isotherm also contains a hysteresis loop and is rarely observed. Lastly, the type VI isotherm represents stepwise adsorption in which each step is highly dependent on the adsorbent as well as the temperature of the sorption analysis.

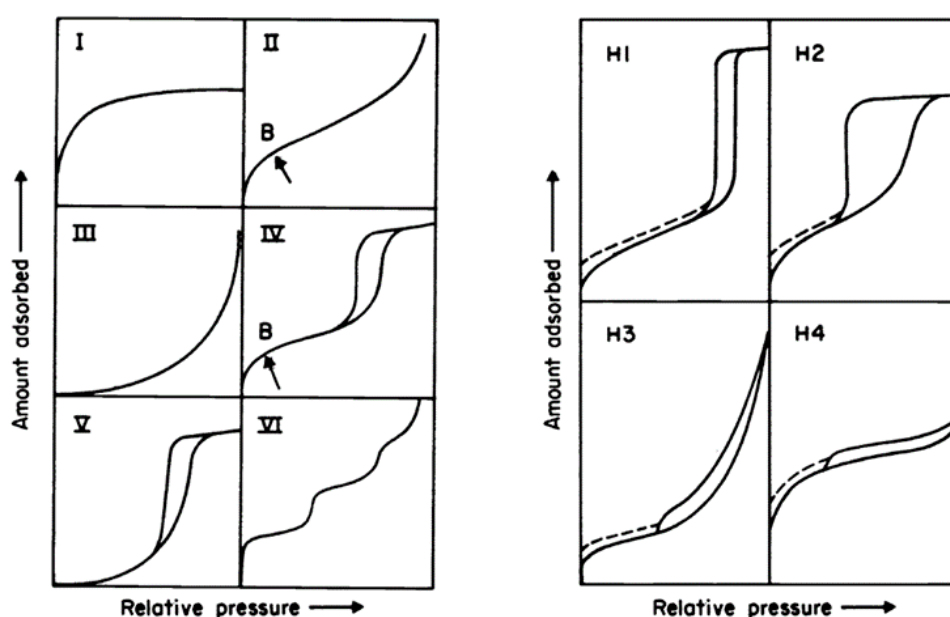


Figure 11. The six types of physisorption isotherms (left) and the four types of hysteresis loop.⁵⁵

Chapter 1 - Introduction

It is widely accepted that there is a correlation between the pore characteristics (size, geometry, distribution and connectivity) of a material and the shape of the hysteric loop.⁵⁶ As a result, hysteresis loops can exhibit a variety of shapes. Figure 11 represents the four IUPAC categories of hysteric loops (H1-H4). Type H1 and H4 have been classified as the extreme types, where type H2 and H3 are the intermediates between these extremes.⁵⁵

The six types of isotherms depicted in Figure 11 are only applicable to systems where the host framework remains unchanged during the sorption process.³⁹ It often occurs that hosts with flexible frameworks undergo a structural transformation during adsorption in order to accommodate more guest molecules. The resulting isotherm cannot be categorised as one of the six isotherms defined by IUPAC,⁵⁵ but it is usually a combination of types I, II or III.³⁹ The sorption isotherm observed when a nonporous framework undergoes a structural transformation to a microporous framework is shown in Figure 12. At low pressure, the adsorption isotherm follows the conventional type II isotherm until point A is reached. Thereafter a sudden increase in adsorption is observed as the isotherm converts to a type I isotherm. This occurs due to the structural transformation from a nonporous to a microporous system. At point B, the transformation is complete and will reach a saturation value as the pressure is further increased. A multistep adsorption profile is observed if more than one structural transformation occurs.

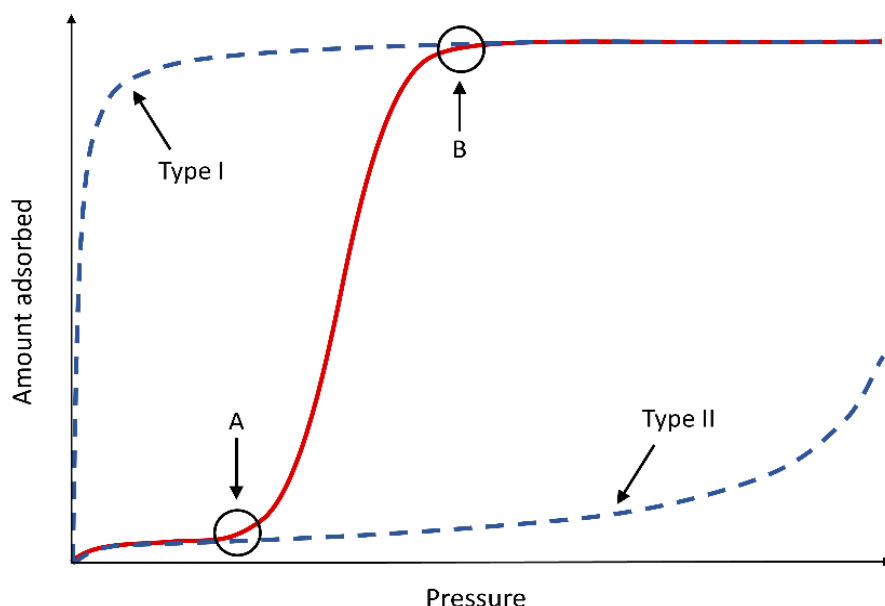


Figure 12. The isotherm of a non-porous framework indicating a structural transformation to a microporous system during adsorption (red). The conventional type I and type II isotherms that make up the adsorption isotherm are indicated as blue dashed lines. Points A and B represent the start and end points of the structural transformation, respectively. This figure was adapted from Kitagawa *et al.*³⁹

1.8. SINGLE-CRYSTAL TO SINGLE-CRYSTAL TRANSFORMATIONS

Atoms in the crystalline solid state are considered to be stationary, with only slight vibrational movement about their equilibrium positions.⁵⁷ Interestingly, induced structural reorganization in the solid state can occur as a result of a chemical or physical stimulus. Provided the molecules cooperate in a concerted fashion, and the mechanical stress accompanied by this structural reorganization is bearable, the crystals often maintain their mosaicity.⁵⁷ When a significant change in the crystal structure occurs without the loss of single crystallinity, this transition is referred to as a single-crystal to single-crystal (SC-SC) transformation.⁵⁸ During this process the integrity of the single crystal is maintained. A number of examples of SC-SC transformations exist in the literature.⁵⁹ However, in most cases a significant change in crystal structure results in the loss of crystallinity. SC-SC transformations are important since the changes in the solid-state material from the initial to the final phase can be directly visualized by means of single-crystal X-ray diffraction (SCXRD) analysis.

1.9. AIMS

The development of new porous materials for the separation and storage of gases such as CO₂, hydrogen, methane and acetylene has been an ever-growing interest in supramolecular chemistry. Materials traditionally used for the sorption of gases include zeolites and activated carbon. However, the focus has shifted to more flexible and dynamic porous systems that show selective separation. Although much research has focused on development of PCPs, they are often toxic due to the presence of metal ions,⁶⁰ expensive to synthesize, and sensitive to water,⁶¹ which limits their application. In contrast, organic systems are often synthesized from inexpensive starting materials and are stable in the presence of water.⁶¹ Several organic materials are known to form guest inclusion complexes with CO₂ and a large number of organic materials exhibit CO₂ storage capacities that compete with PCPs.⁶²

The uptake and storage of CO₂ in well-known organic macrocycles was investigated and is discussed in this dissertation. The overall aim of this study was to gain insight into the confinement of CO₂ molecules in organic materials. We sought to gain a better understanding of the host structures by analyzing the structural and thermal properties of each of the materials. The uptake and release of CO₂ molecules by each host was investigated by means of sorption processes and the effects of gas-induced structural transformations were further

Chapter 1 - Introduction

explored. SCXRD techniques allowed us to investigate changes in the solid-state materials during SC-SC transformations. The inclusion of CO₂ molecules in the host frameworks was studied using *in-situ* SCXRD analysis with the aim of understanding the host-guest interactions present in the inclusion compounds.

1.10. THESIS OUTLINE

In order to understand the systems reported in this dissertation various experimental techniques such as single-crystal X-ray diffraction, gas sorption, powder X-ray diffraction, pressure-ramped differential scanning calorimetry and thermal analysis have been used. **Chapter 2** contains a description of these techniques and the instrumentation that was used to conduct this research.

Chapter 3 describes both the low density and high density polymorphs of the well-known organic host, *p-tert*-butylcalix[4]arene (TBC4). The low density polymorph of TBC4 is known to accommodate CO₂ molecules in both intrinsic and extrinsic pores. TBC4 is an excellent candidate for studying weak interactions with gaseous CO₂ in the solid state due to the simplicity of the discrete pockets that are present in the crystal structure. The host framework undergoes a SC-SC transformation during the uptake of CO₂ to produce a different form that was studied in detail. This study was extended by re-investigating the high density polymorph of TBC4 under CO₂ pressure and demonstrates how a close-packed non-porous structure can be conditioned to produce a porous material.

Chapter 4 deals with the porosity of cucurbit[6]uril (CB[6]) with respect to the uptake of CO₂ gas. Upon activation, CB[6] undergoes a phase transformation to produce a highly stable phase. This is an example of a rigid host framework with permanent 1D channels. The rigidity of CB[6] allows the structure to remain unchanged during CO₂ adsorption. The activated form is particularly interesting due to its high CO₂ storage capacity. The previously reported CO₂ inclusion compounds were re-investigated using *in-situ* SCXRD analysis in order to gain a better understanding of the high CO₂ affinity of this host.

In **Chapter 5**, the porous nature of another member of the cucurbit[n]uril family, cucurbit[8]uril (CB[8]), was studied. A new polycrystalline phase of CB[8] was obtained during the activation of the as-synthesized material. The activated form is dynamic and shows breathing behaviour during CO₂ sorption.

Chapter 1 - Introduction

Chapter 6 provides a summary of the outcomes of this work and concluding remarks. Suggestions regarding future work are also provided.

REFERENCES

1. Wolf, K. L.; Frahm, F.; Harms, H. *Z. Phys. Chem. Abt. B.* **1937**, *36*, 17.
2. Pederson, C. J. *J. Am. Chem. Soc.* **1967**, *89*, 7017.
3. Lehn, J.-M. *Pure Appl. Chem.* **1978**, *50*, 871.
4. Trueblood, K. N.; Knobler, C. B.; Maverick, E.; Helgeson, R. C.; Brown, S. B.; Cram, D. *J. Am. Chem. Soc.* **1981**, *103*, 5594.
5. Lehn, J.-M. *Angew. Chem. Int. Ed.* **1988**, *27*, 89.
6. Desiraju, G. R. *Crystal Engineering, the Design of Organic Solids*; Elsevier: Amsterdam. 1989.
7. Desiraju, G.R. *Angew. Chem. Int. Ed.* **1995**, *34*, 2311.
8. Steed, J. W.; Turner, D. R.; Wallace, K. J. *Core Concepts in Supramolecular Chemistry and Nanochemistry*; John Wiley & Sons, Ltd: West Sussex, U.K., 2007.
9. Desiraju, G. R. *Nature.* **2001**, *412*, 397.
10. Latimer, W. M.; Rodebush, W. H. *J. Am. Chem. Soc.* **1920**, *42*, 1419.
11. Pauling, L. *The Nature of the Chemical Bond*; Cornell University Press: Ithaca, NY, U.S.A. 1939.
12. Desiraju, G. R. *J. Am. Chem. Soc.* **2013**, *135*, 9952.
13. James, S. L., *Chem. Soc. Rev.* **2003**, *32*, 276.
14. Hosseini, M. W., *CrystEngComm* **2004**, *6*, 318.
15. Muller, P. *Pure & Appl. Chem.* **1994**, *66*, 1107.
16. Ikkanda, B. A.; Iverson, B. L. *Chem. Commun.* **2016**, *52*, 7752.
17. Stone, A. J. *The Theory of Intermolecular Forces*; Clarendon Press: Oxford, U.K., 1996.
18. Nassimbeni, L. R. *Acc. Chem. Res.* **2003**, *36*, 631.
19. Moss, G. P.; Smith, P. A. S.; Tavernier, D. *Pure & Appl. Chem.* **1995**, *67*, 1307.
20. Griffiths, W. D.; Bender, M. L. *Adv. Catal.* **1973**, *23*, 209.
21. (a) Tahli, A.; Elshaarawy, R. F. M.; Köc, Ü.; Kautz, A. C.; Janiak, C. *Polyhedron.* **2016**, *579*; (b) Dey, A.; Bairagi, D.; Biradha, K. *Cryst. Growth Des.* **2017**, *17*, 3885.

Chapter 1 - Introduction

22. Jeon, W. S.; Moon, K.; Park, S. H.; Chun, H.; Ko, Y. H.; Lee, J. Y.; Lee, E. S.; Samal, S.; Selvapalam, S.; Rekharsky, M.; Sindelar, V.; Sobransingh, D.; Inoue, Y.; Kaifer, A. E.; Kim, K. *J. Am. Chem. Soc.* **2005**, *127*, 12984.
23. Haino, T.; Yanase, M.; Fukazawa, Y. *Tetrahedron Lett.* **1997**, *38*, 3739.
24. Gavriš, S. P.; Lampeka, Y. D.; Lightfoot, P. *Inorg. Chim. Acta.* **2004**, *357*, 1023.
25. Kyba, E. P.; Helgeson, R. C.; Madan, K.; Gokel, G. W.; Tarnowski, T. L.; Moore, S. S.; Cram, D. J. *J. Am. Chem. Soc.* **1977**, *99*, 2564.
26. Pearson, R. G. *J. Am. Chem. Soc.* **1963**, *85*, 3533.
27. Kitaigorodskii, A. I. *Molecular Crystals and Molecules*; Academic Press: New York, 1973.
28. Thompson, H. P. G.; Day, G. M. *Chem. Sci.* **2014**, *5*, 3173.
29. Tozawa, T.; Jones, J. T. A.; Swamy, S. I.; Jiang, S.; Adams, D. J.; Shakespeare, S.; Clowes, R.; Bradshaw, D.; Hasell, T.; Chong, S. Y.; Tang, C.; Thompson, S.; Parker, J.; Trewin, A.; Bacsa, J.; Slawin, A. M. Z.; Steiner, A.; Cooper, A. I. *Nat. Mater.* **2009**, *8*, 973.
30. Barbour, L. J.; Das, D.; Jacobs, T.; Lloyd, G. O.; Smith, V. J. Concepts and Nomenclature in Chemical Crystallography. In *Supramolecular Chemistry: From Molecules to Nanomaterials*; Gale, P. A., Steed, J. W., Eds.; John Wiley & Sons, Ltd: West Sussex, U.K., 2012.
31. Zhang, J.-P.; Huang, X.-C.; Chen, X.-M. *Chem. Soc. Rev.* **2009**, *38*, 2385.
32. Braga, D.; Grepioni, F. *Chem. Soc. Rev.* **2000**, *29*, 229.
33. Li, Y.; Li, L.; Zhu, Y.; Meng, X.; Wu, A. *Cryst. Growth. Des.* **2009**, *9*, 4255.
34. Clarke, J. B.; Hastie, J. W.; Kihlberg, L. H. E.; Metselaar, R.; Thackeray, M. M. *Pure Appl. Chem.* **1994**, *66*, 584.
35. Groom, C. R.; Bruno, I. J.; Lightfoot, M. P.; Ward, S. C. *Acta Cryst.* **2016**, *B72*, 171.
36. (a) Grupce, O.; Penavic, M.; Jovanovski, G. *J. Chem. Cryst.* **1994**, *24*, 581; (b) Corpinot, M. K.; Guo, R.; Tocher, D. A.; Buanz, A. B. M.; Gaisford, S.; Price, S.L.; Bucar D.-K. *Cryst. Growth Des.* **2017**, *17*, 827.
37. Atwood, J. L.; Barbour, L. J.; Jerga, A.; Schottel, B. L. *Science.* **2002**, *296*, 2367.

Chapter 1 - Introduction

38. Barbour, L. J. *Chem. Commun.* **2006**, *11*, 1163.
39. Kitagawa, S.; Kitaura, R.; Noro, S.-I. *Angew. Chem. Int. Ed.* **2004**, *43*, 2334.
40. Zhang, Z.; Xiang, S.; Chen, B. *CrystEngComm.* **2011**, *13*, 5983.
41. Khan, N. A.; Jhung, S. H. *J. Hazard. Mater.* **2017**, 198.
42. (a) He, Y.; Zhou, W.; Qian, G., Chen, B. *Chem. Soc. Rev.* **2014**, *43*, 5657; (b) Gándara, F.; Furukawa, H.; Lee, S.; Yaghi, O. M. *J. Am. Chem. Soc.* **2014**, *136*, 5271; (c) Jiang, J.; Furukawa, H.; Zhang, Y.-B.; Yaghi, O. M. *J. Am. Chem. Soc.* **2016**, *138*, 10244; (d) Schlapbach, L.; Züttel, A. *Nature.* **2001**, *414*, 353.
43. Zhang, Z.; Yao, Z.-Z.; Xiang, S.; Chen, B. *Energy Environ. Sci.* **2014**, *7*, 2868.
44. (a) Horcajada, P.; Chalati, T.; Serre, C.; Gillet, B.; Sebrie, C.; Baati, T.; Eubank, J. F.; Heurtaux, D.; Clayette, P.; Kreuz, C.; Chang, J.-S.; Hwang, Y. K.; Marsaud, V.; Bories, P.-N.; Cynober, L.; Gil, S.; Férey, G.; Couvreur, P.; Gref, R. *Nat. Mater.* **2009**, *9*, 172; (b) Mihad, I.; Rana, S.; Ghaleb, H. *Curr. Med. Chem.* **2017**, *24*, 193.
45. Zhao, S.-N.; Song, X.-Z.; Song, S.-Y.; Zhang, H.-J. *Coord. Chem. Rev.* **2017**, *337*, 80.
46. Ma, S.; Zhou, H.C. *Chem. Commun.*, **2010**, *46*, 44.
47. (a) Chen, L.; Reiss, P. S.; Chong, S. Y.; Holden, D.; Jelfs, K. E.; Hasell, T.; Little, M. A.; Kewley, A.; Briggs, M. E.; Stephenson, A.; Thomas, K. M.; Armstrong, J. A.; Bell, J.; Busto, J.; Noel, R.; Liu, J.; Strachan, D. M.; Thallapally, P. K.; Cooper, A. I. *Nat. Mater.* **2014**, *13*, 954; (b) Hasell, T.; Cooper, A. I. *Nat. Rev. Mater.* **2016**, *1*, 16053.
48. Karak, S.; Kandambeth, S.; Biswal, B. P.; Sasmal, H. S.; Kumar, S.; Pachfule, P.; Banerjee, R. *J. Am. Chem. Soc.* **2017**, *139*, 1856.
49. (a) Sozzani, P.; Bracco, S.; Comotti, A.; Ferretti, L.; Simonutti, R. *Angew. Chem. Int. Ed.* **2005**, *44*, 1816; (b) He, Y.; Xiang, S.; Chen, B. *J. Am. Chem. Soc.* **2011**, *133*, 14570; (c) Wang, P.; Wu, Y.; Zhao, Y.; Yu, Y.; Zhang, M.; Cao, L. *Chem. Commun.* **2017**, *53*, 5503.
50. Smaldone, R. A.; Forgan, R. S.; Furukawa, H.; Gassensmith, J. J.; Slawin, A. M. Z.; Yaghi, O. M.; Stoddart, J. F. *Angew. Chem. Int. Ed.* **2010**, *49*, 8630.
51. Zhang, Z.; Drapailo, A.; Matvieiev, L.; Wojtas, L.; Zaworotko, M. J. *Chem. Commun.* **2013**, *49*, 8353.

Chapter 1 - Introduction

52. Wang, P.; Wu, Y.; Zhao, Y.; Yu, Y.; Zhang, M.; Cao, L. *Chem. Commun.* **2017**, 53, 5503.
53. Jie, K.; Liu, M.; Zhou, Y.; Little, M. A.; Bonakala, S.; Chong, S. Y.; Stephenson, A. Chen, L.; Huang, F.; Cooper, A. I. *J. Am. Chem. Soc.* **2017**, 139, 2908.
54. Bojdys, M. J.; Briggs, M. E.; Jones, J. T. A.; Adams, D. J.; Chong, S. Y.; Schmidtman, M.; Cooper, A. I. *J. Am. Chem. Soc.* **2011**, 133, 16566.
55. Sing, K. S. W.; Everett, D. H.; Haul, R. A. W.; Moscou, L.; Pierotti, R. A.; Rouquérol, J.; Simieniewska, T. *Pure Appl. Chem.* **1985**, 57, 603.
56. Alothman, Z. A. *Materials.* **2012**, 5, 2874.
57. Dobrzanska, L.; Lloyd, G. O.; Esterhuysen, C.; Barbour, L. J. *Angew. Chem. Int. Ed.* **2006**, 45, 5856.
58. Barbour, L. J. *Aust. J. Chem.* **2006**, 59, 595.
59. (a) Cao, M.-L.; Mo, H.-J.; Liang, J.-J.; Ye, B.-H. *CrystEngComm.* **2009**, 11, 784; (b) Liu, T.-F.; Sun, G.-M.; Tian, X.-Z.; Zhu, Y.; Yuan, Z.-J.; Liu, S.-J.; Xu, W.-Y.; Feng, X.-F. *Chem. Commun.* **2012**, 48, 1006; (c) Zou, L.; Feng, D.; Chen, Y.-P.; Fordham, S.; Wang, X.; Liu, Y.; Zhou, H.-C. *J. Am. Chem. Soc.* **2014**, 136, 7813; (d) Song, Y.-M.; Luo, F.; Luo, M.-B.; Liao, Z.-W.; (e) Lv, X.-X.; Shi, L.-L.; Li, K.; Li, B.-L.; Li, H. Y. *Chem. Commun.* **2017**, 53, 1860.
60. Sajid, M. *Environ. Sci. Pollut. Res.* **2016**, 23, 14805.
61. Barrow, S. J.; Kasera S.; Rowland, M. J.; del Barrio, J.; Scherman, O. A. *Chem. Rev.* **2015**, 115, 12320.
62. (a) Tian, J.; Ma, S.; Thallapally, P. K.; Fowler, D.; McGraila, B. P.; Atwood, J. L. *Chem. Commun.* **2011**, 47, 7626; (b) Liebl, M. R.; Senker, J. *Chem. Mater.*, **2013**, 25, 970; (c) Kim, H.; Kim, Y.; Yoon, M.; Lim, S.; Park, S. M.; Seo, G.; Kim, K. *J. Am. Chem. Soc.* **2010**, 132, 12200.

Chapter 2

Experimental Techniques

2.1. SINGLE-CRYSTAL X-RAY DIFFRACTION (SCXRD)

Single-crystal X-ray diffraction (SCXRD) analysis was used to determine the crystal structures of crystalline materials. Typically, a suitable single crystal was selected based on its shape and visual quality (i.e. well-defined shape with minimum scratches and cracks) as well as its ability to extinguish plane-polarised light. Paratone oil was used to mount the single crystal on the tip of a MiTeGen¹ foil (Figure 1), which was then placed on a goniometer head fitted to the diffractometer.

Three different diffractometers were used to collect diffraction data:

- 1) Bruker Apex-II SMART;
- 2) Bruker Apex-II DUO;
- 3) Bruker D8 Venture.

The diffractometers are equipped with INCOATEC I μ S microfocus sources that produce multilayer-monochromated Mo-K α radiation ($\lambda = 0.71073 \text{ \AA}$). The Bruker Apex-II DUO is also equipped with a multilayer-monochromated Cu-K α ($\lambda = 1.5418 \text{ \AA}$) Incoatec I μ S microfocus source. The temperature was controlled using a cryostat supplied with liquid nitrogen. Both Bruker SMART and Bruker DUO are fitted with a CCD area detector and an Oxford Cryosystems 700+ cryostat, while the Bruker D8 Venture is fitted with a Photon II CPAD detector and an Oxford Cryosystems 800+ cryostat. The frame exposure time as well as the number of frames collected in each case was varied depending on the diffraction quality of the mounted crystal.

Data reduction was carried out using APEX III² software. The collected frames were integrated with a resolution cut-off of 0.81 \AA using Bruker SAINT³ software. All absorption corrections and systematic error corrections were performed with SADABS⁴. The structures were solved either using a novel dual-space algorithm employed by SHELXT⁵ or using direct methods via SHELXS-97⁶. SHELXL-97⁶ was used to expand and refine the structures in the graphical interface X-Seed⁷. High quality molecular graphics images were produced using POV-Ray.⁸

Chapter 2 - Experimental Techniques

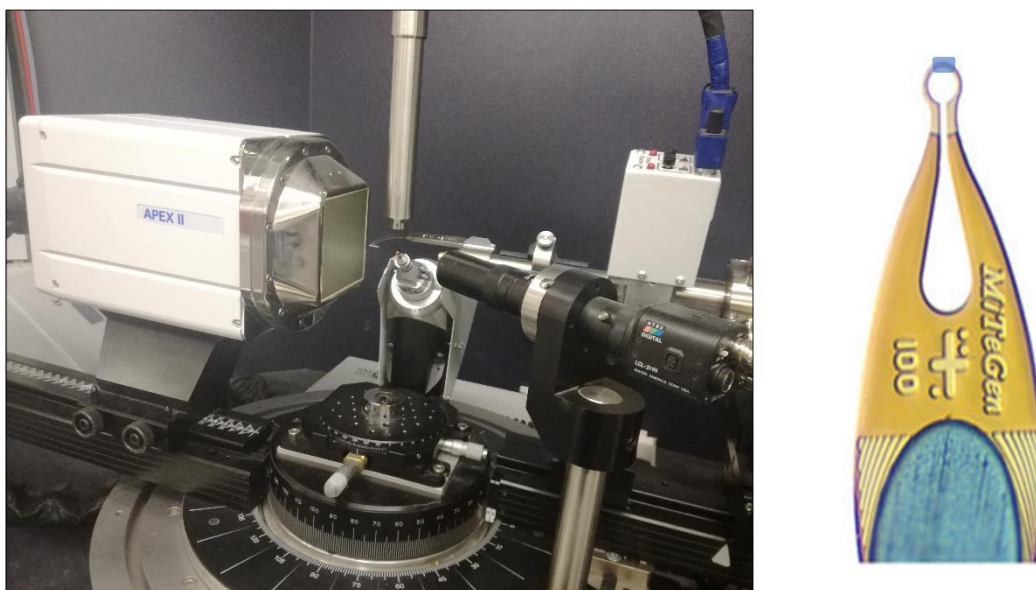


Figure 1. The Bruker Apex-II SMART diffractometer (left) and an illustration of a crystal mounted on a MiTeGen¹ foil (right).

2.2. GAS SORPTION

2.2.1. Volumetric sorption analysis

Gas sorption analysis was carried out using a Setaram PCTPro E&E instrument equipped with a MicroDoser attachment. This instrument makes use of the volumetric method to determine the amount of gas adsorbed by the sample. A fixed value of dosing pressure (1-5 bar) was supplied to the sample holder during the measurement cycle. The pressure in the sample holder drops as adsorption occurs. The amount of gas adsorbed at the equilibrium pressure is measured as the difference between the amount of gas supplied and the amount of gas that is required to fill the remaining volume in the sample holder. This volume needs to be determined prior to the gas sorption experiment by means of a volume calibration protocol. Volume calibration was performed for each sample using helium gas before starting the sorption experiment. The sorption isotherms were recorded isothermally by measuring the amount of gas adsorbed at the equilibrium pressure.⁹

All samples (90-100 mg) were activated prior to loading, followed by *in-situ* activation under reduced pressure. The experiments were performed at a constant temperature (298 K) in the range of 0-60 bar (the upper pressure limit of the MicroDoser attachment). For CO₂, N₂ and CH₄ gas, a maximum pressure of 50 bar was used, which is below the saturation vapour pressure of these gases at 298 K.

2.2.2. Gravimetric sorption analysis

Gravimetric sorption analysis was carried out using an Intelligent Gravimetric Analyser (IGA-002). This instrument measures the uptake of gas by the sample by determining the increase in sample weight at a set pressure and constant temperature. An adsorption balance is used to directly record the weight of the sample during adsorption and desorption. The effects of gas buoyancy are corrected for automatically.

The sample (20-30 mg) was activated prior to loading, followed by *in-situ* activation under reduced pressure. All isotherms were recorded at 298 K up to 20 bar of gas pressure. A Grant refrigerated recirculation bath was used to keep the sample chamber at a constant temperature.

2.3. ENVIRONMENTAL GAS CELL

An environmental gas cell, developed by Prof. L. J. Barbour¹⁰, was used to collect SCXRD and powder X-ray diffraction (PXRD) data for samples under gas pressure. This gas cell can be used to conduct experiments under controlled environments and is able to withstand gas pressure up to 80 bar, depending on the diameter size of the capillary.

A gas cell was prepared by attaching a 0.2 mm glass capillary to a stainless steel fitting with epoxy resin. For SCXRD studies a suitable crystal was glued to the tip of a glass microfiber and allowed to dry. This fibre was then carefully inserted into the glass capillary and glued at a suitable position. For PXRD studies, the capillary was packed with a powdered sample and secured with a small piece of cotton wool. The stainless steel fitting was attached to a nickel-coated brass gas cell, which allows for gas loading by means of a valve stem. An O-ring embedded between the steel nut and brass gas cell was used to ensure a leak-free system. The gas cell was then mounted on a goniometer head before collecting SCXRD or PXRD data.

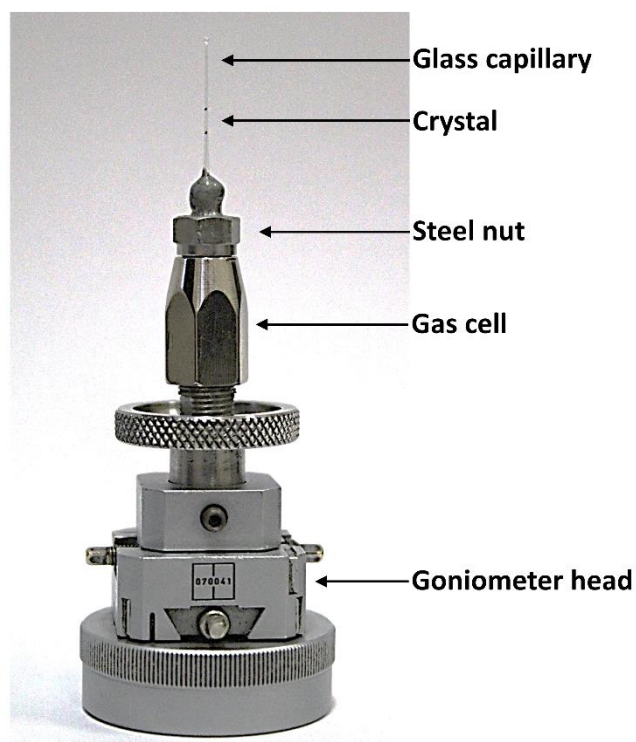
Chapter 2 - Experimental Techniques

Figure 2. Photograph of an environmental gas cell mounted on a goniometer head.

2.4. POWDER X-RAY DIFFRACTION (PXRD)

Powdered samples were prepared by means of grinding with a mortar and pestle prior to being placed on a zero-background holder for data collection using a Bruker D2 Phaser diffractometer equipped with Cu-K α radiation ($\lambda = 1.5418 \text{ \AA}$) and a Lynxeye 1D detector. The diffraction patterns were recorded at atmospheric pressure with an angular scanning range of 5-40°, a step size of 0.016° and an exposure time of 0.50 s. The experimental powder patterns were analysed using X'Pert HighScore Plus. The program Mercury (part of the Cambridge Structural Database package) was used to generate simulated powder patterns where applicable.

2.5. VARIABLE PRESSURE PXRD (VP-PXRD)

Variable-pressure PXRD experiments were carried out on a PANalytical X'Pert Pro instrument using Bragg-Brentano geometry. The instrument was operated using a capillary stage mount, allowing the use of an environmental gas cell as the sample holder. The diffraction patterns were recorded using Cu K α radiation ($\lambda = 1.5418 \text{ \AA}$) and an angular

Chapter 2 - Experimental Techniques

scanning range of 5-40°. X'Pert HighScore Plus software was used to analyse the powder diffraction patterns.

2.6. THERMOGRAVIMETRIC ANALYSIS (TGA)

A TA Instruments TGA Q500 analyser was used to perform thermogravimetric analysis (TGA). The sample (3-5 mg) was placed in an aluminium crucible and heated from room temperature to 773 K at a rate of 283 K min⁻¹. Nitrogen gas was used to purge the furnace at a flow rate of 50 ml min⁻¹. The weight loss of the sample is recorded as a function of temperature to produce a thermogram. Universal Analysis 2000 software (TA Instruments) was used to analyse the thermograms.

2.7. DIFFERENTIAL SCANNING CALORIMETRY (DSC)

DSC was carried out using a TA Instruments Q20 instrument equipped with a refrigerated cooling system. The sample (2-5 mg) was placed in a sealed aluminium pan and the change in heat flow of the sample was recorded as a function of temperature relative to an empty sealed reference pan. Any energetic event is recorded as an endothermic or exothermic peak relative to temperature. The temperature was ramped between 253 and 573 K using a rate of 278-283 K min⁻¹ depending on the sample. Dry nitrogen gas was used to purge the furnace at a flow rate of 50 ml min⁻¹. Universal Analysis 2000 software (TA Instruments) was used to analyse the data.

2.8. PRESSURE-RAMPED DSC (P-DSC)

This instrument measures the change in heat flow of the sample as a function of pressure. All P-DSC experiments were carried out on a Setaram μ DSC7 Evo instrument equipped with a high pressure sample holder. A Teledyne ISCO syringe pump (Model 260D) coupled to a D-series pump controller was used to increase the pressure throughout the measurement. ISCO software developed by Prof. L. J. Barbour was used to control the pressure gradient. Calisto Data Acquisition software was used to record the data. Calistro Processing software was used to process the raw data before plotting the data with OriginPro 9 software.

2.9. SUPERCRITICAL DRYING

Supercritical CO₂ experiments were performed using a Tousimis SAMDRI-PVT-3D instrument. A glass vial containing a small amount of sample is placed in the high pressure sample chamber. Liquid CO₂ is used to cool the sample chamber to approximately 263 K. Once this temperature is reached, the chamber is filled and the sample is submerged in liquid CO₂. The chamber is then slowly heated to 312 K to reach the supercritical point of CO₂. The sample is kept under supercritical conditions for several hours during which the solvent molecules could be replaced by CO₂ molecules. Finally, the chamber is slowly depressurised and the sample removed.

2.10. ELECTRON DENSITY CALCULATIONS (SQUEEZE)

The estimated number of guest molecules trapped in the voids of a SCXRD structure was calculated after carrying out a Platon/SQUEEZE¹¹ analysis of the refined structure. Platon/SQUEEZE calculates the solvent accessible (void) volume in the refined structure, followed by the total number of electrons present per unit cell in these voids as a result of unassigned electron density in the refined structure. The number of guest molecules trapped in the voids can then be calculated based on the electron count.

*Chapter 2 - Experimental Techniques***REFERENCES**

1. MiTeGen, Microloops LDTM, www.mitegen.com, Ithaca, NY 14852.
2. *APEX3 Data Collection Software*, Bruker AXS Inc.: Madison, WI, **2016**.
3. *SAINT Data Reduction Software*, Bruker AXS Inc.: Madison, WI, **2016**.
4. *SADABS Data Correction Software*, Bruker AXS Inc.: Madison, WI, **2016**.
5. Sheldrick, G. M. *Acta Cryst.* **2015**, A71, 3.
6. Sheldrick, G. M. *Acta Cryst.* **2008**, A64, 112.
7. Barbour, L. J. *J. Supramol. Chem.* **2001**, 1, 189.
8. *POV-Ray for Windows*, Version 3.6, Persistence of Vision Raytracer Pty. Ltd. **2004**.
9. Sing, K. S. W.; Everett, D. H.; Haul, R. A. W.; Moscou, L.; Pierotti, R. A.; Rouquérol, J.; Simieniewska, T. *Pure Appl. Chem.* **1985**, 57, 603.
10. Jacobs, T.; Lloyd, G. O.; Gerthenbach, J.; Müller-Nedebock, K. K.; Esterhuysen, C.; Barbour, L. J. *Angew. Chem. Int. Ed.*, **2012**, 124, 4997.
11. Spek, A. L. *Acta Cryst.* **2009**, D65, 148.

Chapter 3

p-tert-Butylcalix[4]arene

Calixarenes are a class of polyphenolic, macrocyclic compounds that were first introduced by Gutsche in the 1970s.¹ They were mainly used as building blocks in organic synthesis and the first single crystal structures were only reported nine years later.² *p*-tert-Butylcalix[4]arene (TBC4) consists of four *p*-tert-butylphenol units linked together by methylene groups. Strong hydrogen bonding between the hydroxyl groups allows the TBC4 molecule to adopt a cone conformation with a hydrophobic cavity (Figure 1).

An interesting feature of the low density polymorph of TBC4 is that, despite its lack of permanent porosity, a wide variety of small guest molecules are able to diffuse through the host structure to reach the intrinsic cavities present in the structure.³ Due to the chemical simplicity of the TBC4 cavity, it is an excellent model host for studying weak interactions with guest molecules.⁴ Moreover, TBC4 can undergo SC-SC transformations during the uptake and release of guest molecules. This allows both the initial and final phases to be structurally characterized and allows us to investigate the cooperativity between the TBC4 molecules during guest uptake.

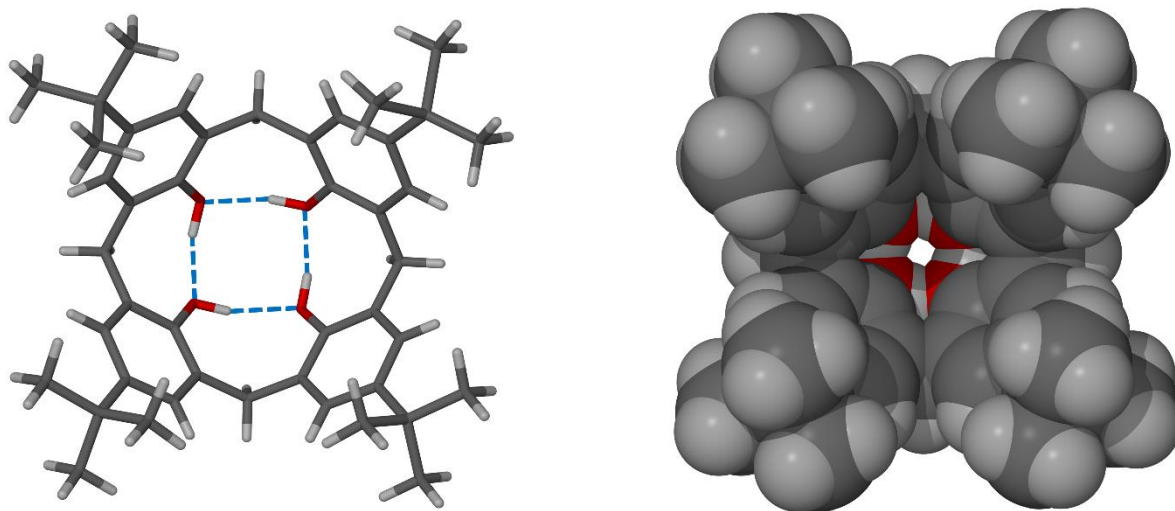


Figure 1. A top view of TBC4 indicating the intramolecular hydrogen bonding in blue (left) and a space-filling model illustrating the bowl formed by the molecule (right).

Chapter 3 – *p*-tert-Butylcalix[4]arene

TBC4 is a versatile host known to produce different structural motifs depending on the solvent used to recrystallize the host material.^{2,5} Typically, the TBC4 molecules arrange in bilayers and form a 1:1 or 1:2 inclusion compound in the tetragonal space groups $P4/n$ or $P4/nnc$, respectively.⁶ When crystallized from toluene, TBC4 forms a 1:1 inclusion compound in the tetragonal space group $P4/n$. However, a SC-SC transformation to the 2:1 $P4/nnc$ form occurs when half the toluene guest molecules are removed.⁶ Guest-free forms are obtained by complete desolvation, yielding either the low ($P2_1/n$) or high density ($P2_1/c$) polymorph of TBC4, depending on the conditions.⁷ Although the close-packed arrangement of the high density polymorph prohibits guest uptake, the low density polymorph forms 1:1 inclusion compounds while the host lattice remains unchanged.⁸ Figure 2 displays the packing arrangements of the TBC4 molecules in the guest-free $P2_1/n$ (**1a_o**) and $P2_1/c$ (**1b_o**) forms, as well as in the $P4/n$ (**1c**) and $P4/nnc$ (**1d**) inclusion compounds.

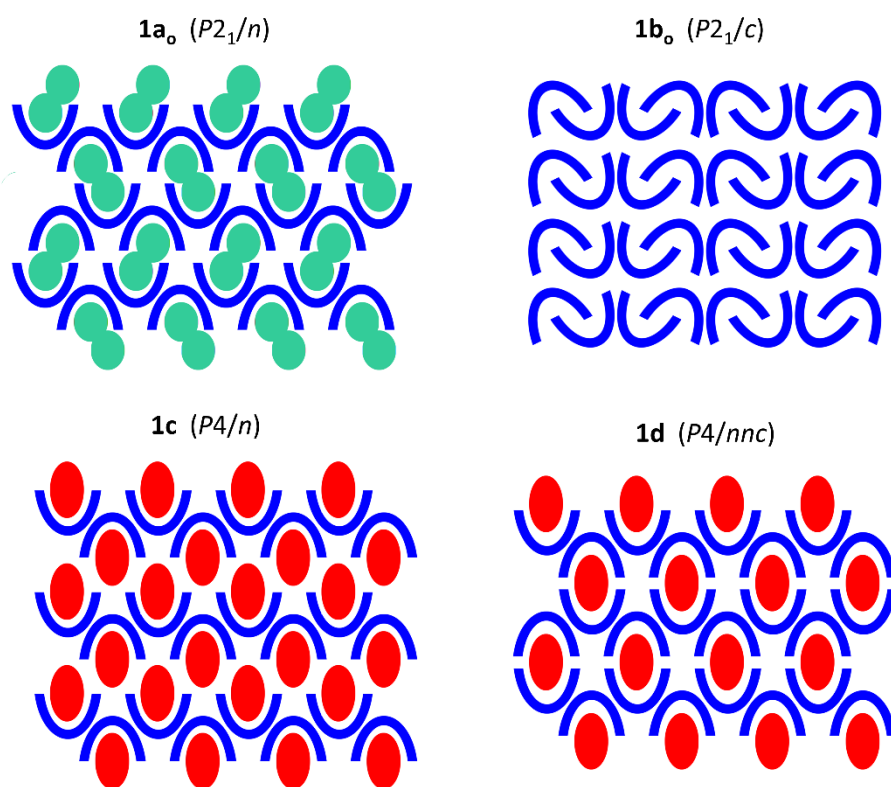


Figure 2. Cartoons of the packing arrangements of TBC4 in the monoclinic space groups $P2_1/n$ (**1a_o**) and $P2_1/c$ (**1b_o**) in the guest-free forms, and in the tetragonal space groups $P4/n$ (**1c**) and $P4/nnc$ (**1d**). Blue arcs represent TBC4 molecules, green circles represent empty intrinsic cavities and red ellipses represent guest molecules.

Chapter 3 – *p*-*tert*-Butylcalix[4]arene

This chapter discusses the low and high density polymorphs (LDP and HDP, respectively) of guest-free TBC4. The properties and porosity of these polymorphs were studied in detail. The LDP of TBC4 was previously studied using sorption analysis at 298 K and was shown to form two distinct inclusion compounds under CO₂ pressure.⁴ At relatively low pressure (up to 22 bar) a 1:1 (CO₂:TBC4) inclusion compound is formed, whereas a 2:1 inclusion compound is formed above 22 bar. Furthermore, the HDP of TBC4 was reported to undergo a gas-induced structural transformation at relatively high CO₂ pressure.⁹ In this study, the structural transformation was investigated using P-DSC and VP-PXRD.

3.1. LOW DENSITY POLYMORPH OF *P*-*TERT*-BUTYLCALIX[4]ARENE

3.1.1. Synthesis and crystallization

TBC4 was synthesized according to a literature procedure¹⁰ from *p*-*tert*-butyl phenol and formaldehyde. Guest-free single crystals of the LDP (**1a_o**) were grown by sublimation at 533 K under dynamic vacuum (Figure 3).

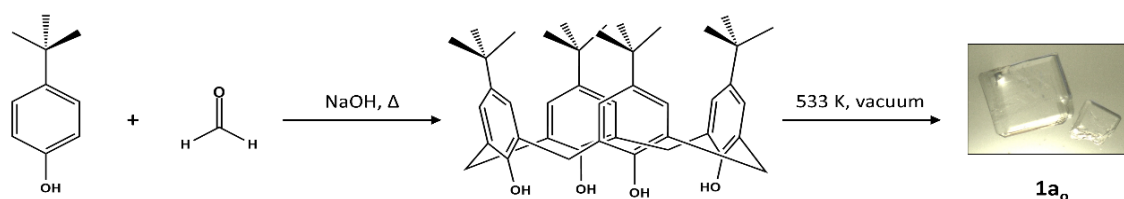


Figure 3. The synthesis of TBC4, followed by sublimation at 533 K to produce clear block-like crystals of **1a_o**.

3.1.2. Structural analysis

A single crystal selected from a freshly sublimed sample of **1a_o** was mounted in an environmental gas cell, which was then evacuated. SCXRD analysis of **1a_o** at 298 K revealed that the compound crystallizes in the monoclinic space group $P2_1/n$. The TBC4 molecules are arranged in an offset, face-to-face fashion in consecutive ABCD layers stacked along the crystallographic *b* axis (Figure 4).¹¹ The TBC4 molecules from layers AB and CD are closely-packed to produce repeating bilayers. The *tert*-butyl groups of offset, facing TBC4 molecules in adjacent bilayers are displaced by approximately 2.35 Å along the *c* axis. No strong intermolecular interactions occur between the TBC4 molecules and the overall structure is held together by weak van der Waals interactions.

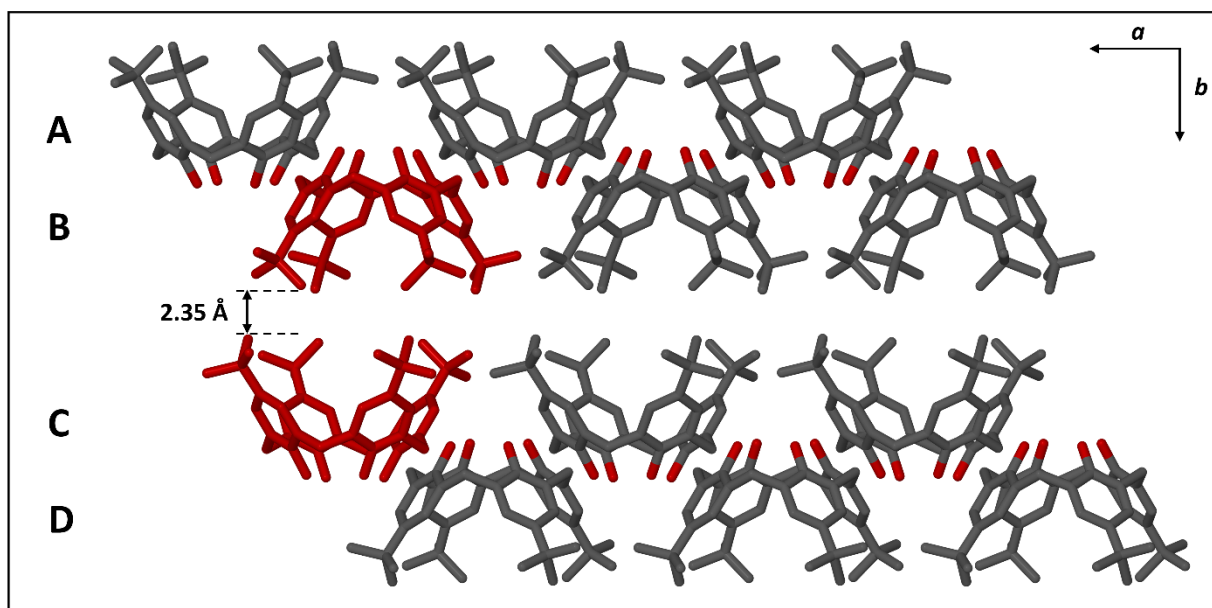


Figure 4. The structure of guest-free TBC4 (**1a₀**) at 298 K viewed along the crystallographic *c* axis. The four different layers are labeled to illustrate the AB and CD bilayers. An offset face-to-face dimer is highlighted in red. Hydrogen atoms are omitted for clarity.

Large intrinsic cavities, each with a volume of 275 \AA^3 , are present in the bowls formed by each TBC4 molecule (Figure 5a). Since these cavities are isolated by surrounding molecules the porosity of **1a₀** can be described as zero-dimensional (0D). At 298 K, all four *tert*-butyl groups of each TBC4 molecule appear to be rotationally disordered over at least two positions (Figure 5b). SCXRD analysis of the same crystal was also performed at a low temperature (100 K) in order to obtain better quality data. At this temperature only one of the *tert*-butyl groups is disordered over two positions (Figure 5c).

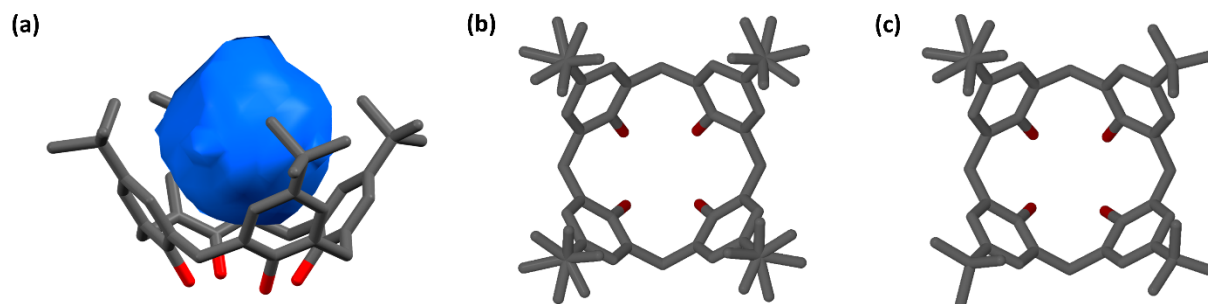


Figure 5. (a) The intrinsic void situated in the bowl of TBC4 and the disorder of the *tert*-butyl groups at (b) 298 K and (c) 100 K.

PXRD analysis (Figure 6) was used to confirm the homogeneity of the bulk sample. The powder pattern of the bulk material matched the pattern calculated from the single crystal structure of **1a_o**. The powder pattern also matched the calculated pattern of the reported structure⁸ obtained by sublimation. This confirms that a bulk sample of TBC4 in the low density form can easily be prepared by means of sublimation.

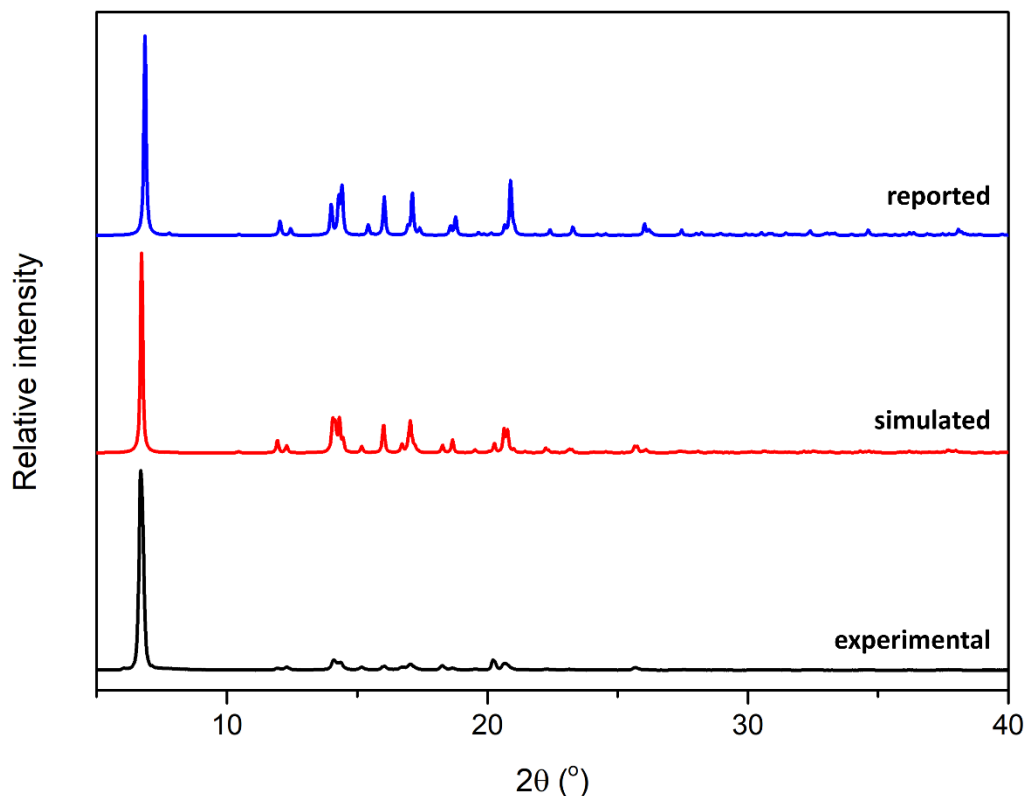


Figure 6. The reported (top), simulated (middle) and experimental (bottom) powder diffraction patterns of the LDP of TBC4.

3.1.3. Thermal analysis

The TGA thermogram of a freshly sublimed sample of **1a_o** (red curve) is given in Figure 7. A gradual weight loss is observed until the sample starts to sublime during the large step at 533 K. If the freshly sublimed sample is left exposed to air for a week (black curve) a small weight loss step becomes visible in the thermogram. A 1.6% weight loss was observed up to 423 K, likely due to the loss of atmospheric gases (such as N₂ or O₂) that had been adsorbed into the discrete pores of **1a_o**. The guest-free form **1a_o** can be regenerated by activating the sample at 333 K under dynamic vacuum for 24 h.

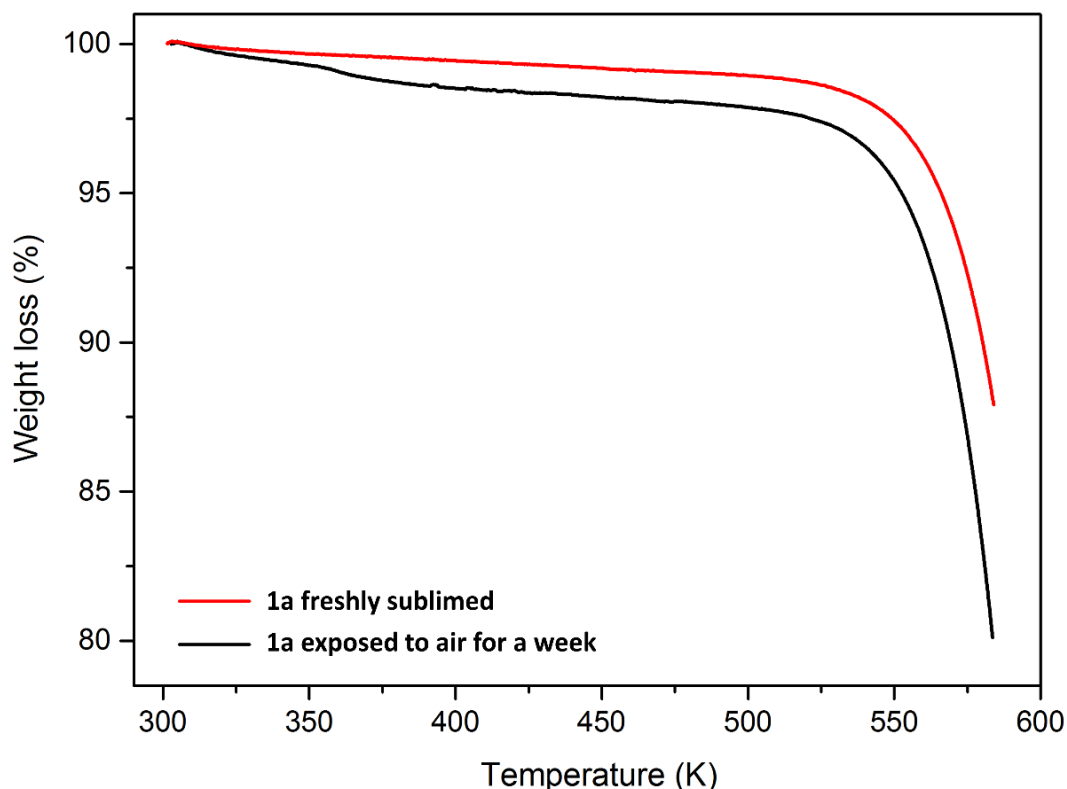


Figure 7. TGA thermogram of a freshly sublimed sample of **1a_o** (red) and the thermogram of **1a_o** that had been left exposed to air for a week (black).

3.1.4. Volumetric sorption analysis

Although the adsorption of CO₂ into **1a_o** has been reported,⁴ the sorption data were rather poorly measured. The sorption data were fitted to a Langmuir adsorption isotherm (type I), but did not seem to converge at higher pressure.⁴ For this reason the sorption of CO₂ by **1a_o** was re-investigated in this study. A freshly sublimed sample was activated *in-situ* at 333 K under dynamic vacuum prior to the sorption analysis. The CO₂ uptake was measured volumetrically up to 50 bar at a constant temperature of 298 K.

The CO₂ sorption isotherm of **1a_o** at 298 K is depicted in Figure 8 (blue curve). The uptake of CO₂ occurs in two steps. From 0-22 bar the concentration of CO₂ adsorbed increases until a maximum of 0.95 molecules of CO₂ are adsorbed per molecule of TBC4 (~1.47 mmol g⁻¹). At 22 bar a second adsorption step occurs. This step is indicative of a structural transformation to a more porous phase with a larger CO₂ loading capacity (**1c**).⁴ Consequently, the uptake of CO₂ increases further until 1.45 CO₂ molecules are adsorbed per molecule of TBC4 at 50 bar (~2.23 mmol g⁻¹). Therefore, at a pressure below 22 bar a CO₂ inclusion compound (**1a**·CO₂) with an ideal stoichiometry of 1:1 (CO₂:TBC4) is formed,

whereas a 2:1 CO₂ inclusion compound (**1c**·CO₂) ideally forms at high pressure. Owing to the very slow kinetics of sorption at high CO₂ pressure, a larger deviation from the ideal stoichiometry is observed at 50 bar. For both steps, the uptake of CO₂ can be described by a type I isotherm. Despite the 0D porosity of **1a_o**, the CO₂ molecule can easily move through the material to fill the isolated cavities. However, during desorption no step was observed, suggesting that the sample remains in the same phase, even under vacuum.

To confirm this, a second sorption cycle was performed using the same sample. The sample was activated *in-situ* at 298 K under dynamic vacuum for 24 h prior to the second sorption cycle. The CO₂ isotherm of the second cycle is represented by the black curve in Figure 8. The adsorption and desorption of CO₂ occurs in one step and follows a type I isotherm up to 50 bar. There is no indication of a structural transformation. During the second sorption cycle 1.33 molecules of CO₂ were adsorbed per TBC4 molecule at 50 bar (~2.05 mmol g⁻¹). The amount of CO₂ adsorbed is slightly lower as compared to that in the first cycle. A possible explanation is that the sample was only partially activated during the vacuum activation process, resulting in decreased adsorption during the second sorption cycle.

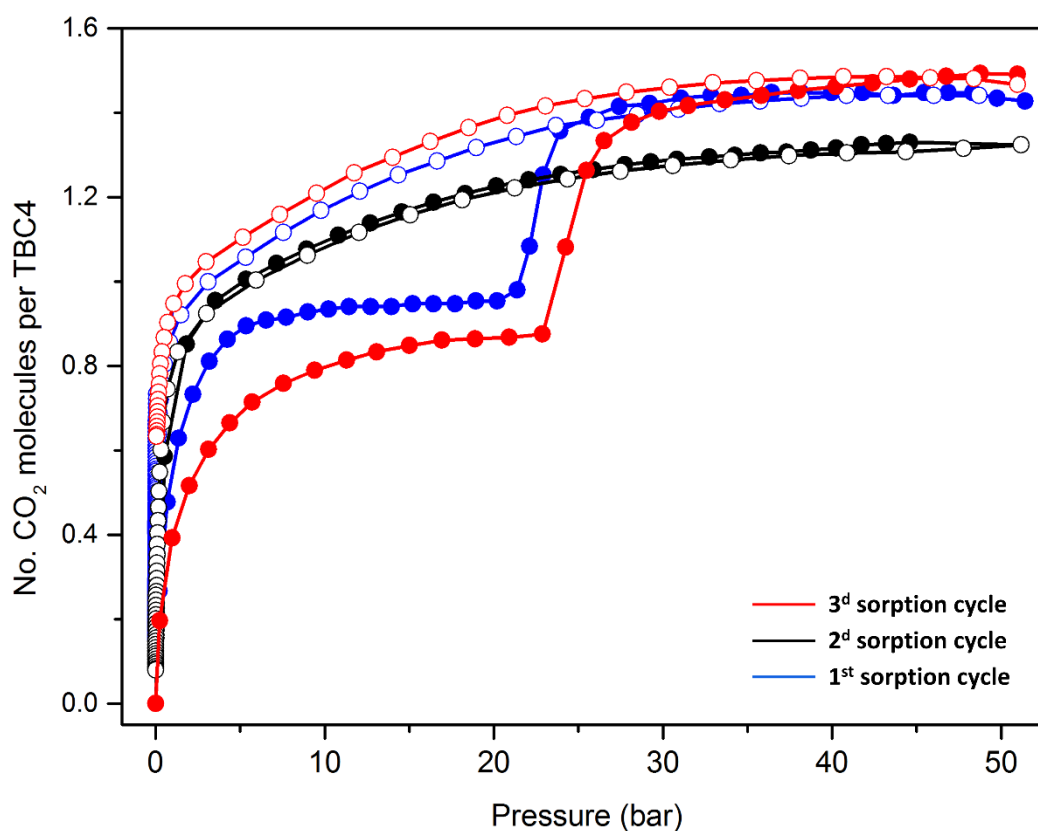


Figure 8. The first (blue), second (black) and third (red) CO₂ sorption isotherms of **1a_o**, measured at 298 K. The filled circles represent adsorption and the open circles represent desorption.

Chapter 3 – p-tert-Butylcalix[4]arene

The same sample was then activated *in-situ* at 333 K under dynamic vacuum for 12 h before starting a third sorption cycle. The third sorption isotherm is indicated by the red curve in Figure 8. This sorption profile is similar to that of the first cycle. These results suggest that **1a₀** can be regenerated under relatively mild activation conditions. The phase transformations from **1a₀**→**1a·CO₂**→**1c·CO₂** were further investigated using P-DSC, T-DSC and VP-PXRD, and are discussed in Section 3.1.5 below.

3.1.5. Investigating the phase transformation

A guest-free sample of **1a₀** was scanned from 1-55 bar at 298 K using P-DSC (Figure 9). In agreement with the sorption results, no energetic event occurred in the range of 1-22 bar. However, at 22 bar an exothermic event is observed in the P-DSC thermogram, indicating an increased uptake of CO₂ due to the structural change from **1a·CO₂** to **1c·CO₂**. The energy evolved during this phase transformation (sorption + structural change) is ~10.68 kJ mol⁻¹. No corresponding endothermic peak was observed when the pressure was decreased back to vacuum. When the same sample was subjected to a second P-DSC cycle after being activated *in-situ* at 298 K under dynamic vacuum overnight, no distinct exothermic event was observed. This observation agrees with the sorption results and indicates that the compound remains in the same phase as **1c·CO₂**, even after being subjected to vacuum.

A third P-DSC cycle was performed after **1a₀** was regenerated by heating the sample *in-situ* at 333 K under dynamic vacuum overnight. Similar to the first P-DSC cycle, the structural change to **1c·CO₂** is represented by an exothermic event that starts at 22 bar. The energy associated with this event is ~9.73 kJ mol⁻¹ and agrees well with the energy evolved during the first transformation.

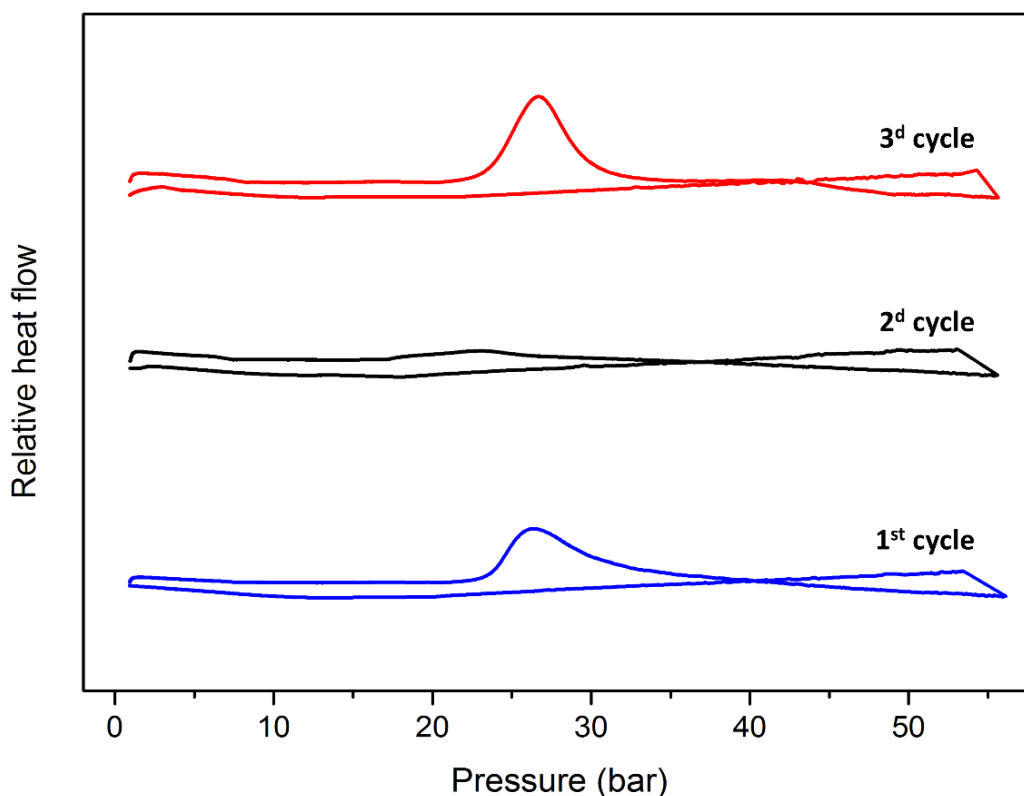


Figure 9. P-DSC plots of **1a₀** measured during the first P-DSC cycle (blue curve), **1d** measured during the second cycle (black curve) and **1a** (regenerated) measured during the third cycle (red curve).

T-DSC was carried out for **1a₀** and a guest-free sample of **1c·CO₂** (**1c₀**) in the range of 253-353 K (Figure 10). No energetic event occurs when **1a₀** is heated up to 353 K. The form **1c₀** was prepared by activating **1c·CO₂** under dynamic vacuum at 298 K for 24 h. The T-DSC thermogram of **1c₀** shows a broad endothermic peak in the range of 315-328 K. This event represents the structural transformation from **1c₀** back to **1a₀**, as confirmed using VP-PXRD (discussed below). The same sample was subjected to a second T-DSC cycle immediately after the first cycle was complete. No energetic events are visible since the sample had already converted back to **1a₀**.

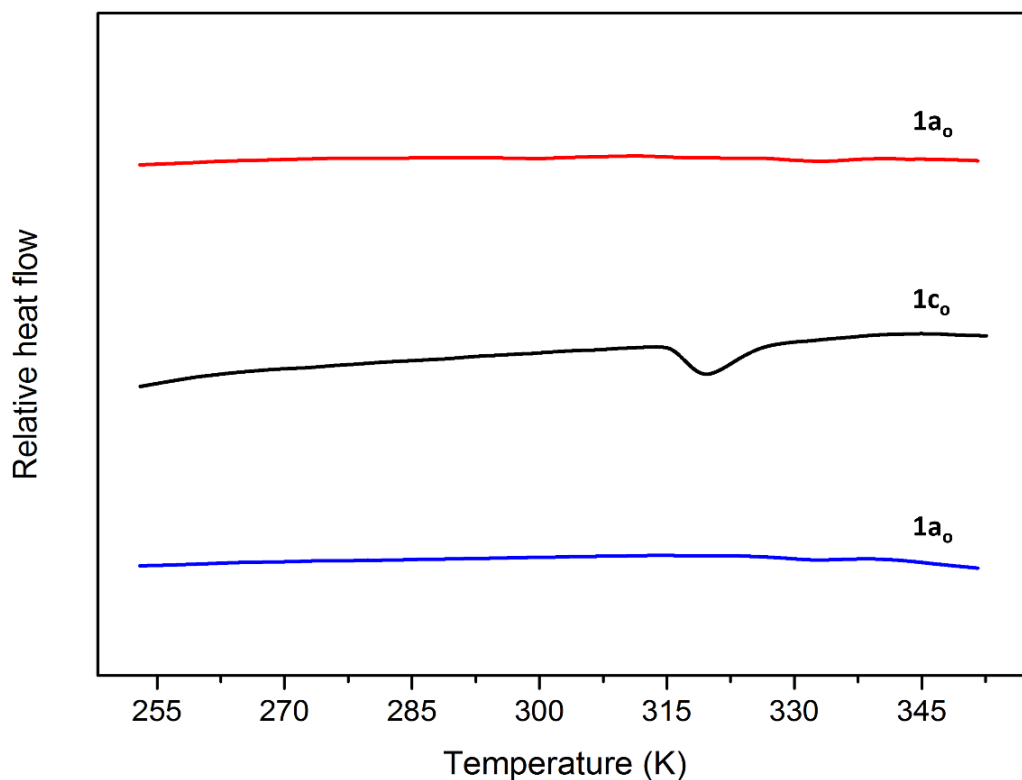


Figure 10. T-DSC cycles of **1a₀**, **1c₀** and **1a₀** (regenerated) during the second cycle of **1c₀**.

The phase transformations of **1a₀**→**1a₀·CO₂**→**1c₀·CO₂** were further investigated using VP-PXRD at 298 K (Figure 11). A powdered sample of **1a₀** was packed in an environmental gas cell and activated at 333 K under dynamic vacuum before the powder pattern of the guest-free sample was recorded. The powder patterns remain unchanged over the pressure range of 0-20 bar, except for the appearance of a small peak at 10.49°, presumably due to the uptake of CO₂ molecules. Between 20 and 25 bar there are noticeable changes in the powder patterns as the phase transformation from **1a₀·CO₂** to **1c₀·CO₂** occurs. At 25 bar, peaks appear at 9.76° and 11.93°, and a noticeable change in the powder pattern is visible between 13.48-23.95°. After recording the powder pattern at 50 bar, the sample was kept under dynamic vacuum (2.20×10^{-5} bar) for 3 days at 298 K to generate the guest-free form of **1c** (**1c₀**). The powder pattern of **1c₀** matches that of **1c₀·CO₂** at 50 bar, except for a clear reduction in the intensity of the peak at 9.76°, presumably due to the lack of CO₂ molecules. After the sample was activated overnight at 333 K under dynamic vacuum, the powder pattern matched that of guest-free **1a₀**, confirming that **1a₀** can be recovered homogeneously under relatively mild activation conditions.

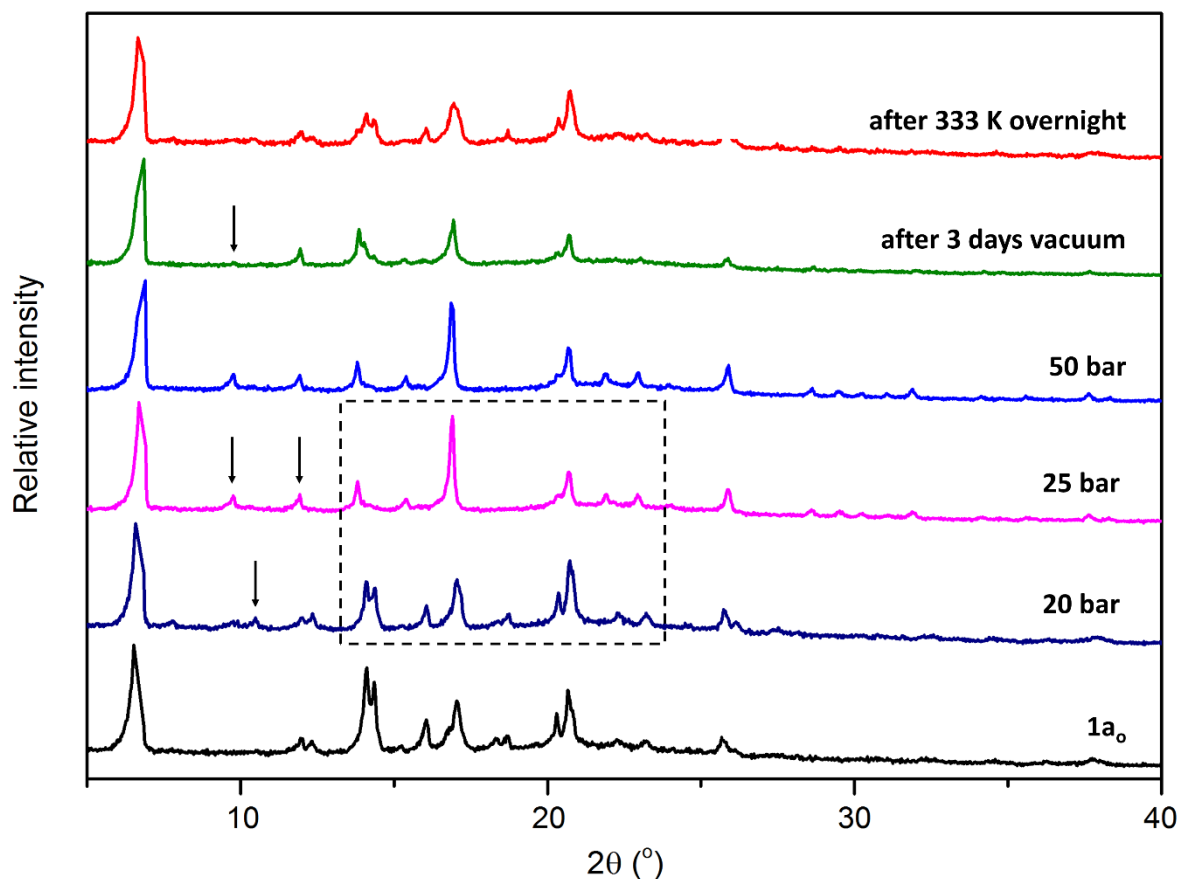


Figure 11. Comparison between the powder patterns of **1a₀**, the sample at pressures of 20 bar, 25 bar and 50 bar, the sample after being kept under vacuum for 3 days at 298 K, and the sample that had been activated at 333 K overnight.

To summarize (Figure 12), the structure remains unchanged when guest-free **1a₀** is pressurized to relatively low CO₂ pressures to form the CO₂ inclusion compound **1a·CO₂**. However, at pressures above 22 bar a phase transformation to the CO₂ inclusion compound **1c·CO₂** occurs. The CO₂ molecules can be removed from the high-pressure phase **1c·CO₂** under dynamic vacuum at 298 K to produce the guest-free form, **1c₀**. The original guest-free phase of **1a₀** can, however, be regenerated under relatively mild conditions (333 K).

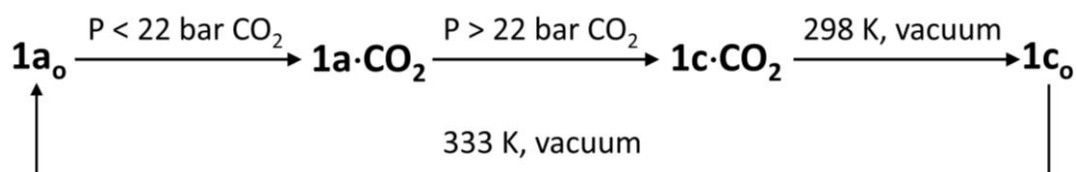


Figure 12. Schematic representation of the conversion from **1a₀** to **1a·CO₂**, **1c·CO₂** and **1c₀**, and the recovery of **1a₀**.

3.1.6. Structural analysis of the CO₂ inclusion compounds

SCXRD analysis was used to elucidate the structure of **1a**·CO₂ and **1c**·CO₂ at 298 K and 100 K. The occupancies of the CO₂ molecules in these structures were determined using SQUEEZE analysis.¹²

A suitable single crystal of **1a**₀ was mounted in a gas cell and activated *in-situ* by heating the crystal at 333 K under dynamic vacuum (2.22×10^{-5} bar). The gas cell was then pressurized to 4.5 bar of CO₂ and the system allowed to equilibrate at this pressure for 12 h. After equilibration, the single crystal data of **1a**·CO₂ were recorded at 298 K (Figure 13). Structure elucidation revealed that **1a**·CO₂ remains in the same space group (monoclinic *P*₂₁/*n*) as **1a**₀ with statistically similar unit cell parameters. The asymmetric unit (ASU) contains one complete TBC4 molecule with one CO₂ molecule (0.50 occupancy) present in the intrinsic cavity. Except for the presence of the CO₂ molecules, the structures of **1a**₀ and **1a**·CO₂ are isoskeletal. Each of the *tert*-butyl groups of the TBC4 molecule is rotationally disordered over two positions. SQUEEZE analysis revealed that there are 44 electrons present per unit cell in **1a**·CO₂, which corresponds to 0.50 CO₂ molecules per TBC4 molecule at 4.5 bar. After recording the single crystal data at 298 K, the pressure was rapidly released from the gas cell and the SCXRD analysis of **1a**·CO₂ was immediately repeated at 100 K. The rationale for releasing the pressure just prior to SCXRD analysis is that the CO₂ gas present in the capillary of the gas cell would freeze at 100 K, thereby introducing powder diffraction lines that would compromise the quality of the single-crystal data. Since it is known that the desorption process is slow, it was reasoned that rapid freezing would “lock” the gas-included structure. Using the abovementioned procedure, it is possible to compare room-temperature gas-loaded structures with those obtained after releasing the gas, followed by immediate exposure to cryogenic conditions. It was anticipated that the low temperature SCXRD data would improve the quality of the structure analyses without affecting the packing arrangements of the molecules. Indeed, the packing arrangement of the molecules does not appear to change at 100 K and better quality data were obtained. At 100 K, only one of the four *tert*-butyl groups of each TBC4 molecule is disordered. SQUEEZE analysis of **1a**·CO₂ at 100 K revealed 80 electrons are present per unit cell, which is equivalent to 0.90 molecules of CO₂ per TBC4 molecule. The occupancy is higher than that at 298 K.

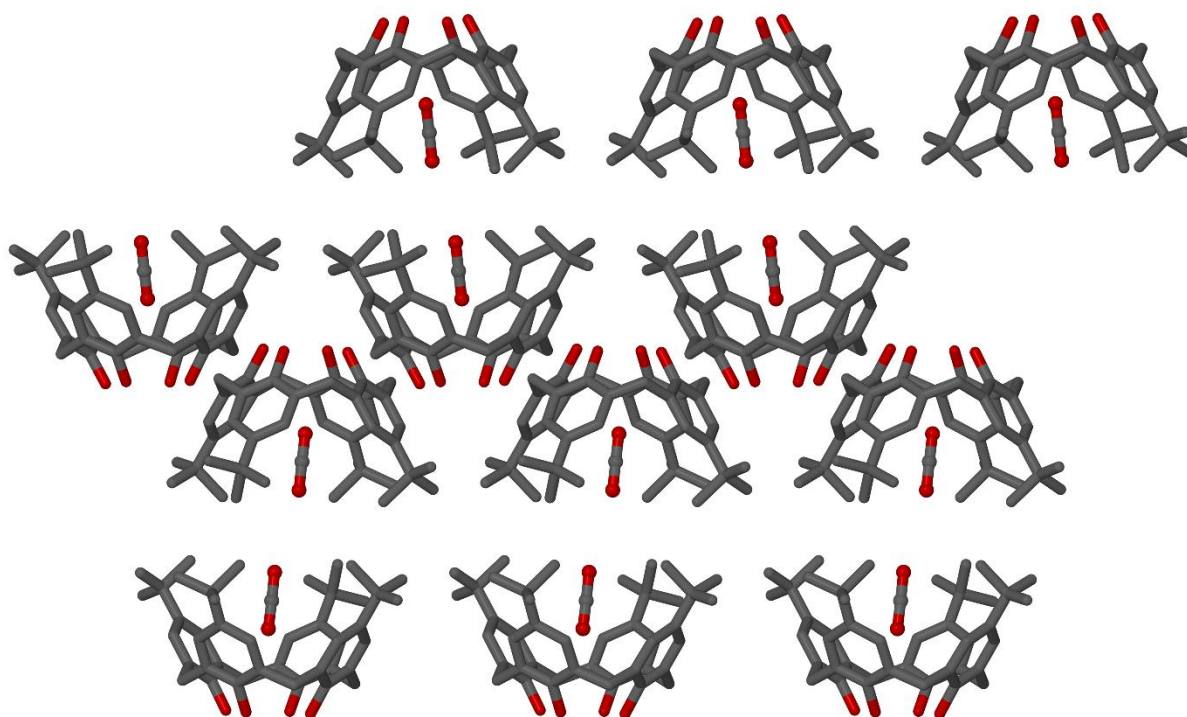
Chapter 3 – *p*-*tert*-Butylcalix[4]arene

Figure 13. The structure of the low pressure (4.5 bar) CO₂ inclusion compound (**1a**·CO₂) at 298 K. Hydrogen atoms and disordered carbon atoms are omitted for clarity.

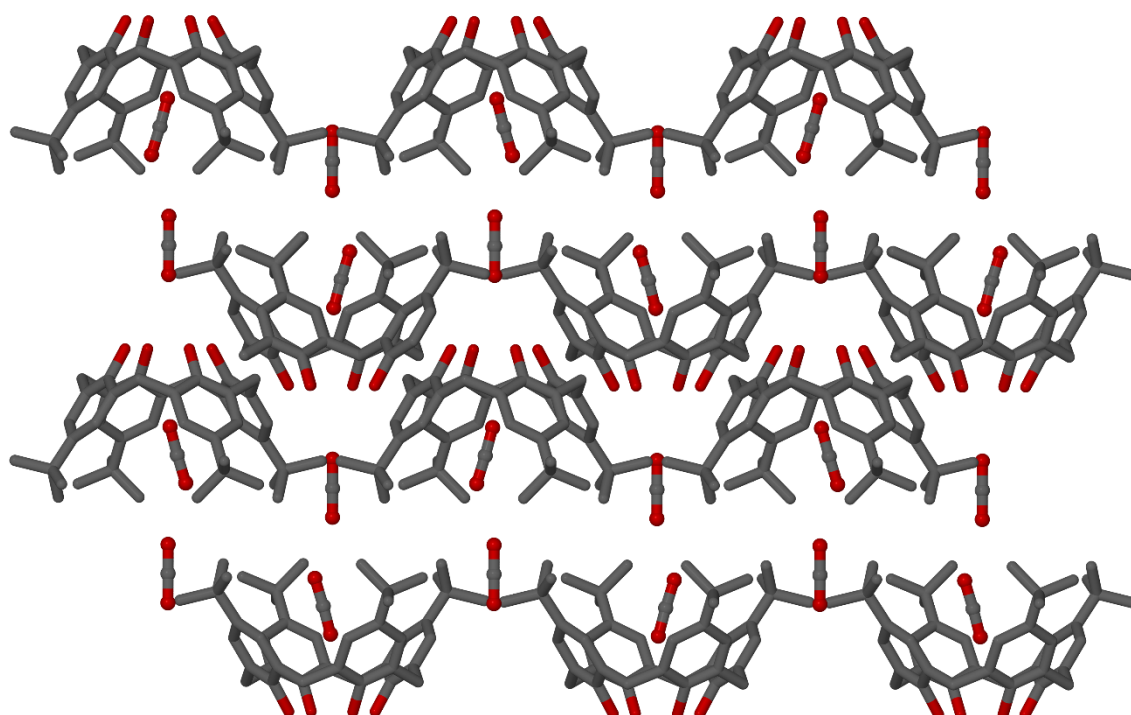


Figure 14. The structure of the high pressure (30 bar) CO₂ inclusion compound (**1c**·CO₂) at 298 K. Hydrogen atoms and disordered carbon atoms are omitted for clarity.

Chapter 3 – p-tert-Butylcalix[4]arene

This could be due to the longer equilibration time at 4.5 bar CO₂ before collecting the single crystal data. This result is consistent with the ideal stoichiometry of 1:1 (CO₂:TBC4), determined by sorption analysis at 22 bar.

The same crystal was then pressurized at 30 bar of CO₂ at 298 K, and allowed to equilibrate at this pressure for 12 h (Figure 14). Although the quality of the single crystal deteriorates at 30 bar, it was still possible to determine the crystal structure. At 30 bar, the compound packs in the tetragonal space group *P4/n* (**1c**) with ¼ of a TBC4 molecule and two crystallographically independent CO₂ molecules (1.68 total occupancy) in the ASU. The TBC4 molecules are arranged in successive ABAB layers along the crystallographic *c* axis. The structure of **1c**·CO₂ contains additional intermolecular cavities (extrinsic cavities) that are situated between four TBC4 molecules of one layer and approximately 4 Å above the intrinsic cavity of a TBC4 molecule in the facing layer. These extrinsic voids allow the accommodation of an additional CO₂ molecule per TBC4 molecule. At 298 K, all of the *tert*-butyl groups of each TBC4 molecule are disordered over two positions. SQUEEZE analysis of **1c**·CO₂ indicated that there are 74 electrons present in the solvent accessible volume in the unit cell, which is equivalent to 1.68 molecules of CO₂ per TBC4 molecule. As in the case of **1a**·CO₂, the low temperature structure of **1c**·CO₂ was determined at 100 K. At 100 K, no disorder is observed for the *tert*-butyl groups. SQUEEZE analysis of **1c**·CO₂ at 100 K showed that there are 84 electrons present per unit cell, which equates to 1.90 molecules of CO₂ per TBC4 molecule. This result agrees well with the ideal stoichiometry of 2:1. The structures of **1a**·CO₂ and **1c**·CO₂ at 100 K are similar to those reported by Udachin *et al.* at 125 K.⁴

Table 1 summarizes the occupancy of the CO₂ molecules per TBC4 molecule in the structures of **1a**·CO₂ and **1c**·CO₂, as calculated from the sorption isotherm and SQUEEZE analyses. For **1a**·CO₂, the sorption and SQUEEZE (100 K) results agree well and are in agreement with the ideal stoichiometry of 1:1 at pressures below 22 bar. For **1c**·CO₂, the SQUEEZE result at 100 K is consistent with the ideal stoichiometry of 2:1 at high pressure. A slight difference in the occupancy is observed with respect to the SQUEEZE and sorption results. This could be associated with the difference in equilibration time allowed at each pressure: The single crystal was left to equilibrate for 12 h whereas each sorption point was assigned an equilibration time of 2 h.

Table 1. The occupancy of CO₂ molecules with respect to one TBC4 molecule in **1a**·CO₂ and **1c**·CO₂.

Analysis	Temperature (K)	Occupancy 4.5 bar	Occupancy 30 bar
Sorption	298	0.87	1.43
SQUEEZE of 1a ·CO ₂	298	0.50	-
	100	0.90	-
SQUEEZE of 1c ·CO ₂	298	-	1.68
	100	-	1.90

3.1.7. Structural analysis of the apohost

In an attempt to determine the crystal structure of **1c**₀, a single crystal that had been exposed to 30 bar CO₂ for 12 h was activated under high vacuum (2.19×10^{-5} bar) at 298 K for two days using a gas cell. After activation the crystal was severely cracked and the single crystal data were of insufficient quality to yield a crystal structure. Since the phase of **1c**·CO₂ is preserved when the CO₂ guests are removed, it can be said that **1c**₀ remains in the tetragonal space group *P4/n*. Considering that **1c**·CO₂ and **1c**₀ are isoskeletal, the estimated guest-accessible void space present in **1c**₀ can be generated by deleting the CO₂ guests from the structure of **1c**·CO₂.¹¹ This “virtually” porous structure is the expected structure of **1c**₀ and it contains large pear-shaped cavities with a calculated volume of 162 Å³ each (Figure 15).

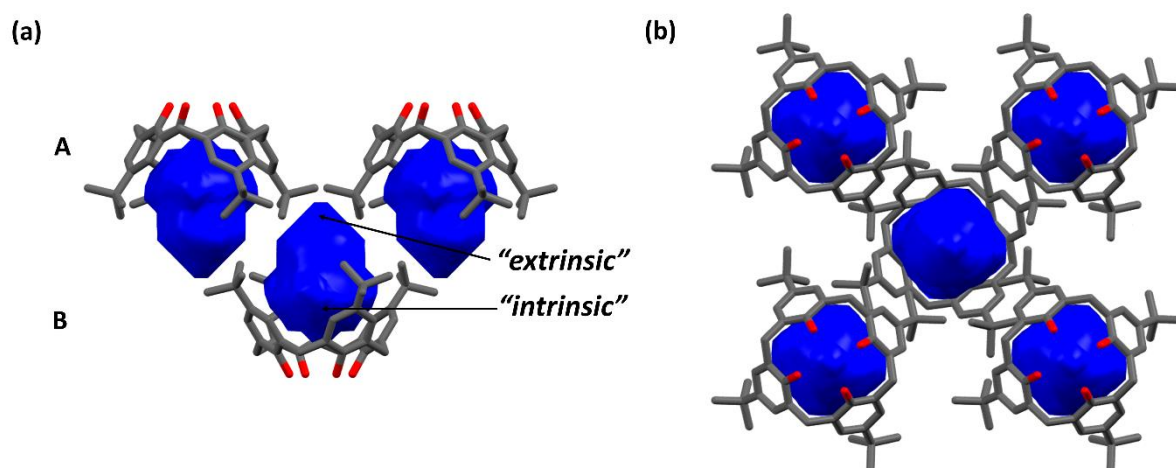


Figure 15. (a) The virtual pear-shaped voids present in **1c**₀ are illustrated in blue. (b) The extension of the cavity from bowl (intrinsic space) of a TBC4 molecule in the B layer into the extrinsic space in the A layer is illustrated.

Chapter 3 – *p*-*tert*-Butylcalix[4]arene

These cavities extend from the bowl formed by each TBC4 molecule (intrinsic space) into the extrinsic space between four TBC4 molecules in the facing layer. Since there are no channels leading to these cavities, the porosity of **1c_o** can be described as zero-dimensional (0D).

3.1.8. Proposed mechanisms for CO₂ transport through the host

The LDP of TBC4 has received much attention in the literature due to the adsorption of CO₂ and other small gas molecules into this seeming non-porous structure. Although **1a_o** only exhibits 0D porosity, the cavities are accessible to guest molecules due to the flexibility of the host material. Computational studies have been carried out in attempts to elucidate gas dynamics within **1a_o**.^{14,15} In 2008, Gu and co-workers¹⁴ suggested two possible mechanisms for the movement of gas molecules through the material based on molecular mechanics calculations:

1. The squeeze mechanism, wherein the guest molecules move through the gaps between the TBC4 molecules until an intrinsic void is reached.
2. The relay mechanism, wherein the dynamic movement of the bilayer allows the guest molecules to move from host to host, until the voids are filled.

Additional computational work by Breite *et al.* in 2010¹⁵ supported the likelihood of the relay mechanism. Furthermore, they suggest that the induced rotation of the *tert*-butyl groups plays a vital role in the movement of the guest molecules through the host material and act as ball-bearings rather than turnstiles. The rotation of the *tert*-butyl groups decreases the effective friction in the material, thereby facilitating the lateral movement of the bilayers and the diffusion of the guests through the host.

3.2. HIGH DENSITY POLYMORPH OF *P*-*TERT*-BUTYLCALIX[4]ARENE

3.2.1. Preparation of the high density polymorph of TBC4

The HDP of TBC4 (**1b_o**) is prepared by heating a sample of the LDP (**1a_o**) at 473 K under dynamic vacuum. The conversion from **1a_o** to **1b_o** was studied using T-DSC up to 533 K. Three events are visible in the T-DSC thermogram of **1a_o** (Figure 16). Between 353-383 K the LDP undergoes a slight structural rearrangement to produce a phase that only persists at high temperature.¹⁶ The broad exothermic peak between 413-478 K represents a further rearrangement from **1a_o** to **1b_o**. This agrees well with the reported phase transformation between 413-463 K.⁹ Upon further heating a third exothermic event occurs as the sample starts to sublime between 483-533 K to yield **1a_o**. The energies associated with these events are 1.34 kJ mol⁻¹, 1.87 kJ mol⁻¹ and 3.31 kJ mol⁻¹, respectively.

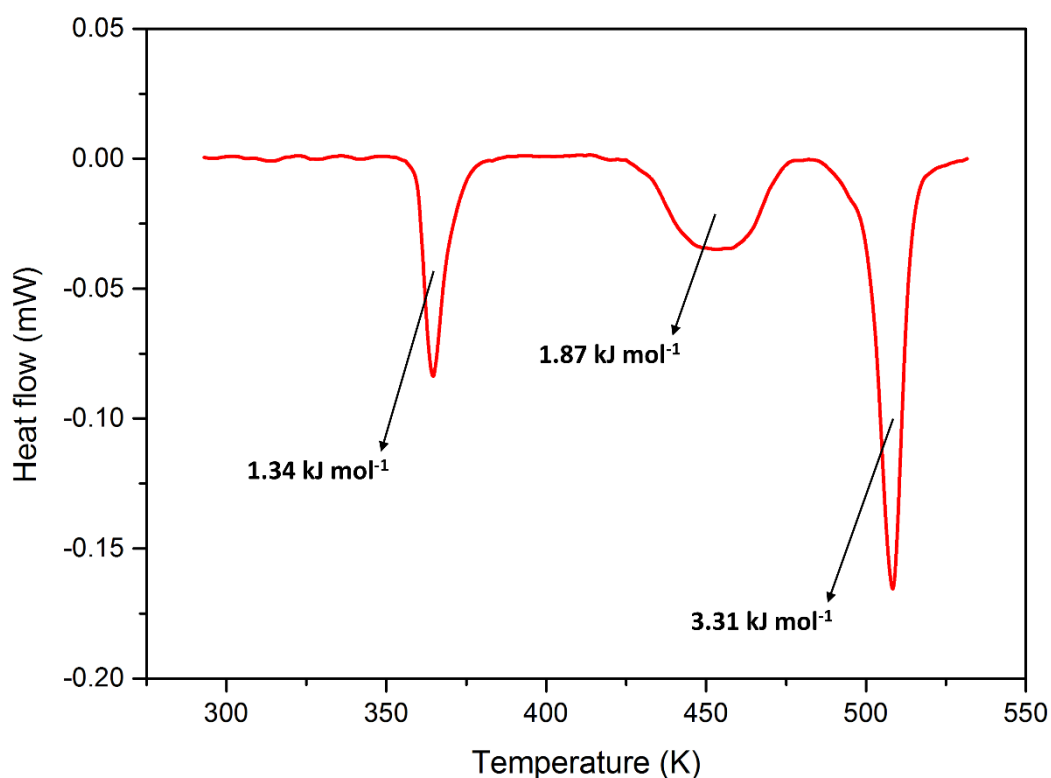


Figure 16. T-DSC thermogram of a guest-free sample of **1a_o** up to 533 K displays three exothermic events with energies of 1.34 kJ mol⁻¹, 1.87 kJ mol⁻¹ and 3.31 kJ mol⁻¹, respectively.

PXRD analysis was used to monitor the phase transformation from **1a_o** to **1b_o** (Figure 17). Initially, the powder pattern of a sample of **1a_o** was recorded at 298 K. Thereafter, the sample was kept in an oven at 473 K under dynamic vacuum and then the powder patterns were recorded at 24 h intervals. After 24 h, the powder pattern had changed significantly as

the sample started to convert to the HDP. However, the peak present at 6.78° also appears in the powder pattern of **1a**, suggesting that the sample contained a mixture of the LDP and HDP. After 72 h, the sample had fully converted to **1b** and matched the powder pattern calculated from the reported HDP structure.⁹ When the sample is heated to 533 K, sublimation starts to occur and **1a** is regenerated.

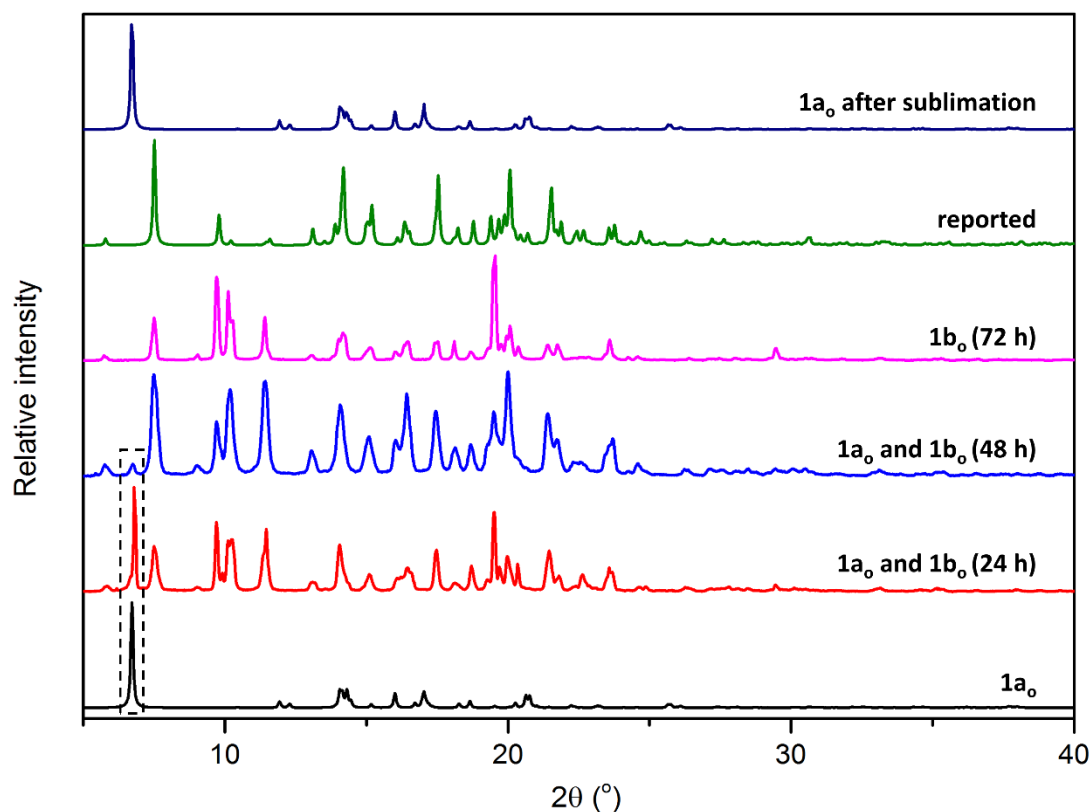


Figure 17. Powder patterns of **1a**, a mixture of **1a** and **1b** after the sample was heated at 473 K for 24 h and 48 h, **1b** after heating for 72 h, the reported structure of **1b** and **1a** regenerated by sublimation.

3.2.2. Structural analysis

SCXRD analysis of **1b** at 298 K revealed that the TBC4 molecules arrange in the monoclinic space group $P2_1/c$ with one complete TBC4 molecule in the ASU. One of the *tert*-butyl groups of each calixarene molecule protrudes into the intrinsic cavity of a neighboring molecule to form an interdigitated dimer. These dimers are closely-packed in repeating AB layers along the *a* axis (Figure 18). The dimers of each layer are displaced vertically along the *a* axis by approximately 9.66 Å (relative to the center of each dimer). At 298 K, all of the *tert*-butyl groups of each TBC4 molecule are rotationally disordered over two positions, whereas none of the *tert*-butyl groups are disordered at 100 K. Although small

contractions in the unit cell parameters are observed at 100 K, the structure remains in the space group $P2_1/c$ and is isoskeletal to the structure determined at 298 K. During the structural transformation from **1a_o** to **1b_o**, the calculated density of the structure increases from 1.024 g cm⁻³ to 1.139 g cm⁻³ at 298 K. Unlike **1a_o**, the closed-packed structure of **1b_o** does not contain any voids and is therefore incapable of accommodating guest molecules without significant rearrangement of the host molecules.

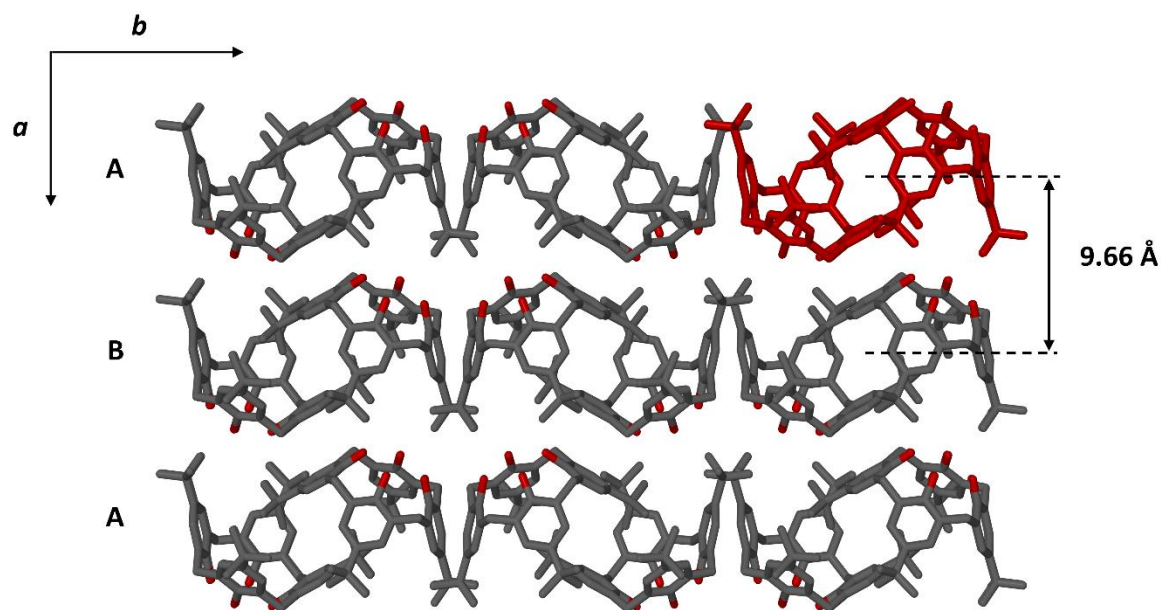


Figure 18. The structure of **1b_o** at 298 K viewed along the crystallographic *c* axis, with an interdigitated dimer indicated in red. The distance between two dimers from layer A and B is 9.66 Å. Disordered carbon atoms and hydrogen atoms have been omitted for clarity.

3.2.3. Thermal analysis

Figure 19 contains the TGA thermogram of a sample of **1b_o** that had been exposed to air for four weeks. The sample only loses 1% of its initial mass before sublimation starts to occur during the large step observed at 533 K. As a result of close-packing and the lack of voids, **1b_o** appears to be atmospherically inert and does not adsorb atmospheric gases as in the case of **1a_o**.

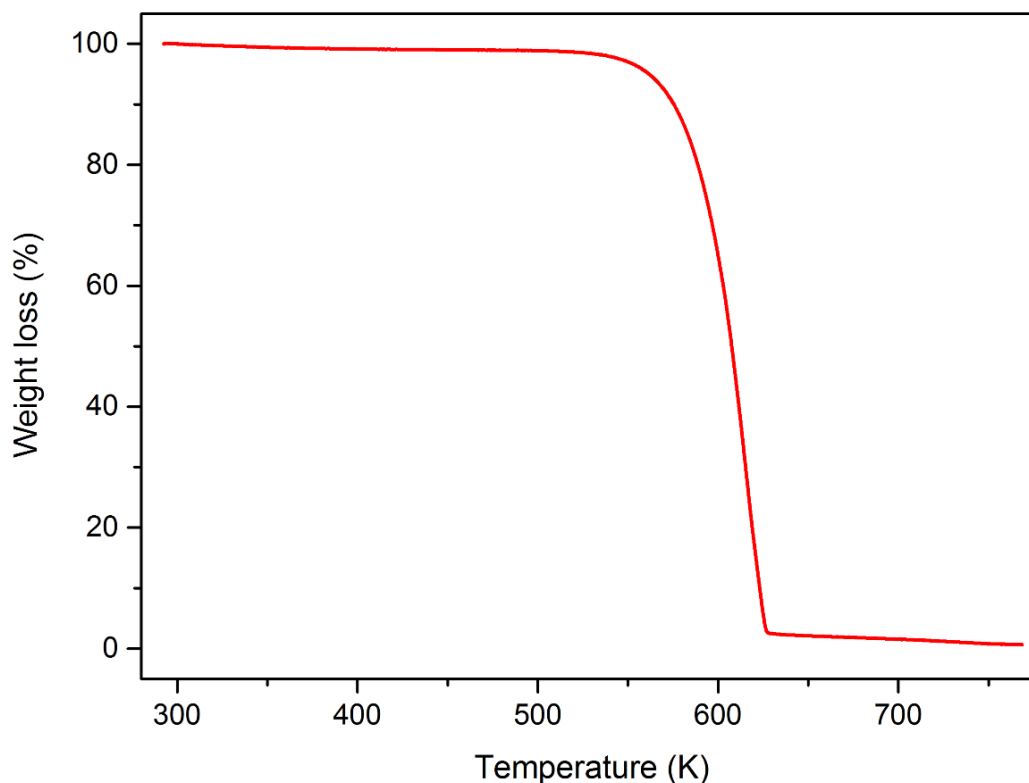


Figure 19. TGA thermogram of **1b₀** after being exposed to air for four weeks.

3.2.4. Interactions between the HDP of TBC4 and CO₂

Although **1b₀** does not contain any channels or voids to facilitate the movement of guests through the material, Thallapally *et al.* reported that the HDP of TBC4 undergoes a gas-induced structural transformation to the LDP at high CO₂ pressure.⁹ This transformation was further investigated using P-DSC, volumetric sorption analysis and VP-PXRD.

P-DSC was used to scan a sample of **1b₀** from 1-50 bar at 298 K using CO₂ gas (Figure 20). A large exothermic event occurs with an onset pressure of 35 bar, and represents the gas-induced transformation from **1b₀** to the LDP. The energy involved in the transformation (CO₂ sorption + structural change) is ~23.88 kJ mol⁻¹.

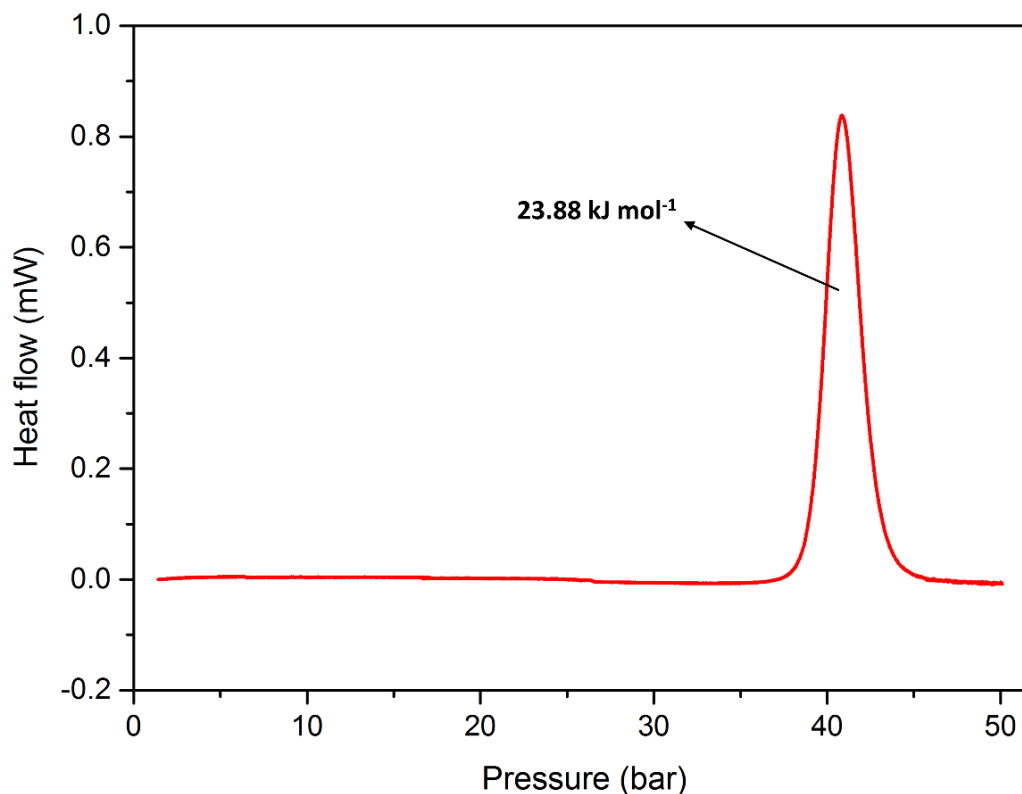


Figure 20. P-DSC plot of **1b₀** at 298 K displaying a $\sim 23.88 \text{ kJ mol}^{-1}$ transformation to the LDP at 35 bar of CO₂.

Volumetric sorption analysis was carried out on **1b₀** up to 52 bar using CO₂ gas at 298 K. The CO₂ sorption isotherm of **1b₀** is depicted by the red curve in Figure 21. From 0-34 bar, the sample remains in the close-packed high density phase, resulting in a negligible amount of CO₂ being adsorbed. In agreement with the P-DSC result, a large step is visible at 35 bar in the sorption isotherm. This step represents the transformation from **1b₀** to a low density phase capable of adsorbing CO₂ (**1c**). At 52 bar, 1.38 molecules of CO₂ (2.12 mmol g⁻¹) were adsorbed per TBC4 molecule. However, from the isotherm it appears that the uptake of CO₂ is still occurring at 52 bar. This could be due to the very slow kinetics of CO₂ sorption by the low density phase. As a result, the concentration of CO₂ further increases during the first few points in the desorption cycle. A maximum CO₂ concentration of 2.20 mmol g⁻¹ is reached at 44 bar, which is equivalent to 1.43 molecules of CO₂ per TBC4 molecule. This result is comparable to the maximum concentration reached by **1c**·CO₂ (1.44 CO₂:1 TBC4) during the volumetric sorption analysis of **1a₀** at 298 K (Section 3.1.4). No step was observed during the desorption, suggesting that the sample remains in the low density phase **1c** until vacuum is reached.

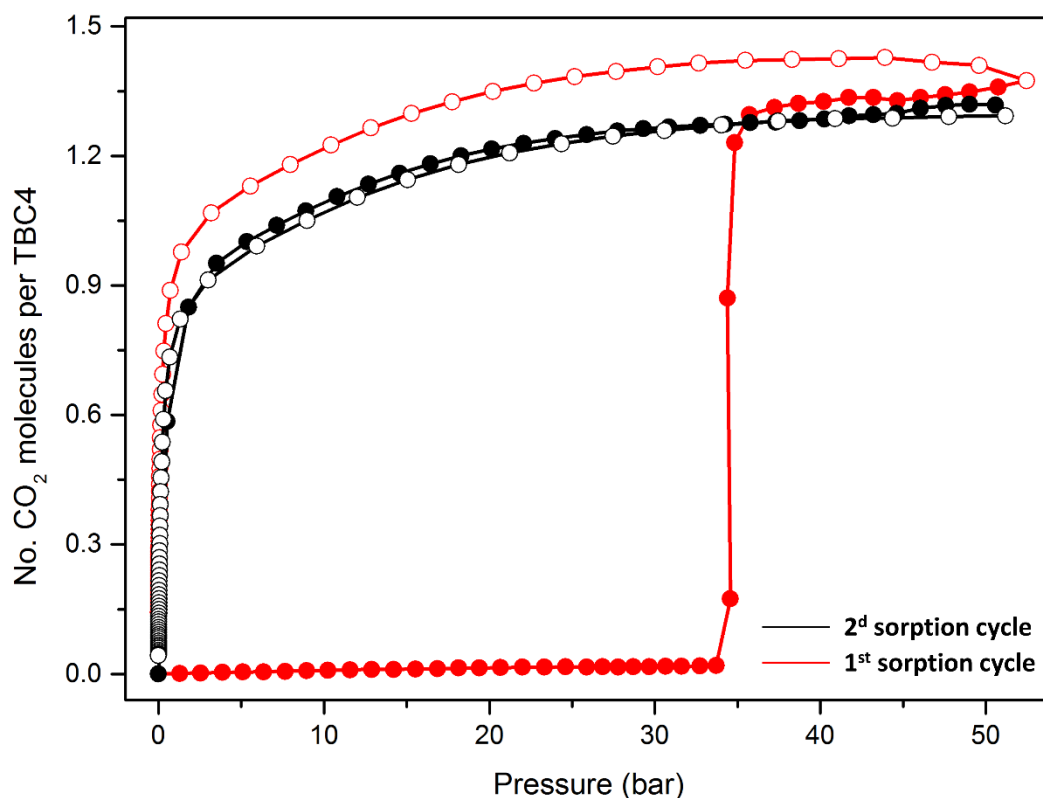


Figure 21. The first (red) and second (black) CO₂ sorption isotherm cycles of **1b₀** measured at 298 K. The filled circles represent the adsorption cycle and the open circles represent the desorption cycle.

A second sorption cycle was performed using the same sample in order to confirm that the same phase is preserved. The sample was evacuated *in-situ* at 298 K for 24 h prior to the second cycle. The sorption isotherm is indicated by the black curve in Figure 21. The adsorption and desorption of CO₂ follows a type I isotherm. Since the sorption of CO₂ occurs in one step, it is conclusive that no structural transformations occur and the sample remains in the same phase. During the second sorption cycle a maximum CO₂ concentration of 2.03 mmol g⁻¹ is reached at 50 bar, which equates to 1.32 molecules of CO₂ per TBC4 molecule. The maximum uptake is slightly lower than the amount absorbed during first sorption cycle (1.43 CO₂ molecules), but agrees well with the amount adsorbed during the second sorption cycle of **1a₀** at 298 K (1.33 CO₂ molecules).

The gas-induced phase transformation of **1b₀** was further investigated using VP-PXRD. The powder pattern of **1b₀** was recorded at 298 K under static vacuum by using an environmental gas cell. Thereafter, the sample was loaded with CO₂ in steps of 5-10 bar and was allowed to equilibrate at each pressure for 4 h. The powder pattern of the sample was recorded at each pressure at 298 K to monitor the transformation from **1b₀** to the LDP. Figure 22 illustrates the change in the powder pattern of the sample as the pressure is increased.

Over the pressure range of 0-20 bar the powder pattern remains unchanged. At 25 bar, the sample contains a mixture of the HDP and LDP, which is indicated by the presence of a new peak at 6.82°. By 30 bar, the sample had fully converted to the LDP and no further changes in the powder pattern are observed at 50 bar of CO₂. Unlike in the case of P-DSC and the sorption analysis, the transformation occurred before 35 bar. A possible reason for this is the longer equilibration time (4 h) allowed as compared to the sorption experiment (1.5 h). The powder pattern of the low density form matches that of **1c**·CO₂ (Section 3.1.5), which suggests that **1b**₀ converts to **1c**·CO₂ under CO₂ pressure.

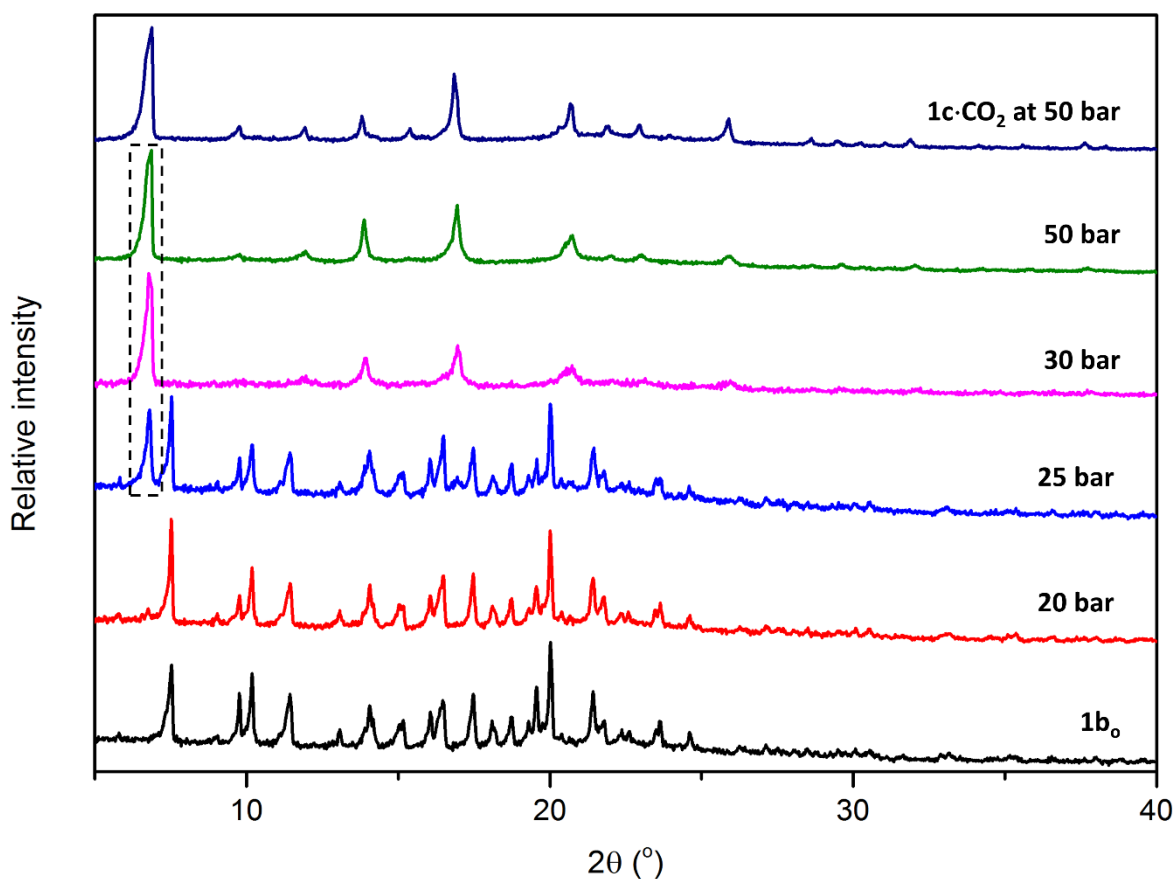


Figure 22. Powder pattern of **1b**₀ under static vacuum, as well as at pressures of 20, 25, 30 and 50 bar, and **1c**·CO₂ at 50 bar.

3.2.5. Structural analysis of **1b**₀ under CO₂ pressure

In order to gain a better understanding of the gas-induced structural transformation that occurs, *in-situ* SCXRD analysis was used to investigate the structures of **1b**₀ at 15 and 40 bar of CO₂.

A single crystal of **1b_o** was mounted in a gas cell, which was then pressurized to 15 bar of CO₂ and allowed to equilibrate at this pressure for 7 h. SCXRD analysis at 298 K revealed that no change had occurred and that the structure remains in the monoclinic space group *P*2₁/*c*. As expected from the sorption result, no CO₂ molecules could be modelled in the structure.

The gas cell was then pressurized to 40 bar of CO₂ in order to determine the structure after the phase transformation had occurred. After the crystal had equilibrated at this pressure for 7 h, the single crystal data were recorded at 298 K. Unfortunately, the single crystal did not survive the structural transformation intact. Although it was not possible to determine the crystal structure from the diffraction data, its unit cell parameters are reminiscent to that of **1c·CO₂** at 298 K (Table 2). There is a large difference between the unit cell values of **1c·CO₂** and **1b_o** (40 bar), however it is not possible to account for the differences in the absence of a crystal structure.

Table 2. Comparison of the unit cell parameters of **1c·CO₂** and **1b_o** (40 bar) at 298 K.

Parameter	1c·CO₂	1b_o (40 bar)
Crystal system	Tetragonal	Tetragonal
<i>a</i> (Å)	12.8774(7)	13.73
<i>b</i> (Å)	12.8774(7)	13.73
<i>c</i> (Å)	12.8890	13.65
Volume (Å ³)	2137.33(16)	2575

3.2.6. Proposed mechanism for CO₂-induced phase transformation

Unlike the structure of the LDP of TBC4, the HDP does not contain large intrinsic voids capable of housing guest molecules. These dimers are arranged in a close-packed fashion and provide no apparent pathway that would allow the movement of guests through the host material. It is highly probable that the *tert*-butyl groups play a significant role in allowing the passage of CO₂ molecules through the host material. This requires cooperative movement of the AB layer within the structure, which is made possible by the rotation of the *tert*-butyl groups. At 35 bar, the forces exerted by the CO₂ molecules are large enough to initiate the expansion of the crystal lattice to produce **1c·CO₂**.

3.3. SUMMARY

Structural analysis of the LDP of TBC4 (**1a_o**) indicated that the overall structure is held together by weak van der Waals interactions. Furthermore, the structure contains large isolated cavities (275 Å³ each) that are present in the bowls formed by each TBC4 molecule. Despite the 0D porosity of this host, it has been shown that these cavities are accessible to CO₂ guest molecules. The CO₂ sorption isotherm contained two steps. The second step represents a structural transformation to phase **1c·CO₂**. No step is observed during desorption, suggesting that the porous phase of **1c** is preserved even after vacuum had been reached. The sorption cycles were repeated to confirm that the phase of **1c** was preserved and that **1a_o** can be regenerated by activation under mild conditions. These findings are also supported by P-DSC, T-DSC and VP-PXRD. *In-situ* SCXRD analysis of **1a·CO₂** (at 4.5 bar CO₂) and **1c·CO₂** (at 30 bar CO₂) revealed that additional extrinsic cavities are generated during the gas-induced structural transformation to **1c**. The ideal stoichiometries before and after the structural transformation are 1:1 (CO₂:TBC4) and 2:1, respectively. The ideal stoichiometries can only be achieved at low temperature, due to the slow kinetics of sorption at room temperature.

The LDP of TBC4 converts to the HDP (**1b_o**) by means of a temperature-induced structural transformation when heated up to 473 K under dynamic vacuum. Unlike **1a_o**, the close-packed structure of **1b_o** consists of interdigitated TBC4 dimers and lacks intrinsic and extrinsic cavities. The CO₂ sorption isotherm of **1b_o** indicates that the HDP is unable to adsorb CO₂. However, at 35 bar the sample undergoes a gas-induced transformation to a low density phase and the uptake of CO₂ starts to occur. A second sorption cycle was performed to confirm that this phase is preserved, even after all of the CO₂ molecules had been removed. VP-PXRD was used to confirm that **1b_o** converts to **1c·CO₂** at 35 bar. As a result of this large molecular reorganization, the single crystal of **1b_o** does not survive the transformation and the single crystal structure of **1b_o** could not be determined at 40 bar. However, the unit cell parameters were reminiscent to that of **1c·CO₂** at 298 K.

For both **1a_o** and **1b_o**, all *tert*-butyl group of each TBC4 molecule are rotationally disordered over two positions at 298 K. At 100 K, one of the *tert*-butyl groups of each TBC4 molecule are disordered in the case of **1a_o**, whereas none of the *tert*-butyl groups are disordered in the case of **1b_o**. It is likely that the *tert*-butyl groups play a role in the dynamic nature of these hosts. It has been considered that the rotation of the *tert*-butyl groups induces

Chapter 3 – p-tert-Butylcalix[4]arene

cooperative movement of the layer or bilayers in these host materials. For **1a_o**, this allows the guest molecules to pass through the material until the isolated cavities are filled. Similarly for **1b_o**, the pressure exerted by the CO₂ molecules at 35 bar induces a structural expansion to **1c·CO₂**.

REFERENCES

1. Gutsche, C. D. Calixarenes, In *Monographs in Supramolecular Chemistry*; The Royal Society of Chemistry: Cambridge, 1989.
2. Andreetti, G. D.; Ungaro, R.; Pochini, A. *J. Chem. Soc., Chem. Commun.*, **1979**, 1005.
3. (a) Atwood, J. L.; Barbour, L. J.; Jerga, A. Schottel, B. L. *Science*. **2002**, 298, 1000; (b) Enright, G. D.; Udachin, K. A.; Ripmeester, J. A. *Chem. Commun.* **2004**, 1360; (c) Thallapally, P. K.; Wirsig, T. B.; Barbour, L. J.; Atwood, J. L. *Chem. Commun.* **2005**, 4420; (d) Karotsis, G.; Teat, S. J.; Wernsdorfer, W.; Piligkos, S.; Dalgarno, S. J.; Brechin, E. K. *Angew. Chem. Int. Ed.*, **2009**, 48, 8285; (e) Ramon, G.; Jacobs, A.; Nassimbeni, L. R.; Yav-Kabwit, R. *Cryst. Growth Des.* **2011**, 11, 3172.
4. Udachin, K. A.; Moudrakovski, I. L.; Enright, G. D.; Ratcliffe, C. I.; Ripmeester, J. A. *Phys. Chem. Chem. Phys.* **2008**, 10, 4636.
5. (a) Brouwer, E. B.; Udachin, K. A.; Enright, G. D.; Ratcliffe, C. I.; Ripmeester, J. A. *Chem. Commun.* **1998**, 587. (b) Udachin, K. A.; Brouwer, E. B.; Enright, G. D.; Ripmeester, J. A. *J. Supramol. Chem.* **2001**, 1, 97; (c) Brouwer, E. B.; Udachin, K. A.; Enright, G. D.; Ripmeester, J. A.; Ooms, K. J.; Halchuk, P. A. *Chem. Commun.* **2001**, 565.
6. Atwood, J. L.; Barbour, L. J.; Jerga, A. *Chem. Commun.* **2002**, 2952.
7. Brouwer, E. B.; Enright, G. D.; Udachin, K. A.; Lang, S.; Ooms, K. J.; Halchuk, P. A.; Ripmeester, J. A. *Chem. Commun.* **2003**, 1416.
8. Enright, G. D.; Udachin, K. A.; Moudrakovski, I. L.; Ripmeester, J. A. *J. Am. Chem. Soc.* **2003**, 125, 9896.
9. Thallapally, P. K.; McGrail, B. P.; Dalgarno, S. J.; Schaef, H. T.; Tian, J.; Atwood, J. L. *Nat. Mater.* **2008**, 7, 146.
10. Shah, R. B.; Valand, N. N.; Sutariya, P. G.; Menon, S. K. *J. Incl. Phenom. Macrocycl. Chem.*, **2016**, 84, 173.
11. Atwood, J. L.; Barbour, L. J.; Jerga, A. Schottel, B. L. *Science*. **2002**, 298, 1000.
12. Spek, A. L. *Acta Cryst.* **2009**, D65, 148.
13. Barbour, L. J. *Chem. Commun.* **2006**, 1163.

Chapter 3 – p-tert-Butylcalix[4]arene

14. Gu, X.; Zhang, L.; Gong, X.; Lau, W. M.; Liu, Z. F. *J. Phys. Chem. B.* **2008**, *112*, 14851.
15. Breite, M. D.; Coz, J. R.; Adams, J. E. *J. Am. Chem. Soc.* **2010**, *132*, 10996.
16. Atwood, J. L.; Barbour, L. J.; Lloyd, G. O.; Thallapally, P. K. *Chem. Commun.* **2004**, 922.

Chapter 4

Cucurbit[6]uril

Cucurbit[6]uril was first reported in 1905 by Behrend *et al.* as the product formed by the condensation reaction between glycoluril and formaldehyde.¹ In 1981, it was revealed that this product consists of six glycoluril units bound together by twelve methylene groups to form a six-membered macrocycle.² Owing to its pumpkin (belonging to the *cucurbitaceae* botanical family) shape, this macrocycle was named “cucurbituril”.

Between 2000 and 2002 it was discovered that a variety of cucurbituril homologues can be synthesized under slightly modified reaction conditions.³ These homologues were called cucurbit[5]uril, cucurbit[6]uril, cucurbit[7]uril, cucurbit[8]uril and cucurbit[10]uril, based on the number of glycoluril units in the macrocycle. The largest cucurbituril known to date, cucurbit[14]uril, was reported in 2013.⁴ Various functionalized cucurbituril homologues have also been synthesized recently.⁵

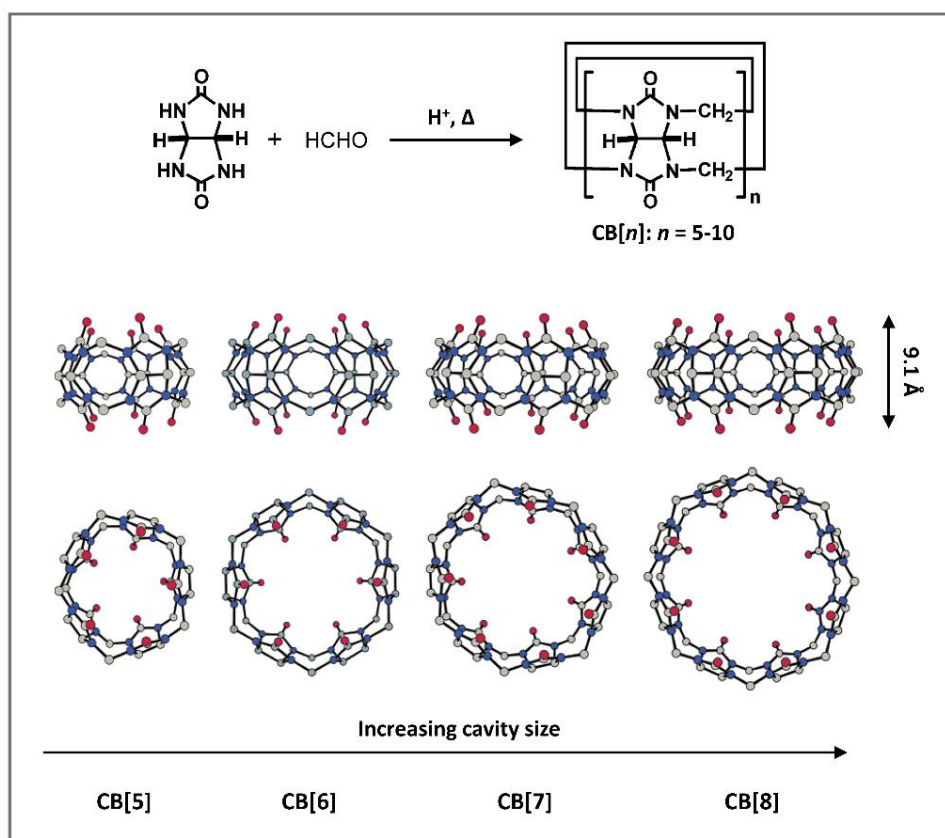


Figure 1. The acid condensation reaction between glycoluril and formaldehyde producing CB[n] (n = 5-10). Image reproduced from Barrow *et al.*⁶

Chapter 4 – Cucurbit[6]uril

Compared to other macrocyclic hosts, the cucurbiturils have very rigid structures. Although the heights of the cucurbituril homologues are the same (9.1 Å), the sizes of their inner cavities range from 82-870 Å³ (Table 1), resulting in different affinities for a large variety of guest molecules.⁶

Table 1. Structural parameters of CB[5]-CB[10]. Portal diameter refers to the diameter of the carbonyl rims and cavity diameter refers to the inner diameter of the CB[n] macrocycle.

	Portal diameter (Å)	Cavity diameter (Å)	Outer diameter (Å)	Cavity volume (Å ³)	Height (Å)
CB[5]	2.4	4.4	13.1	82	9.1
CB[6]	3.9	5.8	14.4	164	9.1
CB[7]	5.4	7.3	16.0	279	9.1
CB[8]	6.9	8.8	17.5	479	9.1
CB[10]	9.5-10.6	11.3-12.4	20.0	870	9.1

Table reproduced from Barrow *et al.*⁶

The cucurbiturils show a preference towards hydrophobic guests due to the hydrophobicity of their macrocyclic cavities. The partially negatively charged carbonyl rims of the glycoluril units cause these hosts to have a very high quadrupole moment and allows for higher-order electrostatic interactions in the overall packing arrangement.⁷ Figure 2 displays an electrostatic potential map of a cucurbit[7]uril macrocycle⁵ to illustrate the high electron density on the carbonyl regions and the resulting quadrupole moment.

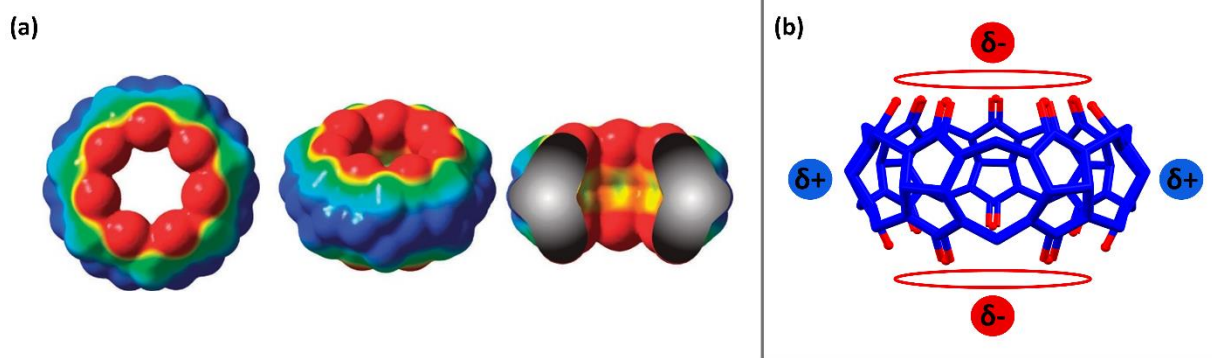


Figure 2. (a) The electron density map of cucurbit[7]uril as reported by Assaf *et al.*⁵ (b) The electronegative carbonyl oxygen atoms are indicated in red and the electropositive cucurbituril ring is indicated in blue. The resulting quadrupole of cucurbit[7]uril is also shown.

Chapter 4 – Cucurbit[6]uril

Cucurbiturils have found many uses in supramolecular chemistry, given their ability to act as molecular containers in various host-guest complexes. Cucurbiturils have proven to be excellent candidates for gas storage due to their exceptionally high thermal and chemical stability. Sorption studies include the encapsulation of greenhouse gases⁸, noble gases⁹ and industrially important gases¹⁰ and have demonstrated gas uptake capabilities comparable^{8a} to PCPs and MOFs.

In this chapter the CO₂ sorption capacity of cucurbit[6]uril (CB[6]) is discussed. CB[6] has been subjected to several studies of host-guest chemistry in solution, but less so in the solid state. CB[6] has demonstrated a high capacity for CO₂ storage and competes with MOFs such as [Pd(2-pymo)₂]_n and HKUST-1 in that regard.^{8a} The high affinity of CB[6] for CO₂ prompted us to investigate the interactions between CB[6] and CO₂ in the solid state. This chapter describes the transformation of the hydrochloride hydrate of CB[6] to a more stable form of CB[6]. The CO₂ inclusion compounds were studied in order to rationalize the high selectivity and exceptional stability of this host.

4.1. SYNTHESIS AND CRYSTALLIZATION

A variety of syntheses of cucurbiturils exist in the literature.^{3,11} Typically, the synthesis yields a mixture of cucurbituril homologues, which then need to be purified by relying on their solubility differences. The procedure of fractional recrystallization can be time consuming and often produces extremely low yields of the desired product. Many literature procedures have been modified in order to produce a targeted homologue as the main or only product. In this work, the method reported by Walker *et al.*^{11a} was used to synthesize CB[6] as the only product.

The crystallization method used during this study allowed the growth of CB[6] crystals within a few hours. The CB[6] precipitate was dissolved in a minimum amount of concentrated HCl (37%) at 333 K. The solution was stirred for 3 h at 353 K and then left to cool to room temperature. As the solution starts to cool down, CB[6] crystallizes from the saturated solution in the form of hydrochloride hydrate crystals. If no crystals were formed, the solution was again heated to 353 K for 3 h before allowing it to cool down.

4.2. CB[6] HYDROCHLORIDE HYDRATE

4.2.1. Structural analysis

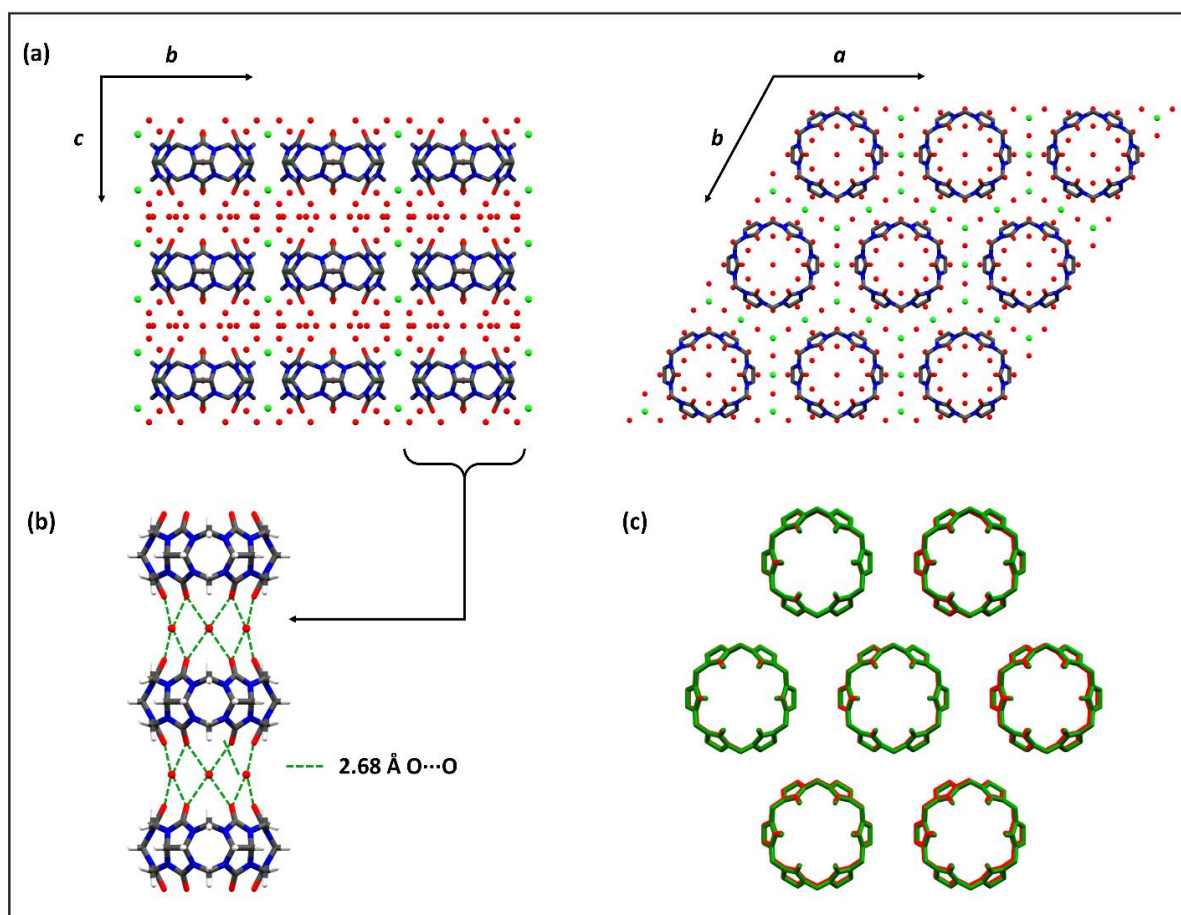


Figure 3. (a) A view of the structure of **2a** along the crystallographic *a* axis (left) and *c* axis (right). (b) A columnar stack of CB[6] molecules held together by hydrogen bonds (green dashed lines) with surrounding water molecules. (c) An overlay of the structure of **2a** (green) and the reported structure¹² (red).

SCXRD analysis of the hydrochloride hydrate of CB[6] (**2a**) at 100 K revealed that the compound crystallizes in the hexagonal space group *P6/mmm*. The structure contains eight chloride anions and 36 water molecules per CB[6] molecule. The CB[6] molecules are arranged in stacks along the *c* axis to produce one dimensional columns (Figure 3a). The CB[6] columns are held together by strong hydrogen bonds (2.68 Å, D...A) with the surrounding water molecules. The carbonyl oxygen atoms of the CB[6] macrocycles act as hydrogen bond acceptors, while the methylene groups act as hydrogen bond donors to surrounding water molecules (Figure 3b). Chloride anions are located between the columns as well as between adjacent CB[6] molecules. The negative charges on the chloride ions are counterbalanced by hydronium cations (H₃O⁺). However, the positions of the hydronium ions

Chapter 4 – Cucurbit[6]uril

could not be determined due to the inability to accurately determine the positions of hydrogen atoms using SCXRD. It is therefore impossible to distinguish between water molecules and hydronium ions in this structure.

The structure of **2a** is the same as that of CB[6] reported in the literature (Figure 3c), except for the difference in water and chloride content.¹² A structural comparison revealed that both structures crystallize in the hexagonal space group $P6/mmm$ and have similar unit cell parameters. The CB[6] macrocycles adopt the same arrangement in all three dimensions and the structures are therefore isoskeletal. The reported structure contains two chloride anions and 34 water molecules (and 2 hydronium ions) whereas in **2a** eight chloride anions and 36 water molecules are present. The difference in water and chloride content is reflected by subtle differences in their powder diffraction patterns (Figure 4). The peak present at 8.40° (Miller index (0 0 1)) in the simulated powder pattern of the literature structure does not appear in the simulated powder pattern of **2a**.

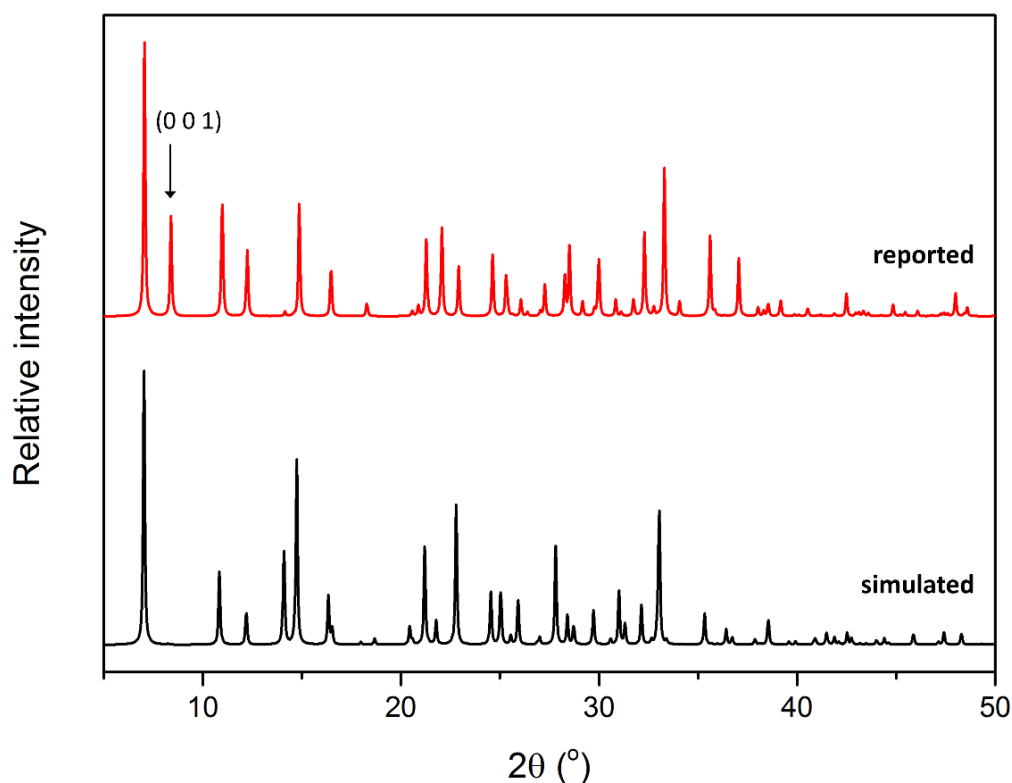


Figure 4. The reported (top) and simulated (bottom) powder diffraction patterns of **2a**.

4.2.2. Thermal analysis

The structure of **2a** has a very high water content: 32% (by weight) of the structure consists of water molecules and a sixth of these water molecules participate in hydrogen bonding that keeps the columnar structure intact. As a result, the structure becomes fragile upon loss of water molecules and visible cracks start to appear in the crystals when they are exposed to air at ambient conditions. Closer inspection revealed that the large block-like crystals of **2a** break down into smaller rod-shaped crystals as a phase transformation occurs during solvent loss (Section 4.3).

The loss of solvent and the phase transformation of **2a** was investigated using TGA and T-DSC. The TGA and T-DSC thermograms are given in Figures 5 and 6, respectively. Three weight loss steps are observed in the TGA thermogram of **2a**. The first weight loss step of ~30% starts at ambient temperature and is completed by 473 K. This step represents the loss of eight chloride anions (as HCl) and 22 water molecules. A similar weight loss was observed when the experiment was repeated. Based on the water and acid content from the SCXRD analysis, the weight loss is expected to be 46%. The difference is most likely due to the rapid loss of water molecules during sample preparation. The high thermal stability of CB[6] is demonstrated by the stepwise decomposition at 623 K.

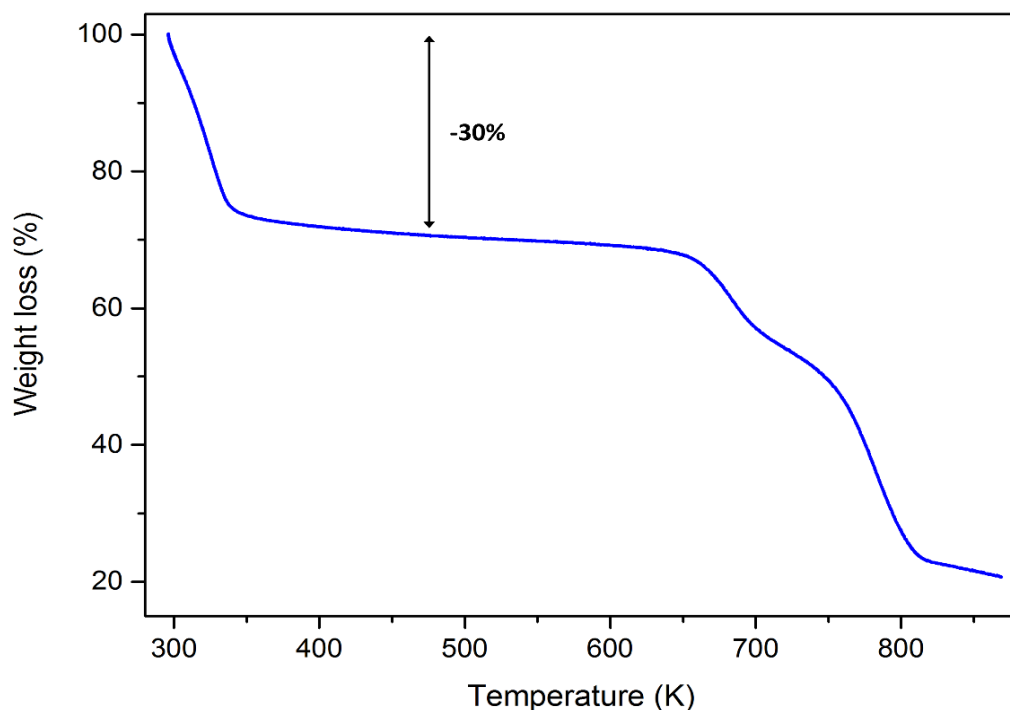


Figure 5. TGA thermogram of **2a** from ambient to 873 K.

Chapter 4 – Cucurbit[6]uril

The characteristic T-DSC profile of **2a** contains two main thermal events. When the sample is heated, an exothermic event is visible in the range of 273-361 K. Directly thereafter a large endothermic event starts to occur and reaches completion at 573 K. In order to gain a better understanding of what happens to the sample during solvent loss, a single crystal of **2a** was filmed over time (Video S1) as the mother liquor was allowed to evaporate (Figure 6, top). During the first thermal event, the large crystals of **2a** appear to melt as solvent and anion loss occurs, yielding an amorphous-looking material of CB[6] (**2a'**). Shortly thereafter an intermediate phase of CB[6] (**2a'**) forms as thin rectangular plates. However, **2a'** is short-lived and converts to another phase of CB[6] (**3a**) during the second thermal event. This last conversion occurs very rapidly and could not be recorded. The two main thermal events are evidenced by several peaks. The occurrence of several peaks is perhaps related to the large difference in size of the crystals. This causes larger crystals of **2a** to undergo the melt and transform at slightly higher temperatures as compared to smaller crystals. Although **2a'** could not be isolated, the crystal of **3a** are extremely stable and were further investigated.

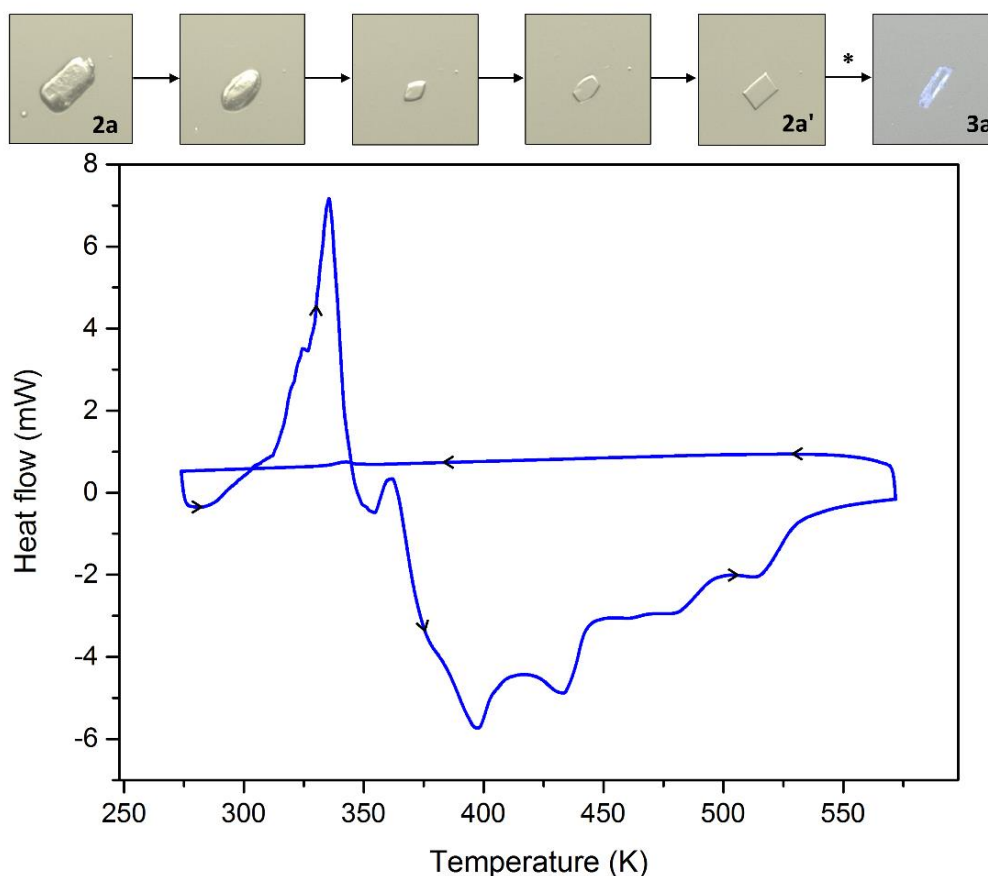


Figure 6. T-DSC thermogram of **2a** in the range of 273-573 K. The conversion from **2a**→**2a'**→**3a** is also shown. *The image of **3a** was not captured during this recording, since the conversion from **2a'** to **3a** occurs too rapidly.

4.3. CB[6] HYDRATE

4.3.1. Preparation of 3a

The crystals of **3a** can easily be prepared from **2a**, since **2a** naturally converts to **3a** over time at ambient conditions (Figure 7). This process can be accelerated by heating a sample of **2a** at 373 K for 24 h. A solvated form of **3a** can also be obtained by recrystallizing **2a** from aqueous HCl or H₂SO₄. In this study hydrated crystals of **3a** were recrystallized from **2a** using 8 M aqueous HCl.

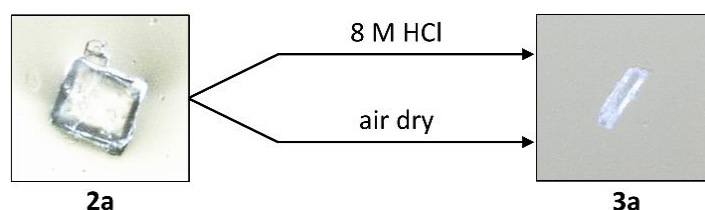


Figure 7. Single crystals of **3a** can be prepared by recrystallizing **2a** from 8 M HCl, or by air drying **2a** at ambient conditions.

4.3.2. Structural analysis

SCXRD analysis of a suitable crystal of **3a** revealed that the compound crystallizes in the trigonal space group $R\bar{3}$. The CB[6] molecules adopt a hexagonal arrangement, producing a honeycomb structure with 1D channels along the *c* axis (Figure 8).

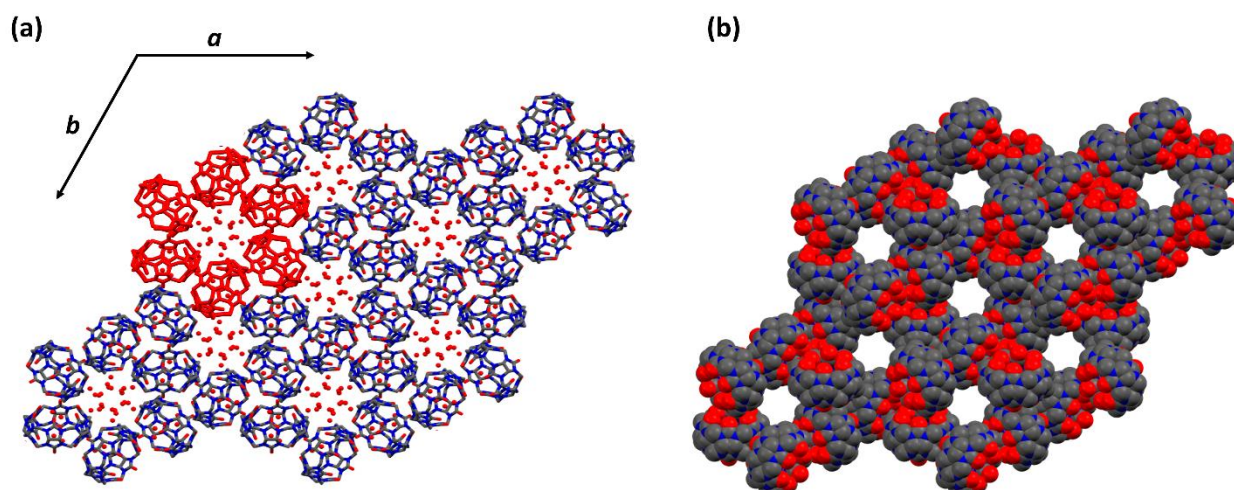


Figure 8. (a) A view of the structure of **3a** along the *c* axis illustrating the 1D channels filled with water molecules. The hexagonal arrangement of six CB[6] molecules is shown in red. (b) A space-filling representation of the honeycomb structure with 1D channels (water molecules have been omitted).

Chapter 4 – Cucurbit[6]uril

The structure of **3a** has previously been reported in the literature.¹⁰ Unlike **2a**, the structure of **3a** does not contain chloride anions. The water content is also much lower, with a total of fourteen water molecules per CB[6] molecule. Eight of these water molecules are located within the 1D channels. The remaining six water molecules are included inside the macrocyclic cavity: four of these molecules are arranged in the hydrophobic region of the cavity, while the other two water molecules are each hydrogen bonded (2.80-2.96 Å) to three oxygen atoms belonging to the carbonyl rims of the macrocycle (Figure 9). Four carbonyl oxygen atoms of each rim participate in C-H \cdots O hydrogen bonding (3.45-3.52 Å, C \cdots O) with the methine and methylene groups of four neighboring CB[6] macrocycles, producing a slanted square-planar unit (Figure 9).¹⁰ As a result of this self-closing arrangement, the portals of each CB[6] macrocycle are blocked by two adjacent macrocycles, trapping the six water molecules that are included inside the cavity. The three-dimensional arrangement of these square-planar units produces the honeycomb network with 1D channels.

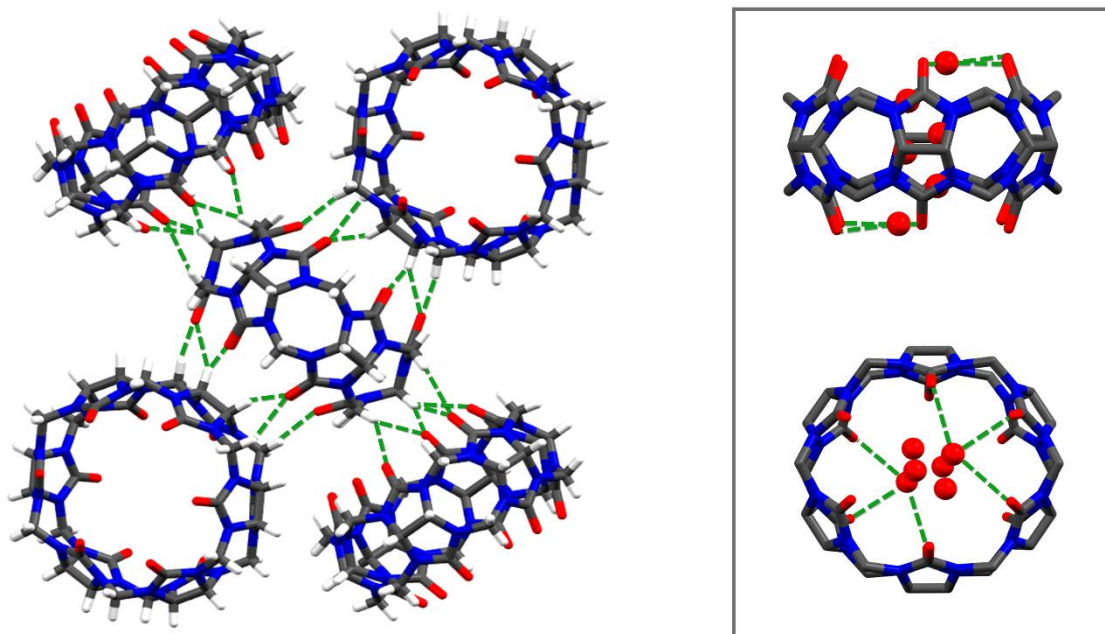


Figure 9. The distorted square-planar unit held together by intermolecular C-H \cdots O hydrogen bonds (left). Green dashed lines indicate the hydrogen bonds between two water molecules and three carbonyl oxygen atoms belonging to each rim (right).

PXRD analysis (Figure 10) was used to confirm the homogeneity of the sample. The powder pattern of the bulk material matches the pattern simulated from the crystal structure of **3a**. Apart from the difference in water content, the structure of **3a** is isoskeletal with respect to the reported structure.¹⁰

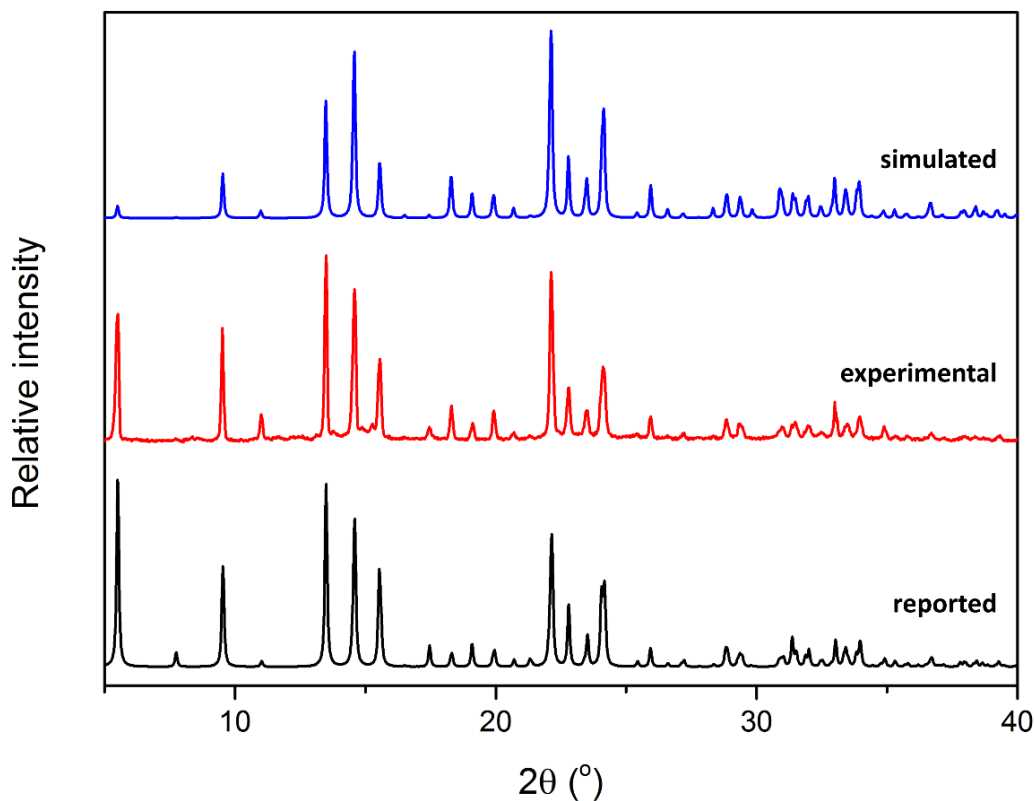


Figure 10. Comparison of the simulated (top), experimental (middle) and reported (bottom) powder diffraction patterns of **3a**. The reported powder pattern is simulated from the literature structure of **3a**.¹⁰

4.3.3. Thermal analysis

The TGA thermogram of **3a** (Figure 11) reveals a 22% weight loss up to 453 K, owing to the loss of the water molecules from the structure. This result is consistent with the expected weight loss of 20%, as determined using the SCXRD structure. The loss of water molecules occurs in two steps. The first 10% weight loss occurs up to 328 K and likely represents the loss of the eight water molecules from the 1D channels. Thereafter, the remaining six water molecules are lost from the macrocyclic cavities. At 623 K, a large weight loss step is observed due to sample decomposition.

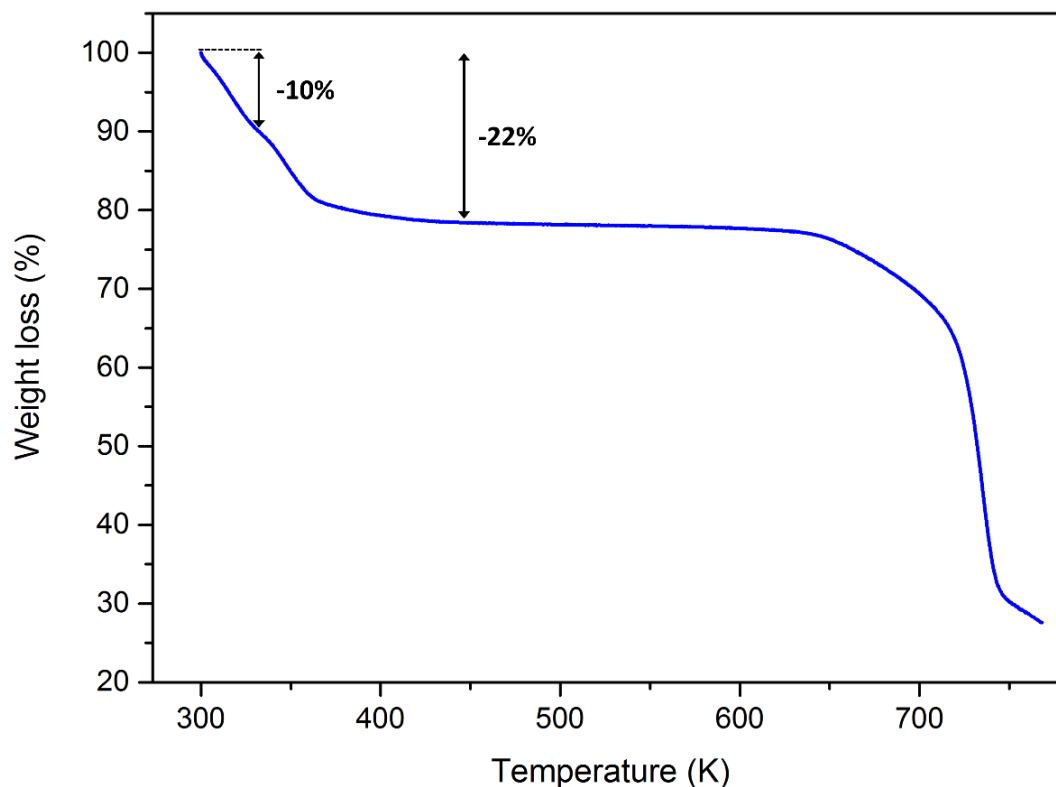


Figure 11. TGA thermogram of **3a** up to 773 K.

4.3.4. Activation of **3a** to produce a porous material

When the water molecules are removed from **3a**, a material with permanent 1D porosity is generated. An activated sample (**3b**) was prepared by heating **3a** at 393 K under dynamic vacuum for 24 h. TGA was used to determine whether the sample was fully activated (Figure 12). However, the thermogram displayed a weight loss of 10% (~6 water molecules) up to 423 K. When the sample is heated for an extended period of time the same profile is obtained. This weight loss is therefore attributed to atmosphere moisture that is absorbed by this porous system (**3b'**) during sample preparation.

In order to confirm that the framework of **3a** survives the activation process, a PXRD analysis was performed. The powder patterns of **3a** and **3b'** are sufficiently similar to indicate that the host packing arrangement is the same for both samples (Figure 12). However, a closer inspection revealed that the powder pattern of **3b'** is shifted to higher 2θ as compared to that of **3a**, signifying that a structural rearrangement to a slightly more close-packed system might have occurred during activation.

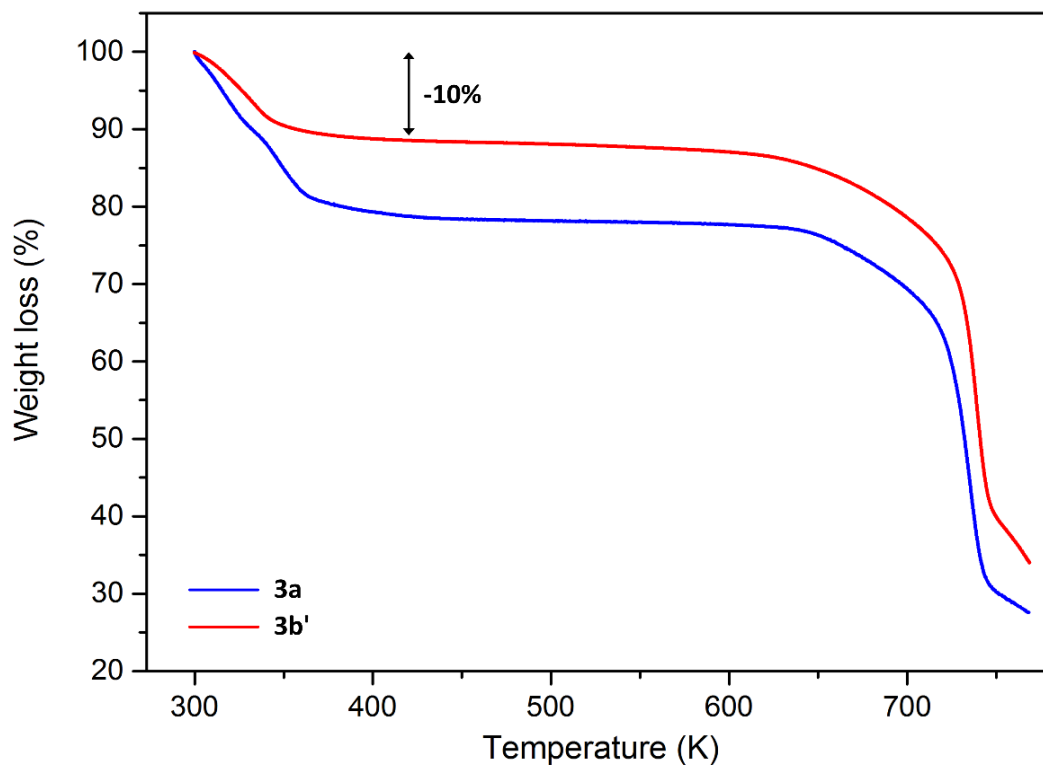


Figure 12. TGA thermograms of **3a** (blue) and **3b'** (red).

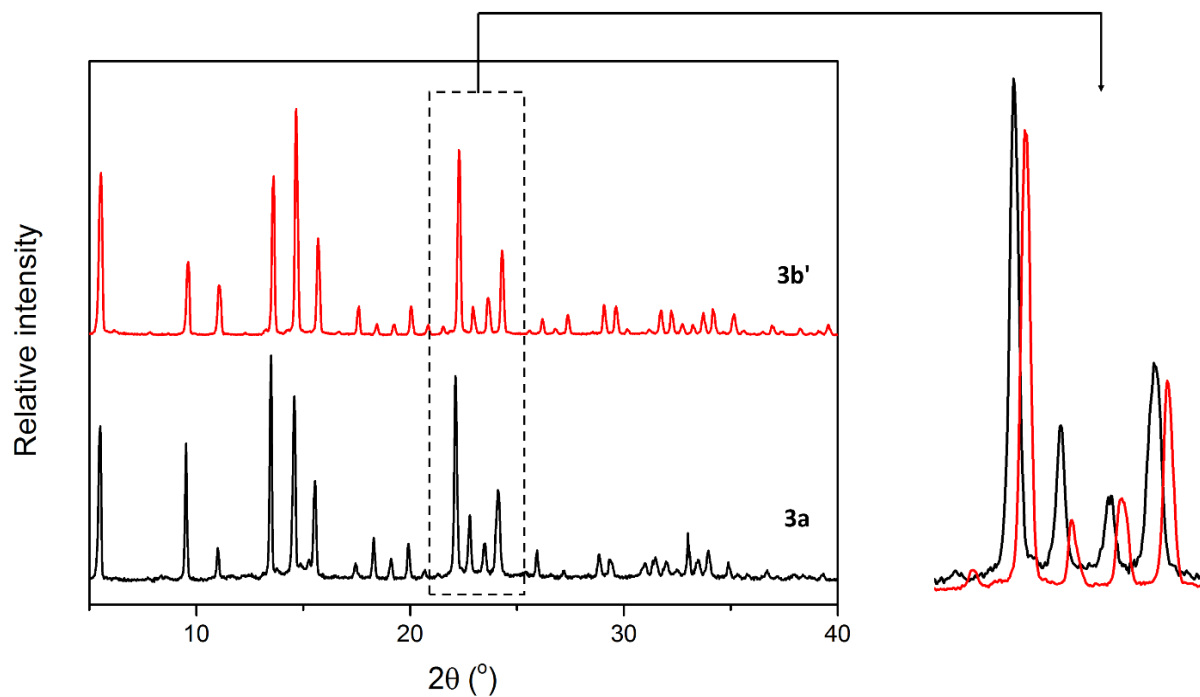


Figure 13. PXRD traces of **3a** (bottom) and **3b'** (top). An expansion of the highlighted section shows that the powder pattern of **3b'** is shifted to higher 2θ .

In order to determine the structure of the partially hydrated form **3b'**, single crystal data of a sample of **3a** that had been activated at 393 K under dynamic vacuum for three days were recorded in a nitrogen atmosphere at 100 K. SCXRD analysis of **3b'** revealed that the structure remains in the trigonal space group $R\bar{3}$. However, the unit cell volume and crystallographic c axis double upon activation (Figure 14). The honeycomb structure survives the activation process, producing 1D channels along the c axis. Closer inspection revealed that a subtle structural change had occurred. The square-planar units of **3b'** are more contracted relative to those of **3a**, resulting in slightly more contracted 1D channels (Figure 14). Consequently, the crystal shrinks by $\sim 3.3\%$ based on the decrease in unit cell volume. The contraction of the square-planar units is discussed in more detail in Section 4.4.1 below. Five water molecules per CB[6] macrocycle could be modelled in the 1D channels. However, the occupancies of the water molecules are very low, likely due to disorder. Unfortunately, the diffuse electron density in the channels made it impossible to accurately determine the disordered positions. SQUEEZE analysis revealed that there are 891 electrons in the solvent accessible volume in the unit cell ($Z = 18$), which corresponds to 4.95 water molecules per macrocycle. The crystals gain $\sim 8.2\%$ in weight owing to the adsorption of moisture, which is similar to the weight gain of 10% indicated by TGA.

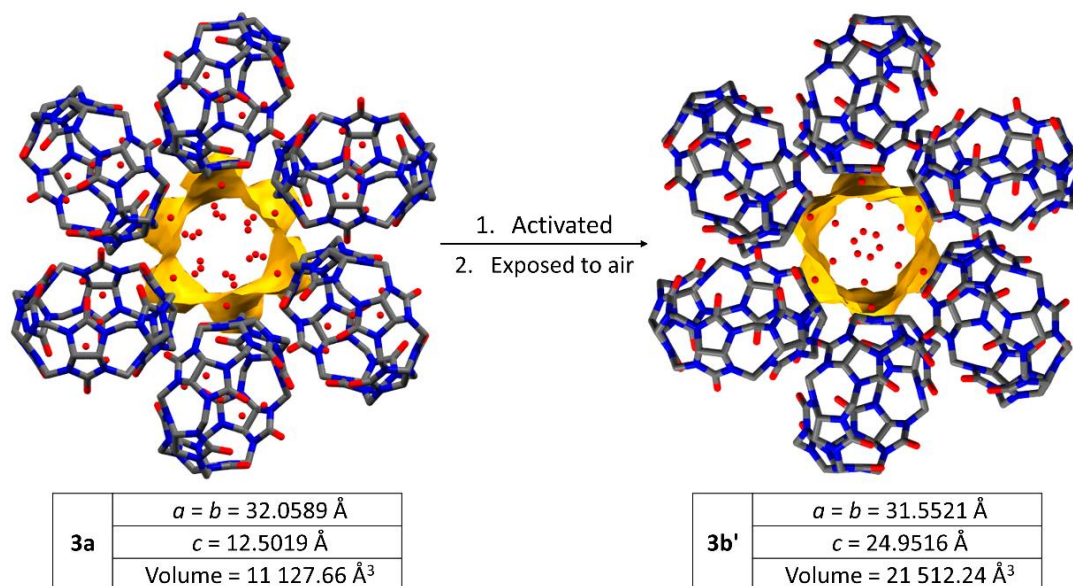


Figure 14. View of a 1D channel of **3a** and **3b'** along the c axis. Selected unit cell parameters of each structure demonstrate the change in unit cell volume and length of the c axis. The slight contraction of the 1D channel walls (yellow) is evident.

4.4. POROUS CB[6]

4.4.1. Structural analysis

Due to the hygroscopicity of **3b**, an environmental gas cell was used to record the SCXRD data of an activated crystal. A suitable single crystal of **3a** was mounted in a gas cell and then activated at 393 K under vacuum (3.25×10^{-5} bar) for five days. SCXRD analysis of **3b** (Figure 15) revealed that the structure is isoskeletal to that of **3b'**, with statistically similar unit cell parameters. As mentioned previously, the square-planar units and channels of **3b** (and **3b'**) are more contracted compared to those of **3a**. The center-to-center distance decreases from 10.15 Å to 10.02 Å and the interplanar angle increases from 75.69° and 76.60° (Figure 15). During activation, water molecules are removed from the intrinsic cavities, including the water molecules that are hydrogen bonded to carbonyl rims of the macrocycles. These carbonyl oxygen atoms become free to act as hydrogen bond acceptors to the methine and methylene groups of a neighboring macrocycle, resulting in closer contact between the molecules. As a result, the dimensions of the channel decrease from 9.40×8.93 Å to 9.24×7.94 Å. The CB[6] molecules rearrange to point their methine and methylene groups towards the channels, creating an inner wall of hydrogen bond donors.

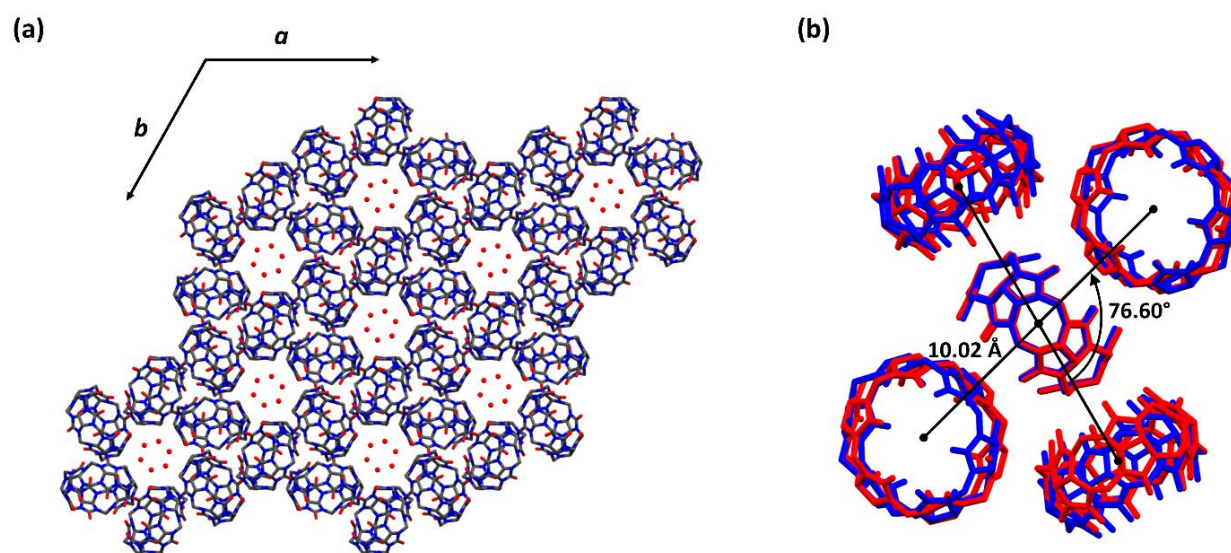


Figure 15. (a) The structure of **3b** as viewed along the *c* axis, displaying the water molecules trapped in the channels. (b) An overlay of the “square planar” unit of **3a** (blue) and **3b** (red) indicating the shift in CB[6] molecules upon activation.

Chapter 4 – Cucurbit[6]uril

Structure elucidation further revealed that the structure is not completely desolvated, even when the crystal is activated for up to 7 days in the gas cell. A water molecule with an occupancy of 0.26 is trapped in the 1D channels. This water molecule is held in place by hydrogen bonds with surrounding methine (3.47 Å, C \cdots O) and methylene groups (3.69 Å, C \cdots O) on the channel walls. SQUEEZE analysis of **3b** showed an electron count of 55 per unit cell for the solvent accessible volume. Since there is one full CB[6] molecule in the ASU ($Z = 18$), the occupancy of the water molecule is 0.30. This result is consistent with the occupancy determined by SCXRD analysis.

4.4.2. Gravimetric sorption analysis

The reported high CO₂ sorption capacity of porous CB[6] up to 1 bar at 298 K^{8a} prompted us to investigate the sorption capacity of **3b** at high CO₂ pressure.

Gravimetric sorption analysis was performed up to a pressure of 20 bar on an activated sample of **3b** at 298 K (Figure 16, red curve). The uptake of CO₂ occurs in one step and can be described as a type I isotherm. At 20 bar, 3.62 mmol g⁻¹ of CO₂ was absorbed, which is equivalent to 3.60 molecules of CO₂ per CB[6] molecule. By 20 bar the isotherm does not reach saturation, suggesting that more CO₂ molecules can be adsorbed. A small hysteric loop is present in the isotherm. This suggests that the CO₂ molecules are retained in the channels of **3b** during desorption, possibly due to strong host-guest interactions. Even after vacuum has been reached, there are still 0.90 molecules of CO₂ (0.74 mmol g⁻¹) present in **3b** per CB[6] molecule. However, these guest molecules can be removed by heating the sample at 333 K overnight in order to regenerate guest-free **3b**.

The gravimetric sorption results of **3b** were compared to the adsorption isotherm reported by Kim *et al.*^{8a} at 298 K. The kinetics of CO₂ adsorption is rather slow for CB[6] at 298 K. In our measurement, the sample was only allowed 45 minutes to equilibrate at each pressure. Consequently, there is quite a large difference between our data and the reported sorption results.^{8a}

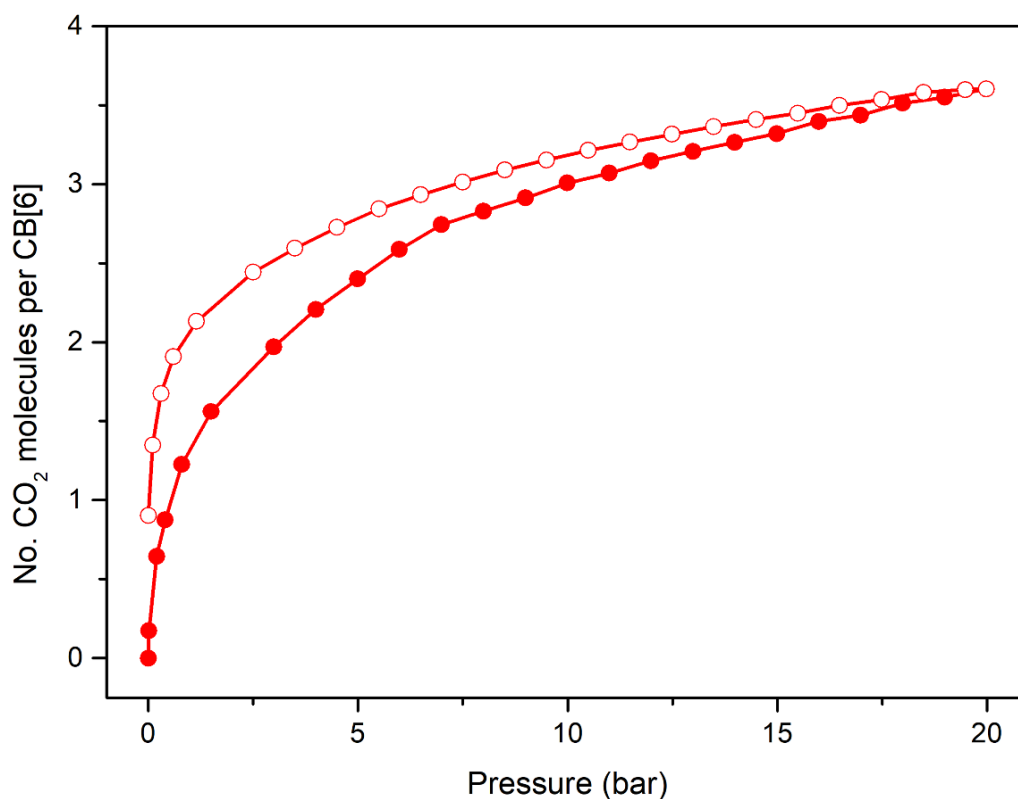


Figure 16. CO₂ sorption isotherms of **3b** at 298 K. Filled circles indicate adsorption and open circles indicate desorption.

4.4.3. Structural analysis of CO₂ inclusion compounds

A single crystal of **3a** was mounted in a gas cell and activated at 373 K under vacuum (3.34×10^{-5} bar) for 5 days to produce **3b**. The CO₂ inclusion compounds formed by CB[6] at 5 bar (**3c**) and 35 bar (**3d**) were studied using SCXRD analysis.

The gas cell was pressurized to 5 bar of CO₂ and the crystal was allowed to equilibrate at this pressure for 8 h before recording the SCXRD data of **3c** at 298 K. The compound remains in the trigonal space group $R\bar{3}$ and has unit cell parameters similar to those of **3a**. Structure elucidation of **3c** revealed that the channels expand in order to accommodate the CO₂ molecules. The ASU contains half a CB[6] molecule and one CO₂ molecule (0.30 occupancy). The CO₂ molecules are located close to the wall in the 1D channels due to C-H \cdots O hydrogen bonds (3.39 Å, C \cdots O) between CO₂ and the methylene groups of CB[6]. The CO₂ molecules also interact with the carbonyl oxygen atoms of CB[6] through dipole-dipole interactions (3.00 Å). Since the structure of **3c** contains large 1D channels, the CO₂ molecule is severely disordered and the disordered positions could not be determined accurately.

Chapter 4 – Cucurbit[6]uril

In addition, a large amount of electron density was still present in the 1D channels and macrocyclic cavities. This electron density is most likely due to CO₂ molecules that could not be modelled.

SCXRD data were also recorded for **3c** at 228 K. At a lower temperature, less disorder is observed and the occupancies of the guest molecules increase. This temperature was chosen since CO₂ is still in the gaseous state at 228 K and 5 bar. If the temperature is further decreased the gas present in the capillary of the gas cell would start to condense and the quality of the single-crystal data would be compromised. At 228 K, two CO₂ molecules (0.61 occupancy each) could be modelled in the intrinsic cavity of each CB[6] macrocycle. These CO₂ molecules adopt a slipped parallel arrangement as a result of a 3.20 Å dipole-dipole interaction. Each CO₂ molecule also forms dipole-dipole interactions with the two carbonyl groups on each rim (3.05-3.18 Å). Even at 228 K the CO₂ molecules are severely disordered, and the total occupancy of the modelled CO₂ molecules only increased to 1.22. No CO₂ molecules could be modelled in the 1D channels due to the large amount of diffuse electron density.

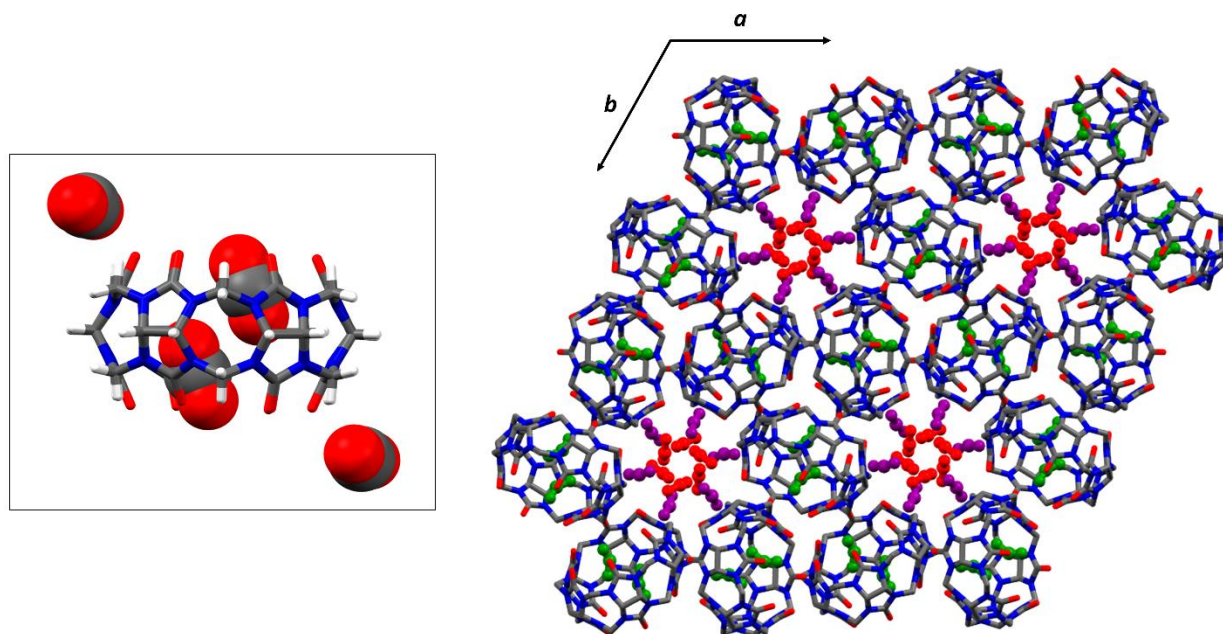


Figure 17. The four CO₂ molecules per CB[6] macrocycle as modelled in **3d** is shown on the left. The structure of the CO₂ inclusion compound viewed along the *c* axis is shown on the right. The CO₂ molecules modelled in the intrinsic cavities and 1D channels in **3d** are shown in green and purple, respectively. The structure reported by Kim *et al.*^{8a} was used to determine the position of the additional CO₂ molecule in the 1D channels, and these are indicated in red.

Chapter 4 – Cucurbit[6]uril

The gas cell was further pressurized to 35 bar of CO₂ and the crystal structure of **3d** was determined at 298 K after equilibration for 8 h. The structure is isostructural to that of **3c** and four CO₂ molecules could be modelled per CB[6] macrocycle in the intrinsic cavities and 1D channels (Figure 17). At 35 bar the occupancies of the CO₂ molecules in the intrinsic cavities and 1D channels increase to 0.78 and 0.60, respectively. Residual electron density in the 1D channels suggests that there is a second CO₂ sorption site. Indeed, Kim *et al.* identified three different CO₂ sorption sites in **3c** using synchrotron radiation.^{8a} Therefore, six CO₂ molecules are present per CB[6] macrocycle (Figure 17). Additionally, two CO₂ molecules are located deeper in the 1D channels and form quadrupole-quadrupole and dipole-dipole interactions with the CO₂ molecules that are located near the channel walls.^{8a} Because of these interactions the CO₂ molecules located deeper in the channels adopt a T-shaped arrangement, while a slipped parallel arrangement is adopted with respect to CO₂ molecules located close to the channel walls.^{8a}

4.4.4. Proposed mechanism for the uptake of CO₂

The structure of **3b** contains intrinsic macrocyclic cavities as well as large extrinsic 1D channels capable of housing up to 6 CO₂ molecules per CB[6] macrocycle.^{8a} However, the slanted square planar arrangement of CB[6] molecules results in partial closure of each CB[6] portal. Despite the limited access to the intrinsic cavities, CO₂ molecules are still able to enter these cavities at a relatively low pressure of 1 bar.^{8a} It is likely that CO₂ molecules travel through the 1D channels before penetrating the intrinsic cavities. The inter-cucurbituril hydrogen bonds would allow cooperative movement of the cucurbituril molecules within the honeycomb network. This dynamic framework would then allow CO₂ to pass from the 1D channels into the intrinsic cavities.

4.5. SUMMARY

The structure of the hydrochloride hydrate of CB[6] is comprised of columnar stacks of CB[6] molecules that are held together by hydrogen bonds with solvent water molecules. As a result, the framework collapses during activation and the CB[6] molecules rearrange to form a honeycomb network comprising interconnected square-planar units. This phase of CB[6] contains large 1D channels that are filled with solvent water molecules. These water

Chapter 4 – Cucurbit[6]uril

molecules can be removed to produce a porous 1D framework (**3b**) with slightly contracted channels.

The CO₂ sorption analysis of **3b** at 298 K revealed that the uptake of CO₂ follows a type I isotherm. The structure thus remains unchanged up to 20 bar of CO₂. *In-situ* SCXRD of **3b** exposed to 5 bar (**3c**) and 35 bar (**3d**) of CO₂ revealed that there are three crystallographically independent sorption sites. Two CO₂ molecules are located in the intrinsic cavity of each CB[6] macrocycle. The structure also contains four CO₂ molecules per CB[6] molecule in the 1D channels. Two of these CO₂ molecules are located near the channel walls, while the remaining two CO₂ molecules are located deeper in the channels.

REFERENCES

1. Behrend, R.; Meyer, E.; Rusche, F. *Justus Liebigs Ann. Chem.* **1905**, 339, 1.
2. Freeman, W. A.; Mock, W. L.; Shih, N.-Y. *J. Am. Chem. Soc.* **1981**, 103, 7367.
3. (a) Kim, J.; Jung, I.-S.; Kim, S.-Y.; Lee, E.; Kang, J.-K.; Sakamoto, S.; Yamaguchi, K.; Kim, K. *J. Am. Chem. Soc.*, **2000**, 122, 540; (b) Day, A.; Arnold, A. P.; Blanch, R. J.; Snushall, B. *J. Org. Chem.*, **2001**, 66, 8094; (c) Day, A. I.; Blanch, R. J.; Arnold, A. P.; Lorenzo, S.; Lewis, G. R.; Dance, I. *Angew. Chem. Int. Ed.*, **2002**, 41, 275.
4. Cheng, X.-J.; Liang, L.-L.; Chen, K.; Ji, N.-N.; Xiao, X.; Zhang, J.-X.; Zhang, Y.-Q.; Xue, S.-F.; Zhu, Q.-J.; Ni, X.-L.; Tao, Z. *Angew. Chem. Int. Ed.* **2013**, 52, 7252.
5. Assaf, K. I.; Nau, W. M. *Chem. Soc. Rev.* **2015**, 44, 394.
6. Barrow, S. J.; Kasera, S.; Rowland, M. J.; De Barrio, J.; Scherman, O. A. *Chem. Rev.* **2015**, 115, 12320.
7. Senler, S.; Li, W.; Tootoonchi, M. H.; Yi, S.; Kaifer, A. E. *Supramol. Chem.* **2014**, 26, 677.
8. (a) Kim, H.; Kim, Y.; Yoon, M.; Lim, S.; Park, S. M.; Seo, G.; Kim, K. *J. Am. Chem. Soc.* **2010**, 132, 12200; (b) Tian, J.; Ma, S.; Thallapally, P. K.; Fowler, D.; McGrail, B. P.; Atwood, J. L. *Chem. Commun.* **2011**, 47, 7626; (c) Wang, P.; Wu, Y.; Z, Y.; Yu, Y.; Zhang, M.; Cao, L. *Chem. Commun.* **2017**, 53, 5503.
9. Pan, S.; Mandal, S.; Chattaraj, P. K. *J. Phys. Chem. B.* **2015**, 119, 10962.
10. Lim, S.; Kim, H.; Selvapalam, N.; Kim, K.-J.; Cho, S. J.; Seo, G.; Kim, K. *Angew. Chem. Int. Ed.* **2008**, 47, 3552.
11. (a) Walker, S.; Kaur, R.; McInnes, F. J.; Wheate, N. J. *Mol. Pharm.* **2010**, 7, 2166; (b) Bardelang, D.; Udachin, K. A.; Leek, D. M.; Margeson, J. C.; Chan, G.; Ratcliffe, C. I.; Ripmeester, J. A. *Cryst. Growth Des.* **2011**, 11, 5598.
12. Bardelang, D.; Udachin, K. A.; Leek, D. M.; Ripmeester, J. A. *CrystEngComm.* **2007**, 9, 973.

Chapter 5

Cucurbit[8]uril

Cucurbit[8]uril (CB[8]) has a cavity volume of 479 \AA^3 , which is almost three times larger than that of CB[6]. Due to its much larger cavity size, CB[8] has the ability to form inclusion complexes with larger guest molecules, such as bulky amphiphilic compounds,¹ macrocycles² and even fullerenes.³ The host-guest chemistry of CB[8] has mostly been studied in solution. Aside from the recently reported gas sorption capacities of a porous phase of CB[8],⁴ very little has been reported regarding the uptake of gases by CB[8].

An investigation of CB[8] as a CO₂ adsorbent is discussed in this chapter. The as-synthesized structure of CB[8] (**4a**) is described and the thermal stability of this compound was investigated. A new phase of CB[8] (**4b**) is generated during activation, but it could not be studied using SCXRD analysis as the sample loses its single crystallinity during the phase transformation. However, volumetric sorption analysis indicated that **4b** is porous. The stepwise CO₂ sorption of **4b** was further investigated using VP-PXRD. Attempts to preserve the single crystallinity of **4a** during the transformation to **4b** are also discussed.

5.1. SYNTHESIS AND CRYSTALLIZATION

CB[8] was synthesized as the only product using a method described by Kim *et al.*⁵ Glycoluril and formaldehyde were partially dissolved in concentrated HCl (37%) and reacted together under solvothermal condition. The reaction mixture was sealed and heated in a Teflon-lined autoclave at 373 K for 12 h. A lower reaction temperature was used as compared to the conventional synthesis of CB[6], thus allowing the formation of CB[8] as the main product.

Two crystallization methods were used during this study. Crude CB[8] was dissolved in a minimum amount of concentrated HCl (37%) and the solution was left to evaporate slowly at room temperature. Distorted octagonal crystals of CB[8] were obtained after a week. CB[8] can also be recrystallized from an aqueous solution of HCl (6-10 M). CB[8] was dissolved in a minimum amount of aqueous HCl (10 M) at 353 K. The solution was then allowed to cool to room temperature and then left for 2 days to allow the formation of crystals. If no crystals formed within this period the solution was diluted with a small amount of distilled water (3-5 ml) and again left for two days. This subsequent dilution step was

repeated until octagonal crystals of CB[8] were obtained. It is important to leave the solution for a few days after each dilution to allow the formation of crystals. If the solution becomes too dilute, no crystals will form. In that case the solution needs to be concentrated by means of water evaporation and the recrystallization process needs to be repeated.

5.2. AS-SYNTHEMIZED CB[8]

5.2.1. Structural analysis

SCXRD analysis of a suitable crystal of as-synthesized CB[8] (**4a**) revealed that the compound crystallizes in the tetragonal space group $I4_1/a$. The structure contains four chloride anions and 23 water molecules per CB[8] molecule (Figure 1a). Ten of these water molecules fill the macrocyclic cavity of CB[8], while the remaining water molecules are located outside the cavity, together with the chloride anions. The hydrogen atoms of the water molecules could not be modelled since it is not possible to accurately determine their positions using SCXRD techniques. Strong to moderate hydrogen bonds (2.44-2.90 Å, O...O) are present between the water molecules in the cavity. Two oxygen atoms belonging to each carbonyl rim form hydrogen bonds (2.93 Å, O...O) with two water molecules in the cavity. Three of the carbonyl oxygen atoms on each rim interact with water molecules and chloride anions located in the extrinsic cavities. The chloride anions also form relatively weak C-H...Cl⁻ ion-dipole interactions (3.70-3.79 Å, C...Cl⁻) with methine groups of the cucurbiturils.

The cavity of each CB[8] molecule is partially closed off by two neighboring molecules due to a series of inter-cucurbituril C-H...O hydrogen bonds. Four carbonyl oxygen atoms on each rim act as hydrogen bond acceptors to methine and methylene groups on an adjacent molecule. Each cucurbituril thus acts as both hydrogen bond donor as well as hydrogen bond acceptor to form a distorted square planar unit⁶ with four surrounding CB[8] macrocycles (Figure 1b). Moderate hydrogen bonds (3.27-3.70 Å, C...O) are responsible for keeping these square planar unit intact. These units are interlocked to produce a network of asymmetrical channels that are connected in three dimensions and filled with water and chloride anions (Figure 1c).

The structure of **4a** is isoskeletal to that of CB[8] reported in the literature.⁴ The reported material was recrystallized from aqueous sulphuric acid and thus contains two sulphate ions and also has a different water content as compared to **4a**. However the overall packing arrangement of the CB[8] molecules is the same in both structures.

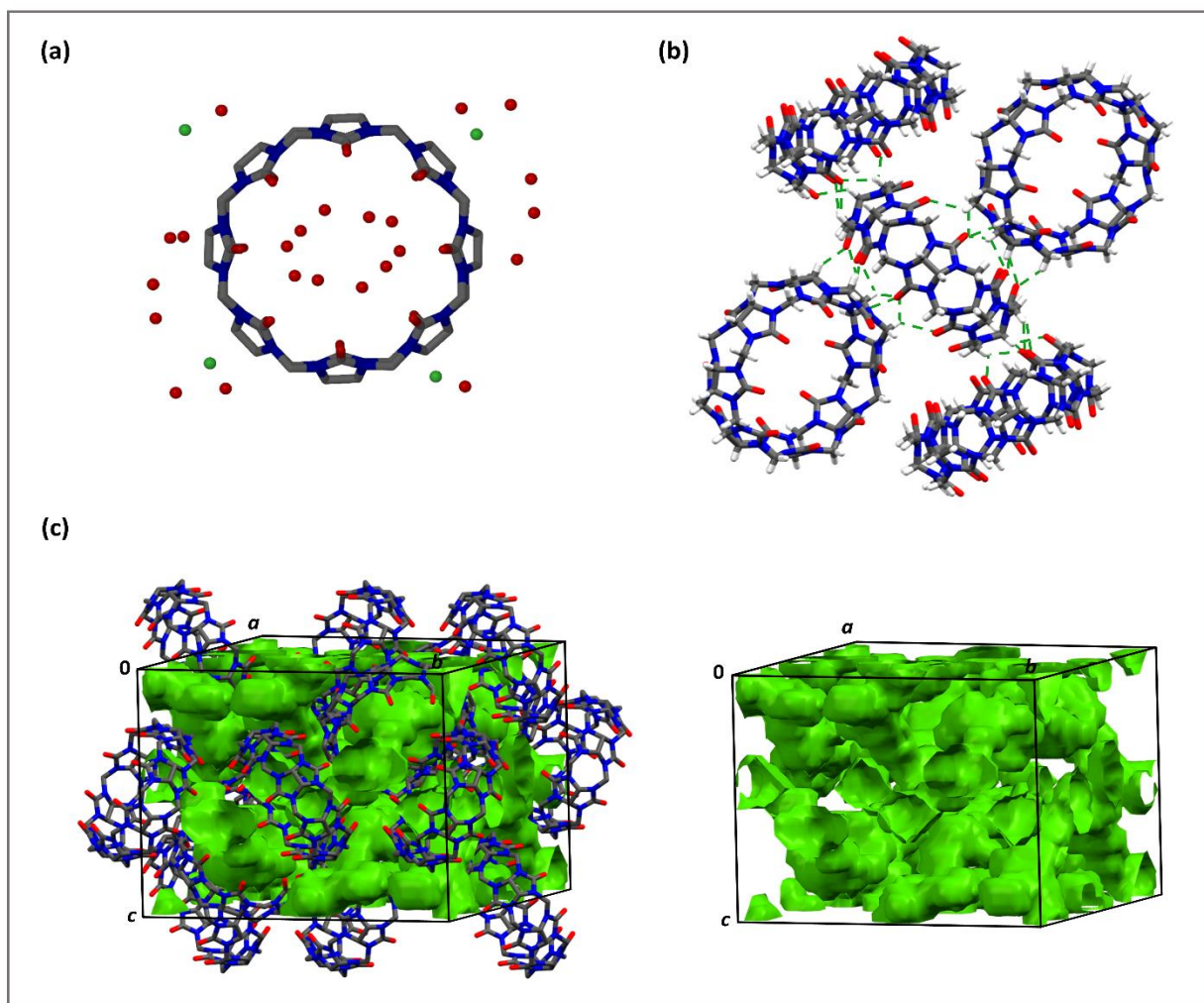


Figure 1. (a) The CB[8] macrocycle with 23 water molecules and four chloride anions as guests. (b) The five-membered distorted square planar unit held together by inter-cucurbituril hydrogen bonds (green dashed lines). (c) The asymmetric channels in the unit cell of **4a** are shown in green. Where applicable, hydrogen atoms have been omitted for clarity.

5.2.2. Thermal analysis

The TGA thermogram of **4a** is shown in Figure 2. A large weight loss step of ~32% is observed in the range of 298 to 473 K due to the loss of water and chloride (*via* HCl) content. The experimental weight loss agrees well with the theoretical weight loss of 30%, as calculated from the crystal structure of **4a**. The guest molecules are present in both the intrinsic and extrinsic cavities of **4a**. Since the cavity of each CB[8] molecule is only partially closed off, the intrinsic and extrinsic cavities are connected. As a result, all the guest molecules are lost in one step, unlike in the case of CB[6] (Chapter 4, Section 4.3.3). After the first step a gradual loss in weight is observed until the sample starts to decompose at 623 K.

Chapter 5 – Cucurbit[8]uril

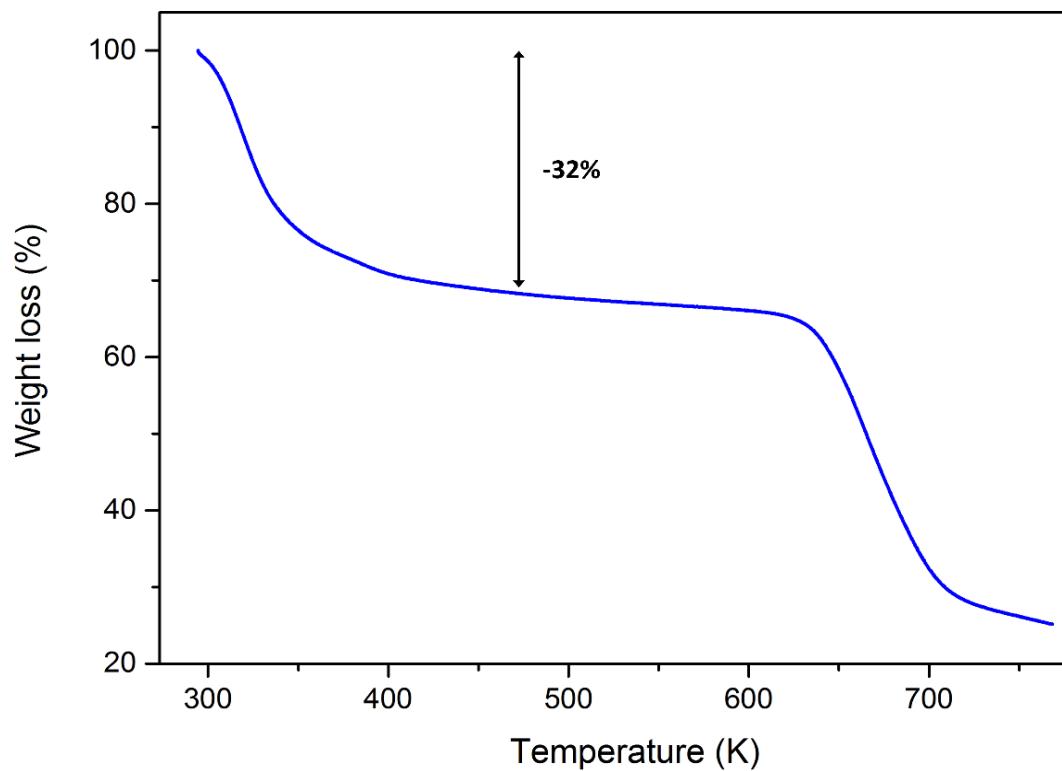


Figure 2. TGA thermogram of **4a** showing a 32% weight loss at 273 K and decomposition at 623 K.

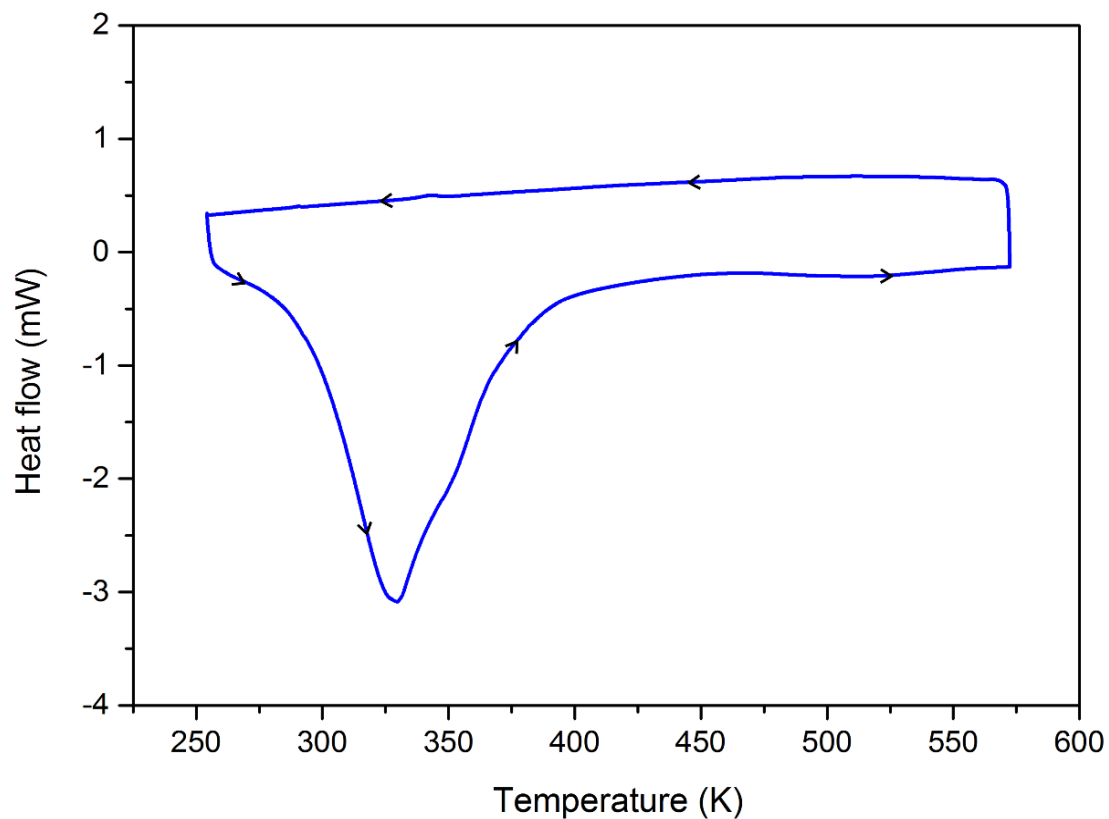


Figure 3. T-DSC profile of **4a** when heated from 253 K to 573 K, followed by cooling to 253 K. The flow of events is indicated by black arrows.

Chapter 5 – Cucurbit[8]uril

As indicated by the TGA thermogram, **4a** rapidly loses its water content once the crystals are removed from the mother liquor. The T-DSC profile of **4a** (Figure 3) displays a large thermal event that starts at 273 K and reaches completion at 448 K. This event represents the loss of guest molecules during a phase transformation to an activated form of CB[8] (**4b**). The energy associated with this phase transformation is 18.7 kJ mol^{-1} . No thermal events occur as the sample is cooled, suggesting that **4b** is preserved.

PXRD was used to monitor the phase transformation that occurs during solvent and anion loss. The powder pattern of a sample of **4a** was recorded at 298 K. Thereafter, the sample was heated to 310 K and the powder pattern was continuously recorded at this temperature in 20 minute intervals to monitor the phase transformation. The change in powder pattern of **4a** over a period of time is shown in Figure 4. After 60 minutes, no further changes in the pattern occur and a partially hydrated phase of **4b** (**4b'**) is formed. The powder pattern of **4b'** is somewhat similar to, but does not exactly match that of the fully activated form **4b** (Figure 4) that was prepared by heating a sample of **4a** at 423 K for 24 h. After the transformation, a polycrystalline powder of **4b'** was obtained and no single crystals were present in the sample.

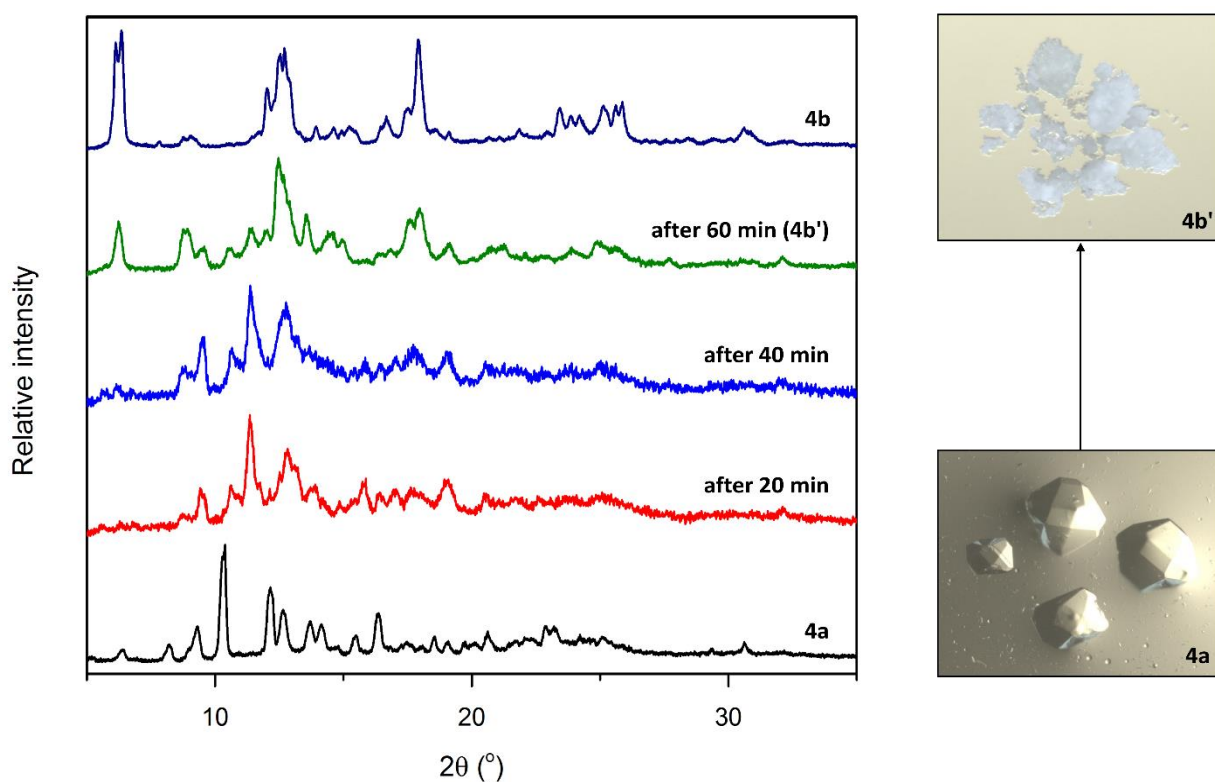


Figure 4. The powder pattern of **4a** changes over time as the sample converts to **4b'**. The PXRD trace **4b'** does not match that of activated **4b** exactly. The single crystals of **4a** and the polycrystalline powder of **4b'** are also shown.

5.3. GUEST-FREE CB[8]

A guest-free sample of **4b** was prepared by heating **4a** at 423 K under dynamic vacuum for 24 h. Due to the loss of single crystallinity, the structure of **4b** could not be determined using SCXRD techniques. Molecular organic solids are known to adopt a close-packed structure in order to maximize favorable intermolecular interactions. It is highly probable that the CB[8] molecules rearrange into a more close-packed structure during the phase transformation from **4a** to **4b**. During this transformation some of the long range crystalline order is lost and a polycrystalline material of **4b** is obtained. The loss in single crystallinity is understandable considering the strain associated with a molecular rearrangement from **4a** with 3D connected channels to the more close-packed structure of **4b**.

TGA of an activated sample of **4b** revealed a step corresponding to 12% weight loss up to 473 K (Figure 5). This step represents the loss of atmospheric water molecules that were absorbed during sample preparation. The hygroscopicity of the sample could be due to the large number of carbonyl oxygen atoms that are available to act as hydrogen bond acceptors. This suggests that the fully activated form is porous to some extent, allowing water molecules to be absorbed into intrinsic and/or extrinsic voids present in the structure. Due to the porosity as well as the strong tendency of cucurbiturils to associate with CO₂ through intermolecular interactions,⁷ **4b** was investigated as a potential CO₂ adsorber.

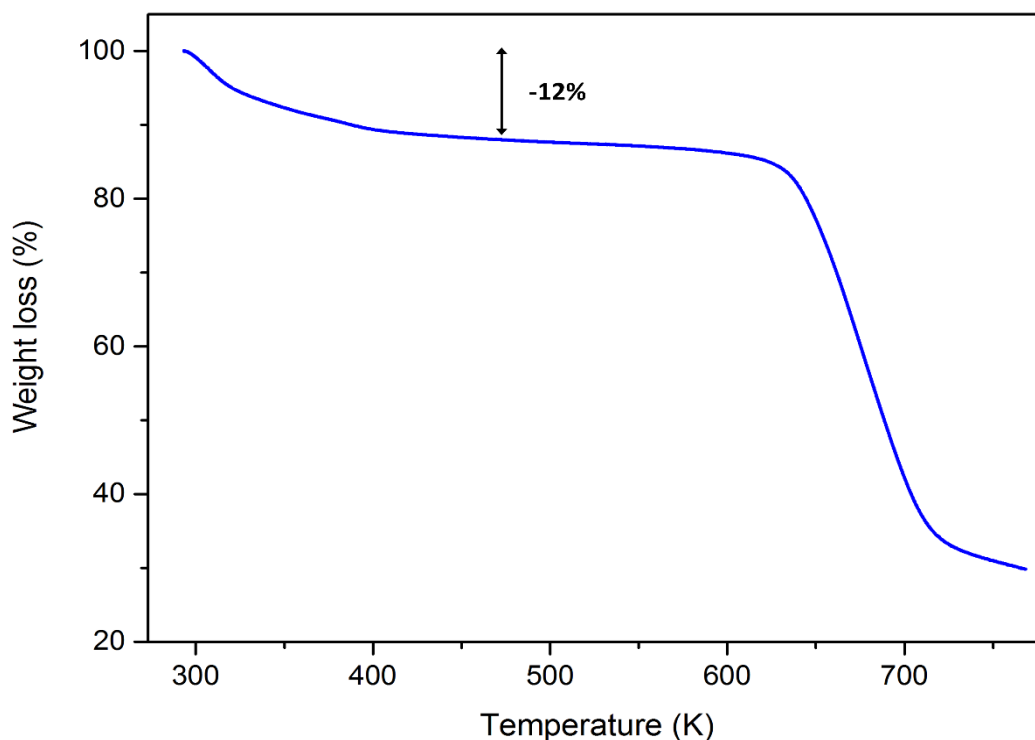


Figure 5. TGA thermogram of an activated sample of **4b** showing a 12% weight loss at 473 K.

5.3.1. Volumetric sorption analysis

The N₂, CH₄ and CO₂ sorption of **4b** were measured volumetrically up to 50 bar at a constant temperature of 298 K (Figure 6). The analyses were carried out using the same sample and the sample was activated *in-situ* prior to each measurement. The analyses were performed in the order of N₂, CH₄ followed by CO₂, in order to prevent any changes in the sample which might affect the gas uptake.

The CO₂ sorption isotherm of **4b** is represented by the red curve in Figure 6. The uptake of CO₂ occurs in two steps. From 0-24 bar, 1.70 mmol g⁻¹ of CO₂ is adsorbed. This is equivalent to approximately two molecules of CO₂ per CB[8] macrocycle. Between 24-30 bar, a transformation to a new phase of CB[8] (**4c**) with a larger CO₂ capacity occurs. This results in a further increase in CO₂ uptake until a total of 3.38 mmol g⁻¹ of CO₂ is adsorbed by 50 bar. At this point there are 4.5 molecules of CO₂ per CB[8] macrocycle. A small step occurs at approximately 2 bar during the desorption of CO₂, indicating that phase **4c** persists up to 2 bar. A large hysteric loop is present in the isotherm, indicating that the sample holds on to the CO₂ molecules strongly by means of intermolecular interactions. By 10 bar, only 18% of the CO₂ that had been absorbed by the sample was released. Even after vacuum had been reached, the concentration of CO₂ does not drop below 0.87 mmol g⁻¹. Thus, 1.16 molecules of CO₂ (per CB[8]) are trapped within the structure. Guest-free **4b** can, however, be regenerated under dynamic vacuum for 4 days, as indicated by VP-PXRD (Section 5.3.2).

The maximum uptakes of CH₄ and N₂ up to 48 bar are 0.45 and 0.47 mmol g⁻¹, respectively. This is equivalent to 0.60 molecules of CH₄ and 0.62 molecules of N₂ per CB[8] macrocycle. The similar and much lower uptake of CH₄ and N₂ as compared to CO₂ could suggest that CH₄ and N₂ are only adsorbed onto the surface of **4b**, while CO₂ is able to penetrate the **4b** framework to occupy intrinsic and extrinsic pockets present in the structure. It is presumed that the lone pair of electrons on the nitrogen atoms of cucurbituril macrocycles as well as the high charge density on their oxygen portals facilitate strong intermolecular interactions with CO₂.⁷ The higher affinity for CO₂ over CH₄ and N₂ is likely due to favorable dipole-quadrupole interactions between CB[8] and CO₂. These interactions would be absent in the case of CH₄ and N₂.

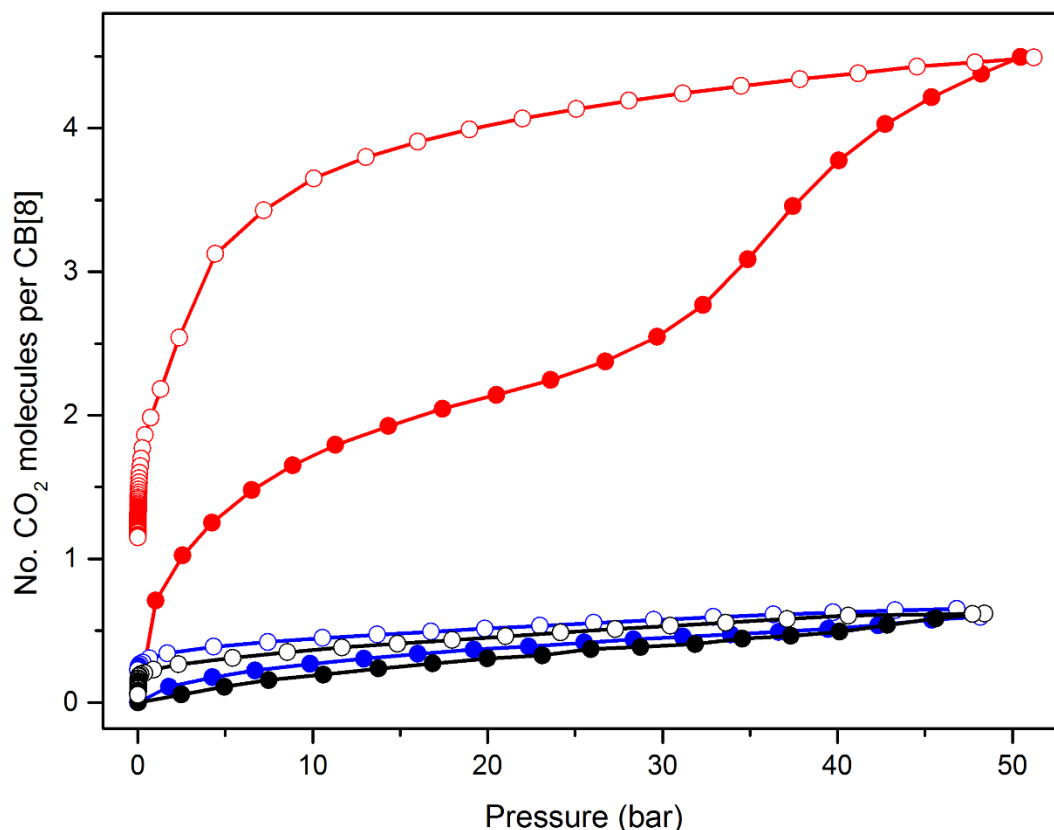


Figure 6. CO₂ (red), CH₄ (blue) and N₂ (black) sorption isotherm of **4b** measured at 298 K. The filled circles represent the adsorption cycle and the open circles represent the desorption cycle.

5.3.2. Phase transformations under gas pressure

The gas-induced phase transformation of **4b** under CO₂ pressure was further investigated using VP-PXRD (Figure 7). A powdered sample of **4a** was packed in a gas cell and the powder pattern was recorded under atmospheric pressure. The sample was then activated at 423 K under high vacuum (2.20×10^{-5} bar) for 24 h to obtain **4b**. The powder pattern of the sample was recorded at 298 K at increasing CO₂ pressure. The sample remains in the same phase over the pressure range 0-25 bar. Subtle changes in the powder pattern become visible between 25-30 bar, as the structural transformation from **4b** to **4c** starts to occur. At 40 bar CO₂ these changes become more apparent. During this transformation, the peaks at 6.20° and 10.80° disappear, and a new peak starts to appear at 11.20° . A noticeable change in the powder pattern occurs between 13.31 - 19.00° . After 40 bar, the powder pattern remains unchanged up to 50 bar, suggesting that the sample remains in the same phase.

The desorption of CO₂ was simulated by decreasing the pressure in the gas cell in increments of 5 bar. The sample was allowed to equilibrate at each pressure for 2 h before recording the powder pattern. The pattern remains unchanged from 50 to 3 bar, indicating that the sample remains in the same phase. At vacuum, the powder pattern closely resembles, but does not exactly overlap, that of the activated form (**4b**). When the sample is kept under vacuum for a longer period (4 days), the powder pattern matches that of the activated form and **4b** is regenerated.

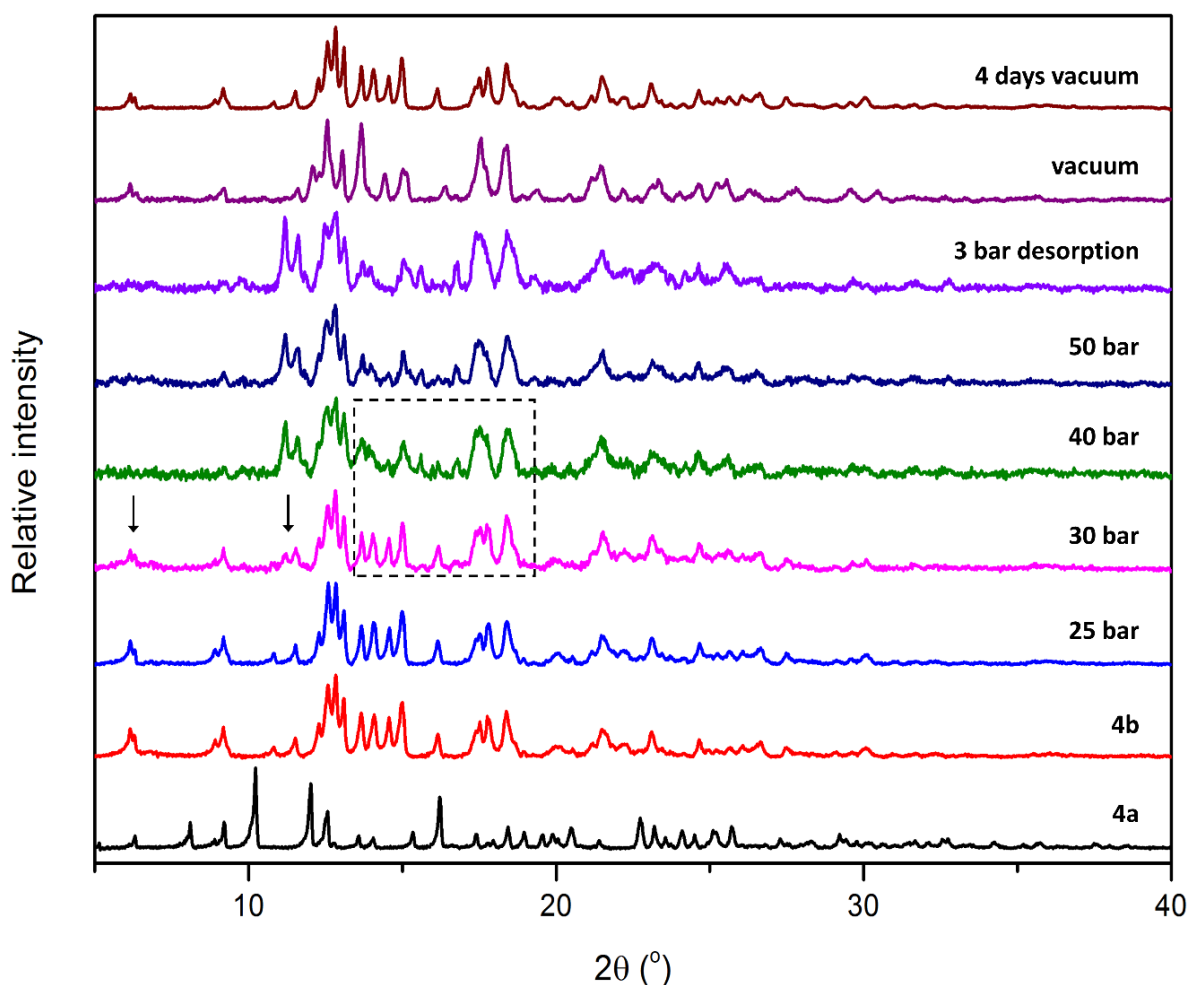


Figure 7. VP-PXRD patterns of **4a**, **4b**, the sample at 25 bar, 30 bar, 40 bar, 50 bar, 3 bar during desorption, vacuum during desorption, and 4 days under dynamic vacuum.

5.3.3. Proposed mechanism for CO₂ uptake and release

As indicated by the sorption results, two CO₂ molecules are adsorbed per CB[8] molecule up to 24 bar, and this increases to 4.5 molecules at 50 bar. Two possible mechanisms are proposed for the uptake of CO₂ molecules by CB[8]:

Chapter 5 – Cucurbit[8]uril

1. The first mechanism (Figure 8a) assumes that the intrinsic cavities of **4b** are more accessible to CO₂ than the extrinsic cavities. Therefore, the CB[8] molecules would have to be arranged in such a way that the CO₂ molecules first fill the intrinsic macrocyclic cavities of CB[8]. At 24 bar, the force exerted by the CO₂ molecules causes an expansion of the framework to the more porous phase **4c**. This allows for further uptake of CO₂ in the extrinsic cavities of the structure.
2. The second mechanism (Figure 8b) assumes that the extrinsic cavities are more accessible than the intrinsic cavities. The CB[8] molecules would have to adopt a square planar arrangement that limits access to the intrinsic macrocyclic cavities. In this case, the CO₂ molecules are first adsorbed into extrinsic spaces present in the framework. At 24 bar, a gas-induced structural expansion causes a rearrangement of CB[8] molecules to produce **4c**. The intrinsic cavities in this phase are accessible and result in further CO₂ uptake.

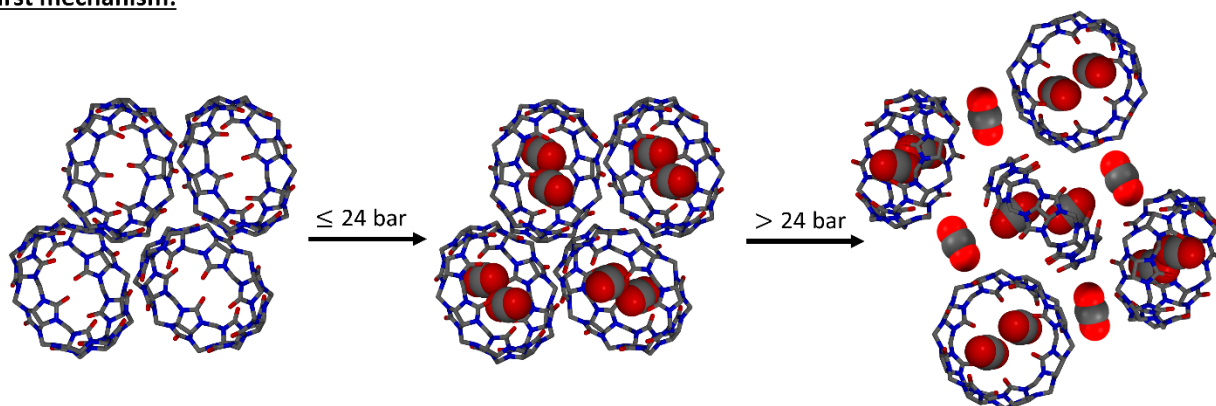
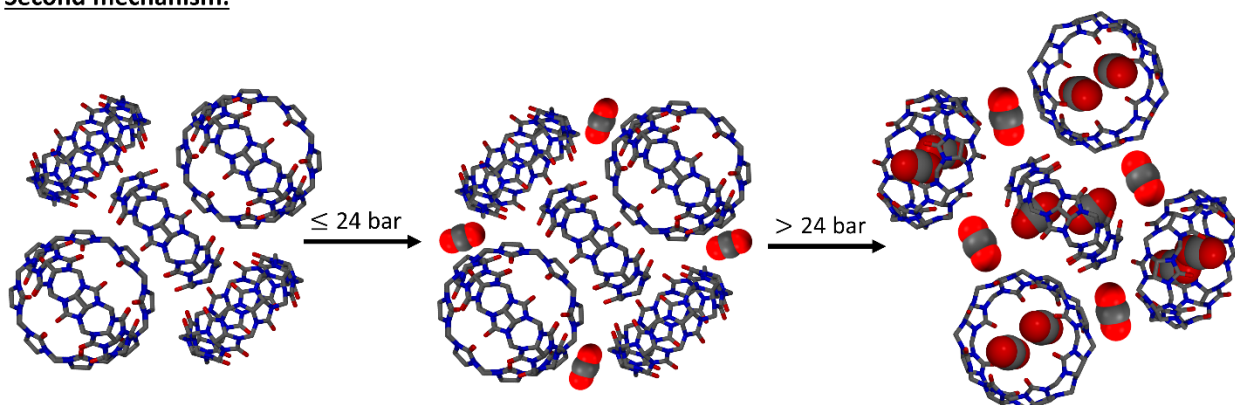
First mechanism:**Second mechanism:**

Figure 8. The two possible mechanisms for the uptake of CO₂ molecules by CB[8]. Proposed structures of **4b** and **4c** are used to illustrate a likely pathway of CO₂ uptake for each mechanism.

Considering that CB[8] has a large macrocyclic cavity (479 \AA^3) and that **4b** only adsorbs two CO_2 molecules per CB[8] at 24 bar, the intrinsic cavities will only be partially filled if the first mechanism applies. At this point, it seems less probable that the pressure exerted by the CO_2 molecules could cause a structural expansion. Therefore, the structure of **4b** most likely contains accessible extrinsic spaces that are first filled with CO_2 molecules and will allow the structure to expand at a higher pressure. For this reason, the uptake of CO_2 most likely occurs by means of the second mechanism. When the CO_2 molecules are released from the extrinsic voids, the structure collapses and **4b** is reproduced. The VP-PXRD and sorption measurements confirm that **4b** undergoes dynamic host-guest transport, despite consisting of rigid building blocks.

5.4. ATTEMPTS TO PRESERVE THE CRYSTALLINITY OF CB[8]

Several approaches were taken in order to preserve the single crystallinity of **4b** during activation, which would allow the structure to be studied using SCXRD techniques.

5.4.1. Supercritical drying

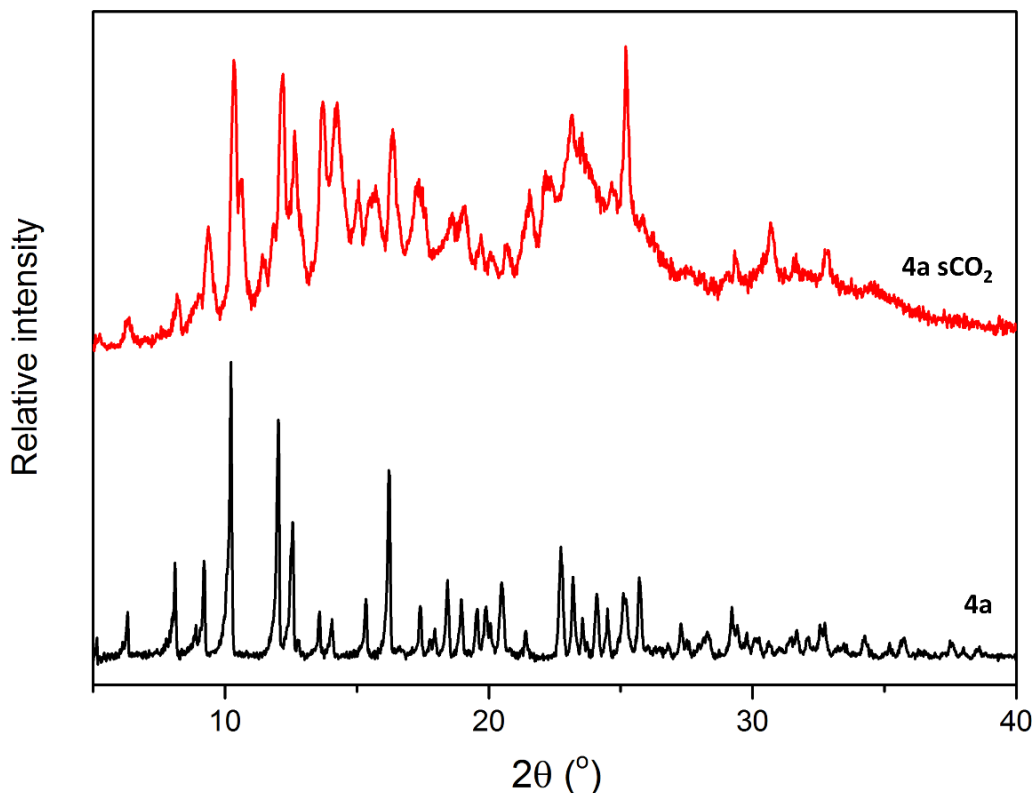


Figure 9. Powder patterns of **4a** (bottom) and a sample of **4a** that had been exposed to sCO_2 conditions overnight (top).

Supercritical CO₂ (sCO₂) conditions have previously been used to activate a solvated sample without the loss of single crystallinity.⁸ During this process, the solvent molecules in the host framework are exchanged with liquid CO₂ that can often be removed without destroying the structural integrity of the sample. This method has mostly been successful for the activation of MOFs and work best for the removal of organic solvents. In this study, supercritical drying was used in an attempt to preserve the crystallinity of **4a**. However, PXRD analysis (Figure 9) of the sample of **4a** that had been exposed to supercritical CO₂ overnight revealed that the phase transformation to **4b** did not occur.

5.4.2. Solvent exchange

Crystals of **4a** were kept in different vials, each containing 1 ml of methanol, ethanol, acetone, ethyl acetate, diethyl ether, dichloromethane (DCM), 1,4-dioxane or acetonitrile (ACN) over a period of a week. The solvents were replaced once a day for a week and the integrity of the single crystals were monitored (Table 1). The crystals immediately started to decompose when placed in 1,4-dioxane, whereas the crystals in ethanol, acetone, ethyl acetate and ACN started to crack and turn brown within a day. The single crystals remained intact in the cases of methanol, diethyl ether and DCM. However, the diffraction data for these crystals were very poor and their structures could not be determined. These crystals lost their single crystallinity when left in their respective solvents for another week.

Table 1. Crystal integrity of single crystals of **4a** during exchange with various solvents after one, two, seven and fourteen days. Crystals remained intact (✓), cracked and turn brown (✓*), started to decompose (×).

Solvent	Day 1	Day 2	Day 7	Day 14
Methanol	✓	✓	✓	×
Ethanol	✓*	×	×	×
Acetone	✓*	×	×	×
Ethyl acetate	✓*	×	×	×
Diethyl ether	✓	✓	✓	×
DCM	✓	✓	✓	×
1,4-dioxane	×	×	×	×
ACN	✓*	×	×	×

5.4.3. Recrystallization of CB[8] with different acids

In order to obtain a more stable phase of CB[8], different acids were used to recrystallize CB[8]. The use of different acids will lead to different anions being present in the crystal structure of CB[8], which may play a role in the stability of the framework.

When CB[8] is recrystallized from aqueous sulphuric acid, the structure is isoskeletal to that obtained from hydrochloric acid (**4a**). These structures only differ in terms of solvent content and the nature of the anion. However, a different phase of CB[8] is obtained when aqueous nitric acid is used as the crystallization solvent.⁹ In this structure, the CB[8] molecules crystallize in the tetragonal space group $I4/mmm$ and contain 1D columns very similar to those of the hydrochloride hydrate of CB[6] (**2a**, Chapter 4). However, this phase loses its crystallinity during activation to produce an amorphous phase of CB[8]. With this in mind, formic acid was used to obtain a new phase of CB[8] during recrystallization.

Slow evaporation of a 12 M formic acid solution of CB[8] yielded small rod-like crystals of CB[8] (**5**) within a week. SCXRD analysis revealed that this new phase of CB[8] crystallizes in the trigonal space group $R\bar{3}$ and has a composition of 22 water molecules and five formate anions per CB[8] macrocycle. Similar to other cucurbituril architectures, the structure of **5** is made up of distorted square planar units of CB[8]. These units are held

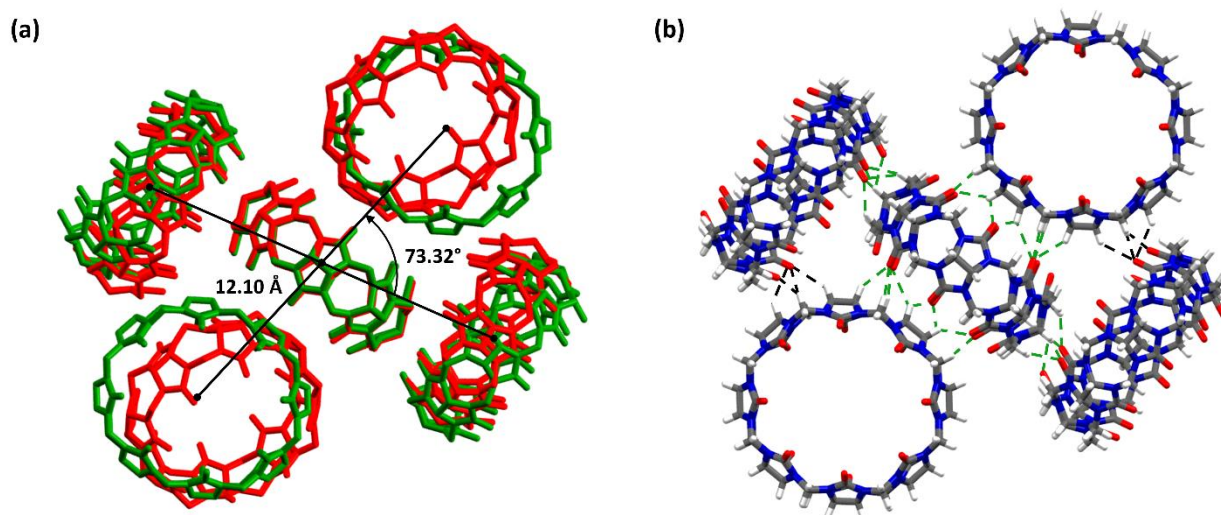


Figure 10. (a) An overlay of the distorted square planar unit formed by **5** (green) and **4a** (red). The centre-to-centre distance (12.10 Å) and inter-planar angle (73.32°) in **5** are also illustrated. (b) The inter-cucurbituril hydrogen bonding present in a square planar unit is indicated as dashed lines. Black dashed lines represent the additional hydrogen bonds between the CB[8] molecules in **5** compared to **4a**.

Chapter 5 – Cucurbit[8]uril

together by inter-cucurbituril hydrogen bonds of 3.25-3.69 Å (C \cdots O). In **5**, two of the carbonyl oxygen atoms on each rim participate in hydrogen bonding to surrounding water molecules. The remaining six carbonyl oxygen atoms on each rim act as hydrogen bond acceptors to methine and methylene groups on adjacent CB[8] molecules (Figure 10). The orientation of the CB[8] molecules in the square planar units of **5** are different as compared to **4a** (Figure 10). The centre-to-centre distance increases from 11.33 Å to 12.10 Å, while the inter-planar angle decreases from 76.51° to 73.32°. As a result, the square planar units of **5** contain additional inter-cucurbituril hydrogen bonds and are more compact than the units in **4a**.

This shift in CB[8] molecules allows the molecules to adopt a hexagonal arrangement, producing a honeycomb network with 1D channels along the *c* axis (Figure 11). The formate anions occupy the 1D channels, while the water molecules are located in the intrinsic cavities of CB[8] as well as in extrinsic pockets between the CB[8] molecules. Interestingly, no water molecules are located in the 1D channels. The structure of **5** closely resembles that of the CB[6] hydrate (**3a**) with 1D channels discussed in Chapter 4. Unfortunately, **5** is not as stable as **3a** and yields an amorphous phase of CB[8] when activated.

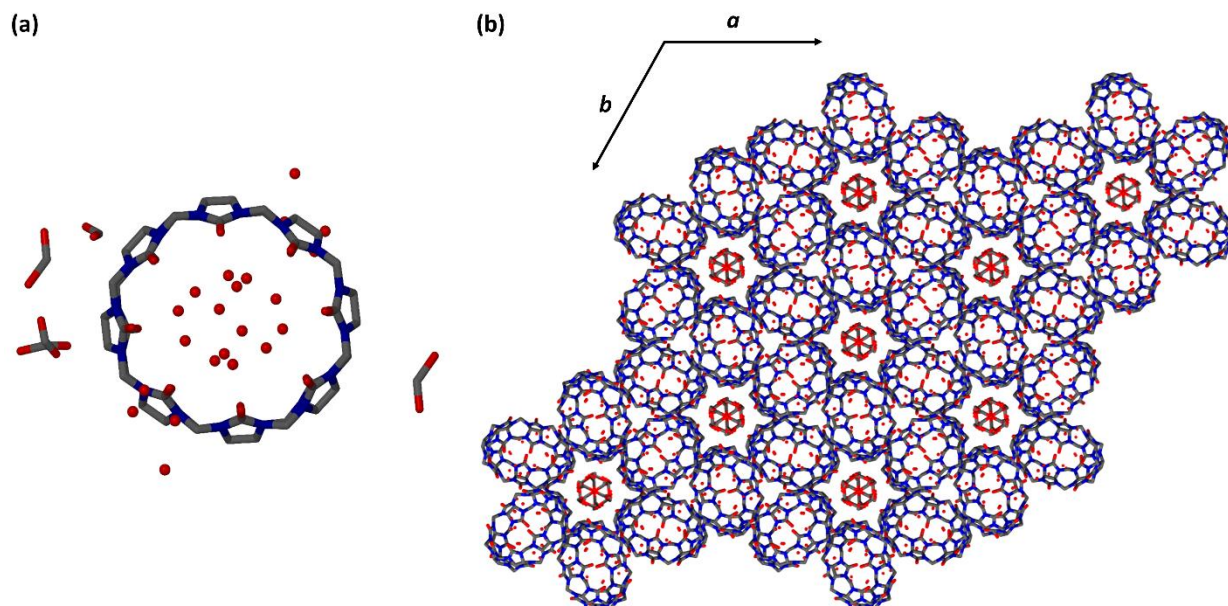


Figure 11. (a) Top view of a CB[8] macrocycle with 22 water molecules and five formate anions. (b) The structure of **5** viewed along the crystallographic *c* axis.

5.4.4. Preserving the anionic species

Since the crystallinity of CB[8] could not be preserved by recrystallizing CB[8] with different acids, crystals were grown in the presence of HCl (3 M) and cadmium salts in another attempt. Cucurbiturils are known to form coordination polymers with various metal ions. Alkali and alkaline earth metals tend to coordinate directly to the oxygen portals of the cucurbiturils,¹⁰ whereas transition metals can coordinate directly¹¹ or associate through a secondary ligand coordination sphere.¹² It was considered that a more stable phase of CB[8] could be produced if the anions were less readily lost during activation. Crystal structures of cucurbit[6]uril and cucurbit[7]uril containing uncoordinated $[\text{CdCl}_4]^{2-}$ anions have been reported.¹³ Therefore, cadmium salts (CdCl_2 and $\text{Cd}(\text{NO}_3)_2$) were used to introduce uncoordinated metal ions into the crystal structure in order to increase the stability of the framework. CB[8] was recrystallized from an aqueous solution of HCl (3 M) containing either CdCl_2 (1 CB[8]: 3 CdCl_2) or $\text{Cd}(\text{NO}_3)_2$ (1 CB[8]: 3 $\text{Cd}(\text{NO}_3)_2$). However, crystals were only obtained in the case of CdCl_2 (**6a**).

SCXRD analysis of **6a** revealed that the complex crystallizes in the tetragonal space group $I4_1/a$ with unit cell parameters similar to those of **4a**. A structural comparison revealed that **4a** and **6a** are isoskeletal and only differ in terms of solvent and anion content. The structure of **6a** contains 20 water molecules per CB[8] molecule (Figure 12). As in the case of **4a**, the cavity of the CB[8] macrocycle is filled with ten water molecules. The remaining ten water molecules are located outside the cavity in the 3D channels. Apart from two chloride anions, the structure also contains one $[\text{CdCl}_6]^{4-}$ anion (full occupancy) and one $[\text{CdCl}_4]^{2-}$ anion (half occupancy) per CB[8] molecule. The cadmium anions are situated between CB[8] molecules in the 3D channels and are arranged such as to produce a 3D diamondoid network (Figure 12). In this network, the $[\text{CdCl}_6]^{4-}$ and $[\text{CdCl}_4]^{2-}$ anions are separated by a minimum Cd1-Cd2 distance of 7.51 Å and a Cd1-Cd2-Cd1 angle of 97.28°.

Figure 13 displays a simplified packing arrangement of the cadmium anions and CB[8] macrocycles along the crystallographic *b* and *c* axes. The arrangement of the cadmium anions between two layers of CB[8] molecules is also displayed. The cadmium anions are arranged between, above and below CB[8] molecules and thereby stabilize the framework. The additional stability provided by the cadmium anions prevents the structure from collapsing during desolvation (discussed below).

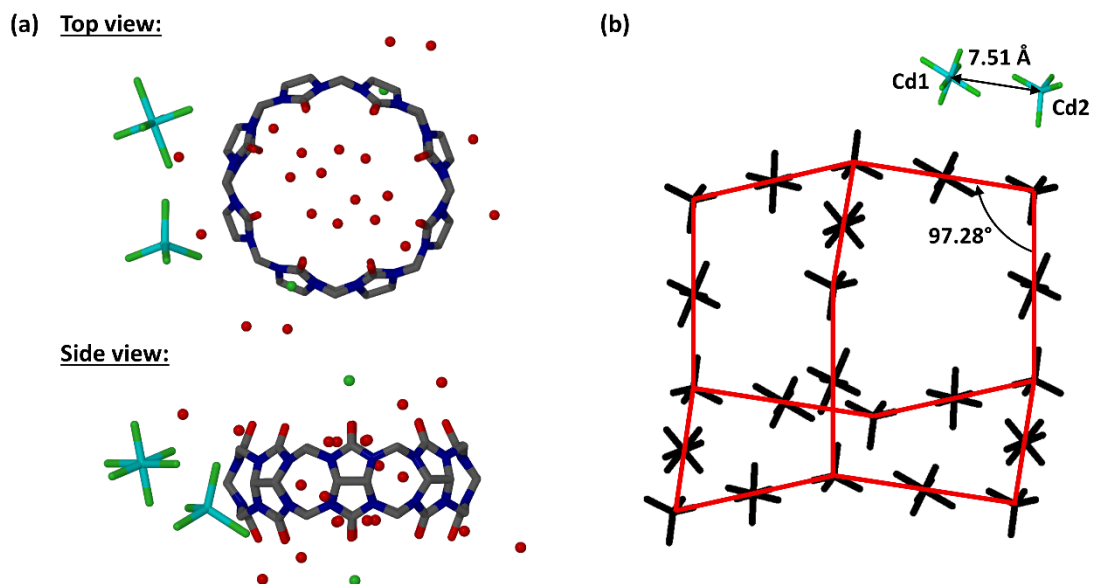


Figure 12. (a) Top and side views of CB[8] and the water molecules, chloride anions and cadmium anions present in the structure of **6a**. (b) The 3D diamondoid network produced by the [CdCl₄]²⁻ and [CdCl₆]⁴⁻ anions.

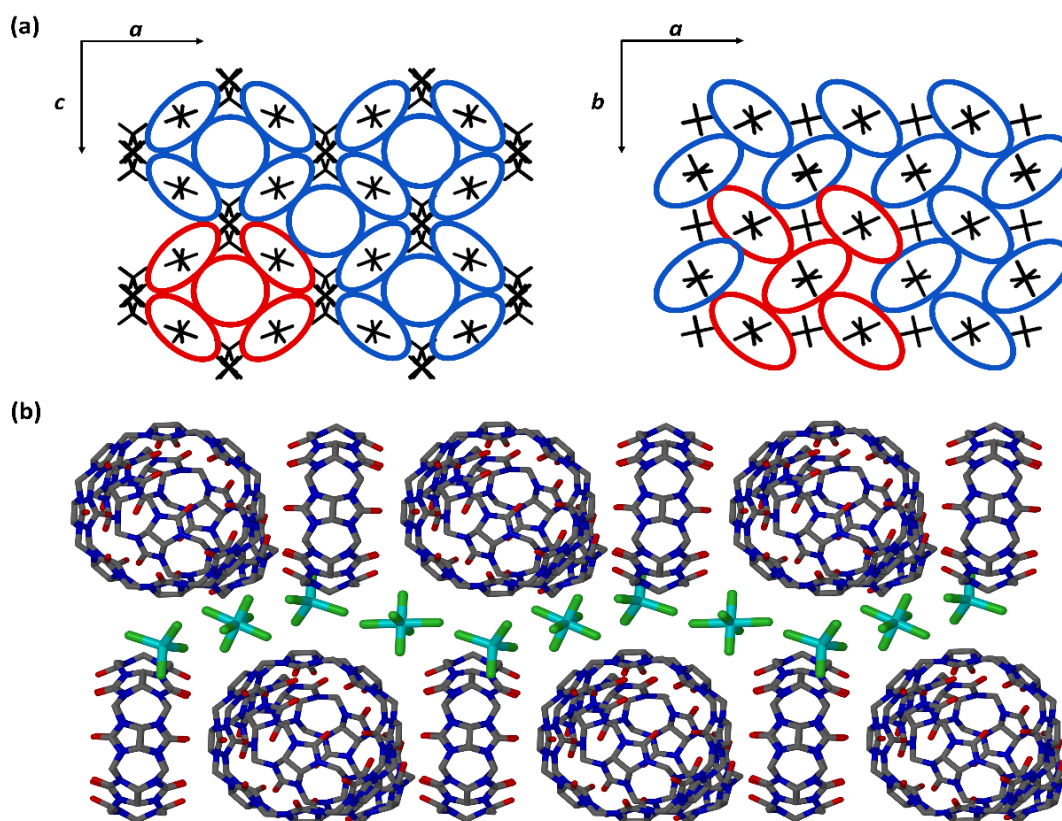


Figure 13. (a) The packing arrangement of **6a** along the *b* (left) and *c* (right) axes. The CB[8] molecules are represented as ovals (side view) and circles (top view). A square-planar unit formed by five CB[8] molecules is highlighted in red. (b) The arrangement of the [CdCl₆]⁴⁻ and [CdCl₄]²⁻ anions between two layers of CB[8]s in **6a**.

Chapter 5 – Cucurbit[8]uril

The TGA thermogram of **6a** is shown in Figure 14. Although the intrinsic and extrinsic cavities of **6a** are connected, a stepwise weight loss is observed. The first step of ~6% occurs in the range of 298-335 K and accounts for the loss of approximately ten water molecules per CB[8] molecule. A second weight loss step of ~7% occurs in the range of 335-473 K and represents the loss of the remaining ten water molecules per CB[8] molecule. Several strong interactions (2.67-2.32 Å) between the cadmium chloride anions and water molecules in the extrinsic cavities could be the reason why these molecules are retained up to a higher temperature. Despite having a similar water content to **4a**, a much lower weight loss is observed up to 473 K (~32% for **4a**). This suggests that the chloride, $[\text{CdCl}_6]^{4-}$ and $[\text{CdCl}_4]^{2-}$ anions are preserved in the case of **6a**. The experimental weight loss is similar to the theoretical weight loss of 16%, when only the water molecules in the structure of **6a** are taken into account. Beyond 473 K a gradual weight loss is observed until the sample starts to decompose at 625 K.

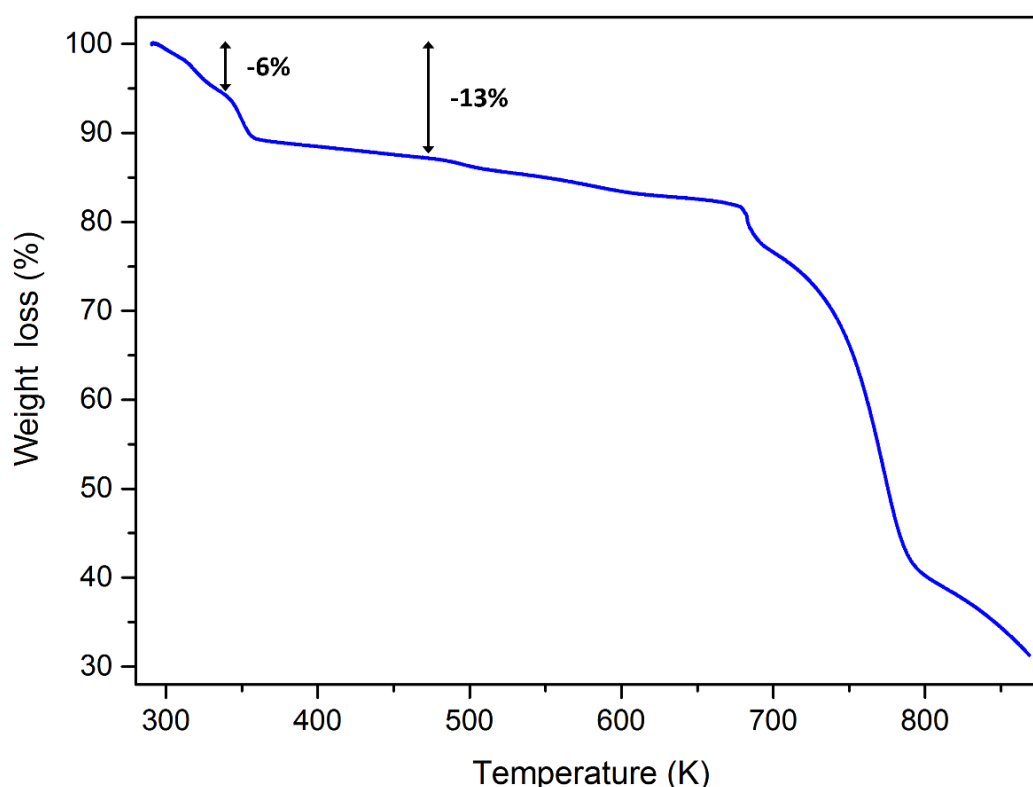


Figure 14. TGA thermogram of **6a** showing a 13% weight loss up to 473 K.

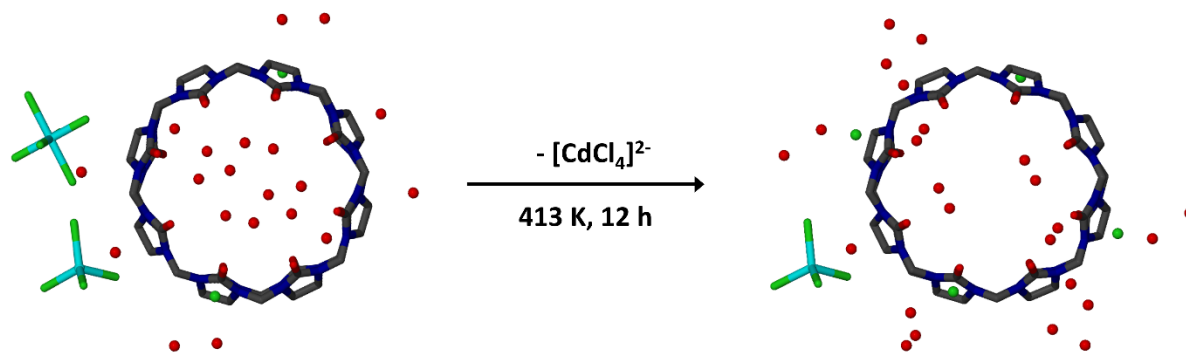


Figure 15. The $[\text{CdCl}_6]^{4-}$ anion present in **6a** (left) is lost as $[\text{CdCl}_4]^{2-}$ during activation at 413 K. The structure of **6b** (right) therefore contains a $[\text{CdCl}_4]^{2-}$ anion and four chloride anions. The structure also contains 23 water molecules, since the single crystal data were recorded in a nitrogen atmosphere.

Unlike **4a**, the crystals of **6a** maintain their single crystallinity during desolvation. Crystals of **6a** were activated at 413 K overnight before collecting the single crystal data in a nitrogen atmosphere at 100 K (**6b**). SCXRD analysis of **6b** revealed that the CB[8] network remains intact and is isoskeletal to **6a** and **4a**. This structure is extremely hygroscopic after activation due to the open 3D channels, and consequently, 26 water molecules could be modelled per CB[8] macrocycle in the structure of **6b**. In agreement with the TGA of **6a**, one $[\text{CdCl}_4]^{2-}$ anion (half occupancy) and four chloride anions are also present per CB[8] (Figure 15). During the activation of **6a**, the number of chloride anions doubles and the $[\text{CdCl}_6]^{4-}$ complex is lost. It is possible that the $[\text{CdCl}_6]^{4-}$ complex converts to $[\text{CdCl}_4]^{2-}$ and two Cl^- anions during activation. It is speculated that $[\text{CdCl}_4]^{2-}$ leaves the structure of **6b** in the form of CdCl_2 and HCl during prolonged heating, while the chloride anions are retained. However, further investigation is required to better understand what happens with the $[\text{CdCl}_6]^{4-}$ complex during activation. The presence of the $[\text{CdCl}_4]^{2-}$ complexes in **6b** prevents the structure from collapsing into the more close-packed structure of **4b** during desolvation. Since the aim was to produce a crystalline phase of **4b**, this structure was not investigated further.

The T-DSC thermogram of **6a** (Figure 16, black curve) displays a large thermal event that starts at 301 K and reaches completion at 445 K. This peak represents the loss of the water molecules from the framework of **6a**. The solvent loss from **6a** occurs at a higher temperature than that of **4a** (Figure 16, red curve). This could suggest that **6a** is more thermally stable than **4a**.

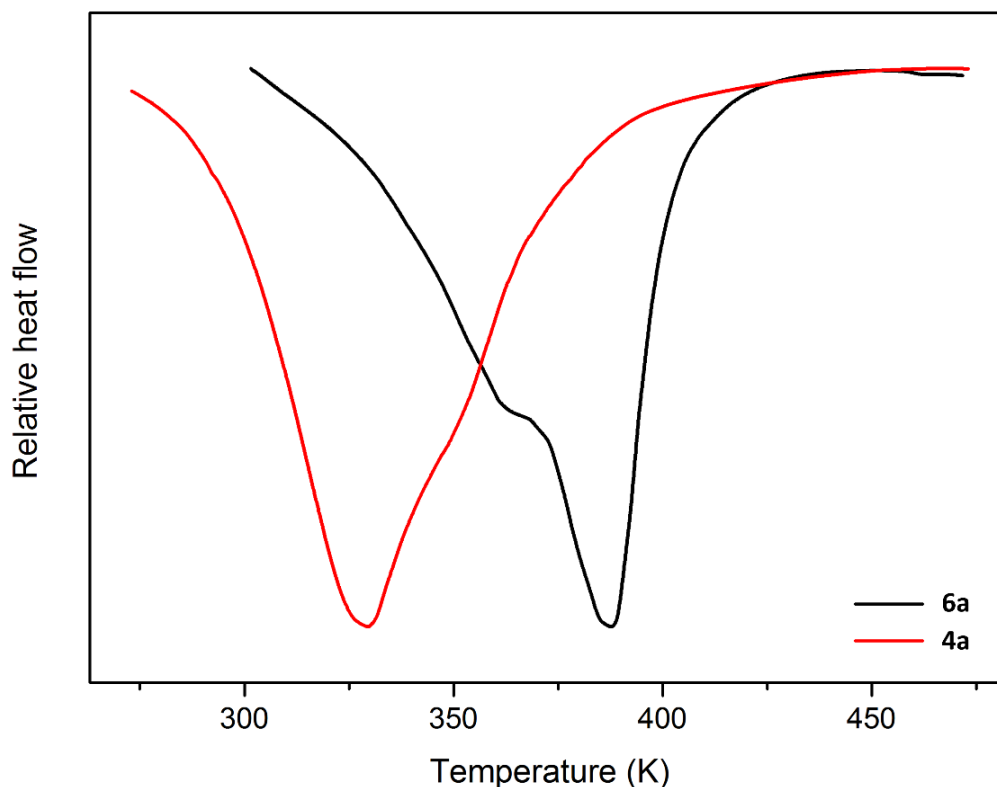


Figure 16. A comparative T-DSC plot of **4a** (red) and **6a** (black).

5.5. SUMMARY

Pure CB[8] was synthesized using a solvothermal method previously reported in the literature. When recrystallized from HCl, hydrochloride hydrate crystals of CB[8] are obtained. The CB[8] molecules arrange in distorted square planar units that are interlocked in three-dimensions to produce a structure with 3D channels filled with water molecules and chloride anions. However, when the water and anion content are removed the structure collapses into a polycrystalline phase of CB[8] (**4b**). Volumetric sorption analysis of N₂ and CH₄ showed limited uptake by **4b**. However, the CO₂ sorption isotherm of **4b** contained two steps. The second step represents a structural transformation to a phase with an increased CO₂ loading capacity. The experimental stoichiometry is 2:1 (CO₂:CB[8]) up to 24 bar and increases to 4.50:1 after the structural transformation up to 50 bar. VP-PXRD was used to confirm that a new form of CB[8] (**4c**) is obtained at high CO₂ pressure. When the sample is kept under vacuum for extended periods of time (four days), the original activated phase (**4b**) is obtained.

Chapter 5 – Cucurbit[8]uril

Since the single crystallinity is lost during activation, the crystal structure of **4b** could not be determined. Several approaches were taken in order to preserve the single crystallinity of **4b**. In most cases the attempts were unsuccessful. However, when crystals are grown in the presence of cadmium chloride a new phase of CB[8] (**6a**) is obtained. This phase contains $[\text{CdCl}_6]^{4-}$ and $[\text{CdCl}_4]^{2-}$ anions in the lattice, which increases the stability of the framework. As a result, the single crystals remained intact during activation.

REFERENCES

1. Liu, S.; Ruspic, C.; Mukhopadhyay, P.; Chakrabarti, S.; Zavalij, P. Y.; Isaacs, L. J. *Am. Chem. Soc.* **2005**, *127*, 15959.
2. Gerasko, O. A.; Samsonenko, D. G.; Fedin, V. P. *Russ. Chem. Rev.* **2002**, *71*, 741.
3. Jiang, G.; Li, G. J. *Photochem. Photobiol.* **2006**, *85*, 223.
4. Wang, P.; Wu, Y.; Zhao, Y.; Zhang, M.; Cao, L. *Chem. Commun.* **2017**, *53*, 5503.
5. Kim, J.; Jung, I.-S.; Kim, S.-Y.; Lee, E.; Kang, J.-K.; Sakamoto, S.; Yamaguchi, K.; Kim, K. *J. Am. Chem. Soc.*, **2000**, *122*, 540.
6. Lim, S.; Kim, H.; Selvapalam, N.; Kim, K.-J.; Cho, S. J.; Seo, G.; Kim, K. *Angew. Chem. Int. Ed.* **2008**, *47*, 3552.
7. Tian, J.; Shengqian, M.; Thallapally, P. K.; Fowler, D.; McGrail, B. P.; Atwood, J. L. *Chem. Commun.* **2011**, *47*, 7626.
8. Kim, T. K.; Suh, M. P. *Chem. Commun.* **2011**, *47*, 4258.
9. Bardelang, D.; Udachin, K. A.; Leek, D. M.; Ripmeester, J. A. *CrystEngComm.* **2007**, *9*, 973.
10. (a) Feng, X.; Chen, K.; Zhang, Y.-Q.; Xue, S.-F.; Zhu, Q.-J.; Tao, Z.; Day, A. I. *CrystEngComm*, **2011**, *13*, 5049; (b) Danylyuk, O.; Fedin, V. P. *Cryst. Growth Des.* **2012**, *12*, 550; (c) Qiu, S.-C.; Li, Q.; Zhang, Y.-Q.; Xiao, X.; Tao, Z.; Zhu, Q.-J.; Zhang, Z.-Q. *Chin. J. Inorg. Chem.* **2016**, *32*, 1303.
11. (a) Liang, L.-L.; Chen, K.; Ji, N.-N.; Cheng, X.-J.; Zhao, Y.; Xiao, X.; Zhang, Y.-Q.; Zhu, Q.-J.; Xue, S.-F.; Tao, Z. *CrystEngComm.* **2013**, *15*, 2416; (b) Shan, C.-Y.; Zhao, W.-X.; Tao, Z.; Zhang, Y.-Q. *Inorg. Chem. Commun.* **2016**, *71*, 109.
12. (a) Roh, S.-G.; Park, K.-M.; Park, G.-J.; Sakamoto, S.; Yamaguchi, K.; Kim, K. *Angew. Chem., Int. Ed.* **1999**, *38*, 638; (b) Park, K.-M.; Whang, D.; Lee, E.; Heo, J.; Kim, K. *Chem. –Eur. J.* **2002**, *8*, 498; (c) Liu, J.-X.; Hu, Y.-F.; Lin, R.-L.; Sun, W.-Q.; Liu, X.-H.; Yao, W. R. *J. Coord. Chem.* **2010**, *63*, 1369.
13. (a) Yang, B.; Xiao, X.; Zhang, Y.-Q.; Zhu, Q.-J.; Xue, S.-F.; Tao, Z.; Wei, G. *RSC Advances.* **2014**, *4*, 44359; (b) Liang, L.-L.; Ni, X.-L.; Zhao, Y.; Chen, K.; Xiao, X.; Zhang, Y.-Q.; Redshaw, C.; Zhu, Q.-J.; Xue, S.-F.; Tao, Z. *Inorg. Chem.* **2013**, *52*, 1909.

Chapter 6

Concluding remarks

Guest inclusion in solid-state host compounds is a fundamental aspect of supramolecular chemistry, with numerous potential applications. In this dissertation, the well-known organic hosts TBC4, CB[6] and CB[8] were investigated as CO₂ adsorbents. The non-covalent interactions and porosity displayed by the host frameworks were studied in order to gain a better understanding of the underlying factors involved in the uptake of CO₂ molecules.

The study started with the investigation of the LDP of TBC4 (**1a₀**) (Figure 1), which is a known CO₂ adsorbent. The single crystals of **1a₀** were grown by sublimation at 533 K. Structural analysis of **1a₀** showed that the overall framework is held together by van der Waals interactions between the TBC4 molecules. Strong hydrogen bonding between the hydroxyl groups in each TBC4 molecule causes the molecules to adopt a cone conformation. As a result, the bowl of each molecule contains a hydrophobic cavity with a calculated volume of approximately 275 Å³. Since these cavities are isolated, the porosity of **1a₀** can be described as zero-dimensional (0D). Volumetric sorption analysis indicated that this host adsorbs CO₂ in a stepwise fashion. Below 22 bar of CO₂, these cavities are filled to produce a CO₂ inclusion compound (**1a·CO₂**) with an ideal stoichiometry of 1:1 (CO₂:TBC4). Above 22 bar, a structural transformation to a phase (**1c·CO₂**) with additional extrinsic cavities occurs. This increases the guest loading capacity of the host to form a CO₂ inclusion compound with an ideal stoichiometry of 2:1 (CO₂:TBC4). This phase is preserved during desorption to produce a new apohost phase of TBC4 (**1c₀**) when all the CO₂ molecules have been removed. Although the single crystal structure of **1c₀** could not be determined, it is likely that the structure is isoskeletal to that of **1c·CO₂** and a possible structure of **1c₀** with virtual porosity was generated. This structure contains large pear-shaped voids, each with a calculated volume of 162 Å³. CO₂ uptake by **1a₀** is interesting since CO₂ molecules are capable of moving through the host framework to fill the isolated cavities. This would require cooperative movement of the TBC4 molecules. Computational studies¹ suggested that the rotation of the tert-butyl groups plays a vital role in enabling lateral movement of the bilayers, thereby allowing guests such as CO₂ to move through the framework.

Chapter 6 – Concluding remarks

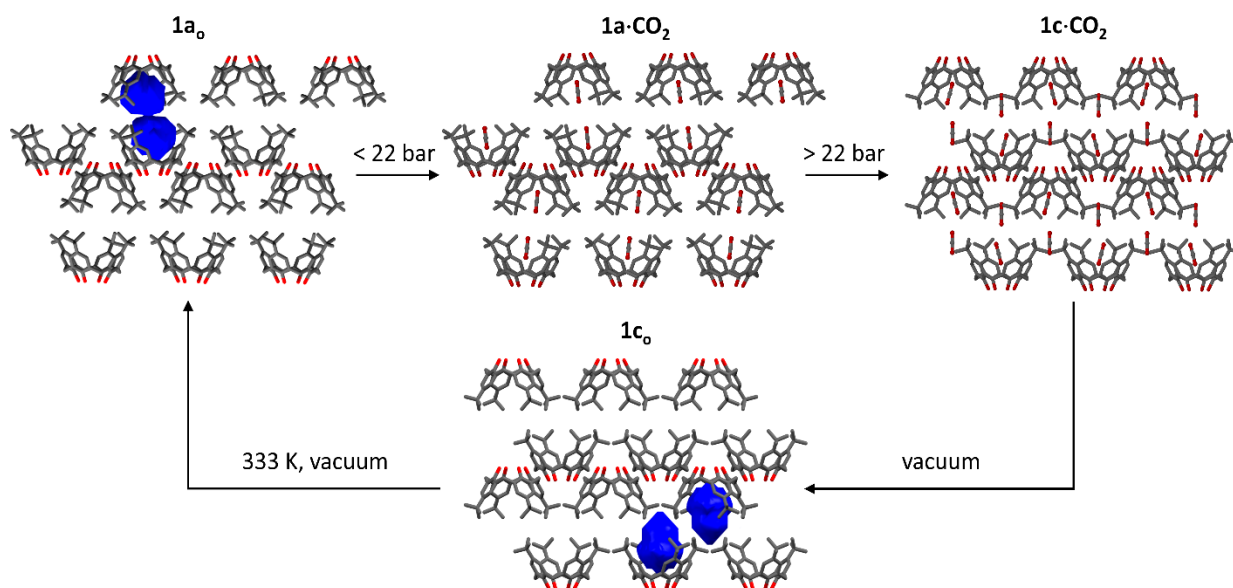


Figure 1. Representation of the crystal structures of the LDP of TBC4 (**1a₀**), the CO₂ inclusion compound at 4.5 bar (**1a·CO₂**), the CO₂ inclusion compound at 30 bar (**1c·CO₂**) and the probable structure of the new apohost phase (**1c₀**).

The study of TBC4 was extended by also investigating the behavior of the HDP of TBC4 (**1b₀**) under CO₂ pressure (Figure 2). Structural analysis of **1b₀** revealed that the TBC4 molecules form interdigitated dimers that arrange in a close-packed fashion in all three dimensions and therefore lack intrinsic and extrinsic cavities. CO₂ sorption analysis of **1b₀** up to 50 bar indicated that no CO₂ is adsorbed while the sample remains in the HDP. However, a gas-induced transformation from **1b₀** to the porous phase **1c·CO₂** rapidly occurs at 35 bar, which allows the uptake of CO₂ molecules. Again, this phase is preserved during desorption to produce **1c₀** when vacuum is reached. As a result of the large molecular reorganization to **1c·CO₂**, the single crystallinity is lost and the SCXRD data of **1c₀** under 40 bar CO₂ were unusable. However, the unit cell parameters are reminiscent to those of **1c·CO₂** at 298 K. This demonstrates how a close-packed non-porous structure can be conditioned to produce a porous material under high pressure. Similar to **1a₀**, it is likely that the rotation of the *tert*-butyl group plays a role in the cooperative movement of the AB layer in **1b₀**. This could momentarily produce pathways for CO₂ that would induce a structural expansion to **1c·CO₂** under relatively high CO₂ pressure.

Chapter 6 – Concluding remarks

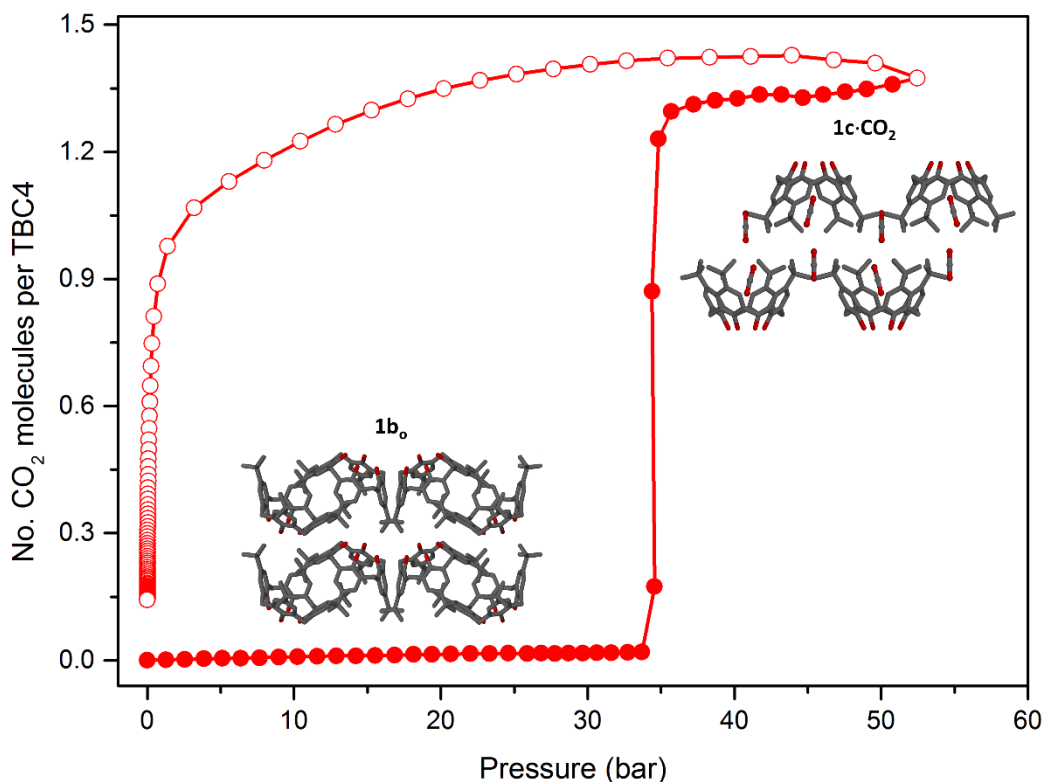


Figure 2. The CO₂ sorption isotherm of **1b₀** at 298 K showing the gas-induced structural transformation from **1b₀** to **1c-CO₂** that occurs beyond 35 bar.

Next the well-known organic host, CB[6], was investigated as a host for CO₂. CB[6] has been shown² to have a large affinity for CO₂ and was studied in order to gain a better understanding of the host-guest interactions. Hydrochloride hydrate crystals of CB[6] (**2a**) can easily be grown from a concentrated solution of HCl. Structural analysis of **2a** revealed that the material has a very high water content (34 H₂O molecules per CB[6]) and relies on hydrogen bonds with surrounding water molecules to keep the 1D columnar stacks of CB[6] molecules intact. As a result, the framework starts to disintegrate when solvent loss occurs and a short-lived intermediate phase (**2a'**) is produced before converting to **3a**. In **3a**, the CB[6] molecules arrange in interconnected square-planar units to produce a honeycomb network with 1D channels that are filled with water molecules. When the water molecules are removed, the framework contracts slightly to produce **3b** with permanent 1D porosity. CO₂ sorption analysis of **3b** at 298 K revealed that the uptake of CO₂ follows a type I isotherm. The very slow kinetics of CO₂ sorption suggests that several host-guest interactions are occurring during guest uptake. Unlike the case of TBC4, the framework appears to be rigid and does not show signs of a gas-induced structural transformation. The CO₂ inclusion compounds were studied *in-situ* under 5 bar and 35 bar CO₂. Under CO₂ pressure, the

Chapter 6 – Concluding remarks

framework of **3b** expands to produce a structure that is isoskeletal to **3a**. There are three crystallographically independent sorption sites that allow the accommodation of six CO₂ molecules per CB[6] (Figure 3).² However, only four CO₂ molecules could be modelled per CB[6] macrocycle in this study. Two CO₂ molecules are located in the intrinsic cavity of each CB[6] macrocycle, while the remaining four CO₂ molecules are located in the 1D channels. Several guest-guest and host-guest interactions are present in the inclusion compounds and could be the reason for the high CO₂ affinity of this host. The methine and methylene groups of the CB[6] molecules point towards the surfaces of the channel walls and act as hydrogen bond donors to CO₂ molecules situated in the 1D channels. The CO₂ molecules can easily move through the 1D channels in the structure to occupy the various sorption sites. However, the macrocyclic cavities are closed off and cooperative movement of the cucurbiturils molecules is required to allow CO₂ to enter these voids. The dynamic nature of this host is facilitated by the series of inter-cucurbituril hydrogen bonds.

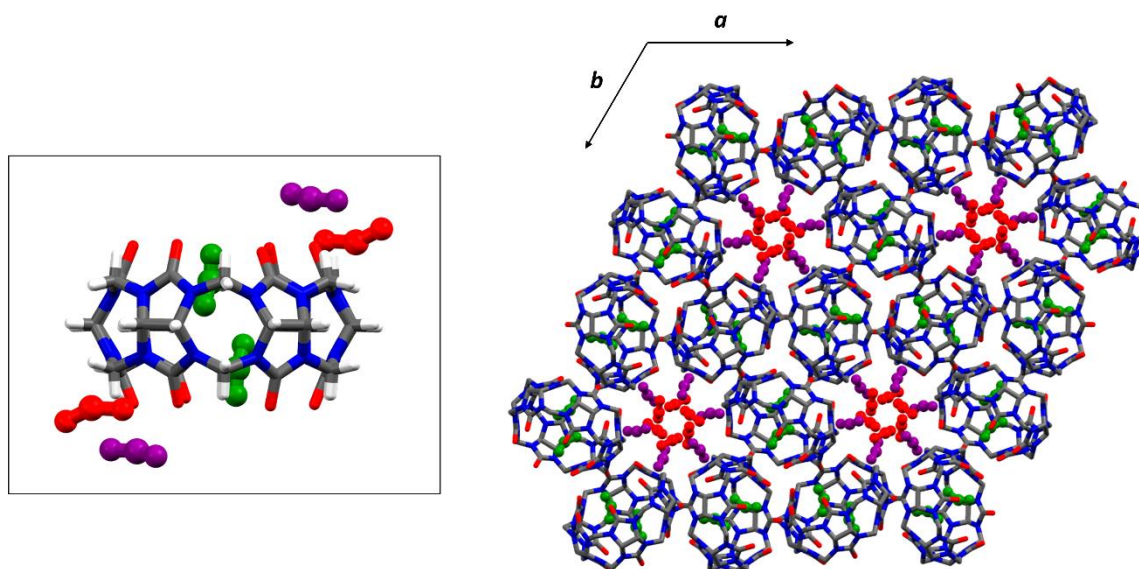


Figure 3. The CO₂ inclusion compound formed by CB[6] captures six CO₂ molecules per CB[6] molecule. The green CO₂ molecules are situated in the intrinsic sorption sites, while the red and purple CO₂ molecules are situated in two separate sorption sites in the 1D channels.²

The porous nature of another member of the cucurbit[n]uril family, CB[8], was also investigated. Octagonal hydrochloride hydrate crystals of CB[8] (**4a**) were grown from a solution of HCl. As in the case of CB[6], the CB[8] molecules are arranged to form a network of interlocked square planar units that are held together by inter-cucurbituril hydrogen bonds. Due to the larger size of CB[8] as compared to CB[6], the macrocyclic cavity of each CB[8] molecule is only partially closed off by the square planar arrangement. As a result, the extrinsic and intrinsic cavities in **4a** are connected to produce a structure with 3D channels

Chapter 6 – Concluding remarks

that are filled with water molecules and chloride anions. Hydrogen bonds and ion-dipole interactions between these guest molecules and the cucurbituril macrocycles keep the 3D architecture of **4a** intact. Consequently, the structure of **4a** collapses during desolvation and a phase transformation to a more stable polycrystalline phase of CB[8] (**4b**) occurs. Since single crystallinity is lost during this process, the crystal structure of **4b** could not be determined. However, volumetric sorption analysis of **4b** indicated that the host framework is porous. CB[8] adsorbs a negligible amount of N_2 and CH_4 , but displays a stepwise uptake and release of CO_2 . Below 24 bar, two molecules of CO_2 are adsorbed per CB[8] molecule, producing a 2:1 (CO_2 : CB[8]) CO_2 inclusion compound. At 24 bar, a gas-induced structural transformation to a new phase of CB[8] (**4c**) occurs. This phase has an increased CO_2 loading capacity and can accommodate 4.50 CO_2 molecules per CB[8] molecule at 50 bar. A large hysteric loop is present in the CO_2 isotherm, indicating that the sample holds on to the CO_2 molecules strongly by means of intermolecular interactions. During desorption, a small step occurs at approximately 2 bar as the phase transforms from **4c** back to a CO_2 inclusion compound of **4b**. When the sample is kept under vacuum for an extended period of time, the original activated phase of **4b** is obtained. CB[8] thus displays a breathing motion during the uptake and release of CO_2 , since the structure expands to accommodate CO_2 during adsorption and contracts to produce the original phase during desorption.

Two mechanisms are proposed for the uptake of CO_2 molecules by CB[8]. The first mechanism assumes that the intrinsic cavities in **4b** are more accessible to CO_2 than the extrinsic cavities, whereas the second mechanism assumes the opposite. In both mechanisms, the force exerted by the CO_2 molecules in the filled cavities is responsible for a structural transformation to a phase with newly exposed extrinsic (first mechanism) or intrinsic (second mechanism) cavities. It is proposed that the second mechanism is most likely to occur, since it does not seem probable that only two CO_2 molecules in the large intrinsic cavities of CB[8] could exert a pressure large enough to induce a structural expansion. Therefore, the structure of **4b** most likely contains accessible extrinsic spaces that are first filled with CO_2 molecules and will allow the structure to expand at a higher pressure.

Chapter 6 – Concluding remarks

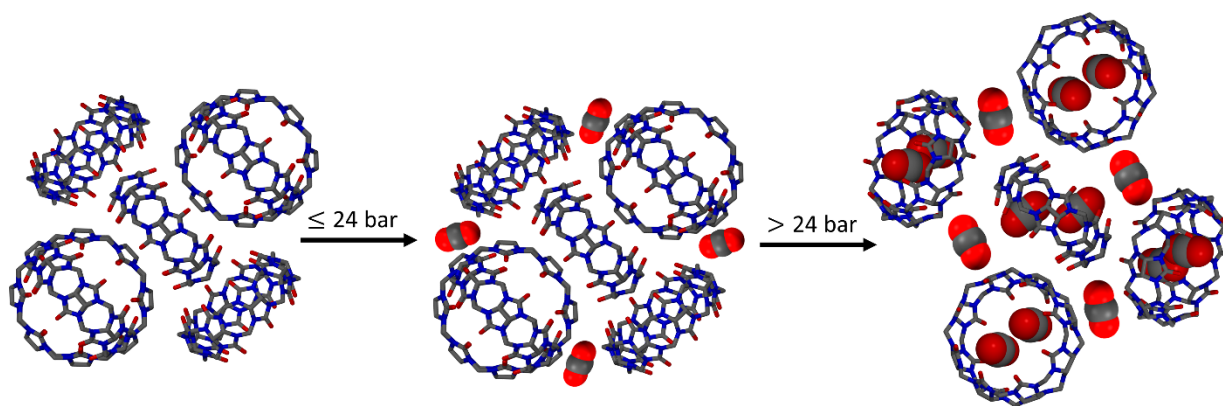


Figure 4. Proposed structures of **4b** and **4c** are used to illustrate a likely mechanism for the uptake of CO₂ by **4b**.

Several approaches were taken in order to maintain the single crystallinity of CB[8] during activation. A new phase of CB[8] (**5**) was grown by recrystallizing CB[8] from a 12 M formic acid solution. Structural analysis of **5** revealed that the CB[8] molecules are arranged to produce a honeycomb network with 1D channels that closely resembles the structure of **3a**. The structure contains water molecules and formate anions in the intrinsic and extrinsic pores. However, when the guest molecules are removed the structure of **5** collapses and single crystallinity is lost.

In another attempt, CdCl₂ was used to introduce uncoordinated cadmium chloride to the crystal structure of CB[8]. When CB[8] is recrystallized from a 3 M HCl solution containing CdCl₂, crystals of **6a** were obtained. In **6a**, the cadmium chloride anions are arranged between CB[8] molecules and lend additional stability to the framework, which prevents the structure from collapsing during desolvation. The structure of **6a** contains 3D channels that are filled with anions and water molecules and it is isoskeletal to **4a**. When **6a** is activated at 413 K under vacuum, the single crystals survive and a phase (**6b**) isoskeletal to **6a** is obtained. Due to the open 3D channels, the sample is extremely hygroscopic and the structure of **6b** contained water molecules.

This study demonstrates the tendency of organic molecules to arrange in a close-packed fashion in the solid state. In the absence of any strong directional interactions such as hydrogen bonds, the molecules tend to pack efficiently to minimize the void space between them. For this reason **1a_o**, which is a van der Waals host, lacks extrinsic cavities and has a much lower CO₂ sorption capacity compared to the highly porous host **3b**, which is held together by hydrogen bonds. When the host framework is held together by non-covalent interactions with surrounding solvent molecules, the host structure often collapses to produce

Chapter 6 – Concluding remarks

a more close-packed structure during activation. This was observed during the phase transformation from **4a** to **4b**. However, due to the large macrocyclic building blocks in **4b**, the host is porous to some extent and is able to adsorb CO₂ in a stepwise fashion.

In future studies, a gas cell should be used to activate a single crystal of **6a** in order to determine the guest free structure. Since the structure of **6a** contains large 3D channels with various possible sites for interactions with CO₂ molecules, it is likely that this host will be able to adsorb a large amount of CO₂. Volumetric sorption analysis can be used to determine the CO₂ adsorption capacity of this host. Furthermore, *in-situ* SCXRD analysis can be used to investigate the host-guest interactions that play a role in CO₂ sorption. Further studies may also include investigations of organic macrocycles similar to the cucurbiturils. The activated hosts should be screened for survival of the activation process and whether they contain sites that would facilitate several host-guest interactions. The study could also be extended to investigate SOFs and COFs with similar attributes.

Chapter 6 – Concluding remarks

REFERENCES

1. (a) Gu, X.; Zhang, L.; Gong, X.; Lau, W. M.; Liu, Z. F. *J. Phys. Chem. B.* **2008**, *112*, 14851; (b) Breite, M. D.; Coz, J. R.; Adams, J. E. *J. Am. Chem. Soc.* **2010**, *132*, 10996.
2. Kim, H.; Kim, Y.; Yoon, M.; Lim, S.; Park, S. M.; Seo, G.; Kim, K. *J. Am. Chem. Soc.* **2010**, *132*, 12200.

Appendix

The supplementary CD contains the following supporting files, tables and videos:

Chapter 3:

- CIF data files and CheckCIF reports of **1a₀**, **1a·CO₂**, **1c·CO₂** and **1b₀**.

Chapter 4:

- CIF data files and CheckCIF reports of **2a**, **3a**, **3b**, **3b'**, **3c** and **3d**.
- Video S1 showing the transformation of **2a** to **2a'**.

Chapter 5:

- CIF data files and CheckCIF reports of **4a**, **5**, **6a** and **6b**.

Table S1. Crystallographic data for **1a_o**, **1a·CO₂**, **1c·CO₂** and **1b_o** at 298 K and 100 K.

	1a_o		1a·CO₂		1c·CO₂	
Molecular formula	C ₄₄ H ₅₆ O ₄	C ₄₄ H ₅₆ O ₄	C _{44.50} H ₅₆ O ₅	C _{44.90} H ₅₆ O ₅	C _{45.44} H ₅₆ O _{6.88}	C _{45.92} H ₅₆ O _{7.84}
Formula weight (g mol ⁻¹)	648.88	648.88	670.89	688.54	712.26	733.38
Temperature (K)	298	100	298	100	298	100
Crystal system	Monoclinic	Monoclinic	Monoclinic	Monoclinic	Tetragonal	Tetragonal
Space group	<i>P</i> 2 ₁ / <i>n</i>	<i>P</i> 2 ₁ / <i>n</i>	<i>P</i> 2 ₁ / <i>n</i>	<i>P</i> 2 ₁ / <i>n</i>	<i>P</i> 4/ <i>n</i>	<i>P</i> 4/ <i>n</i>
<i>a</i> (Å)	12.5955(6)	12.5952(8)	12.5920(2)	12.5483(2)	12.8774(7)	12.7946(8)
<i>b</i> (Å)	26.2720(13)	25.5336(15)	26.2417(4)	25.5433(5)	12.8774(7)	12.7946(8)
<i>c</i> (Å)	12.7254(6)	12.6690(8)	12.7196(2)	12.6380(2)	12.8890(0)	12.6478(15)
α (°)	90	90	90	90	90	90
β (°)	90.3850(10)	90.1100(10)	90.3540(10)	90.0550(10)	90	90
γ (°)	90	90	90	90	90	90
Volume (Å ³)	4210.9(4)	4067.9(4)	4202.93(11)	4050.79(12)	2137.3(2)	2070.5(4)
<i>Z</i>	4	4	4	4	2	2
R _{int}	0.0717	0.0588	0.0609	0.0602	0.3560	0.2250
R1 [<i>F</i> ² >2σ(<i>F</i> ²)]	0.1270	0.0616	0.1342	0.0809	0.1840	0.1642
wR2 (all data)	0.2060	0.1327	0.3050	0.1826	0.3164	0.3151
Goodness of fit	1.044	1.036	1.028	1.033	0.985	1.008

Table S1 continued.

	1b_o	
Molecular formula	C ₄₄ H ₅₆ O ₄	C ₄₄ H ₅₆ O ₄
Formula weight (g mol ⁻¹)	648.88	648.88
Temperature (K)	298	100
Crystal system	Monoclinic	Monoclinic
Space group	<i>P2₁/c</i>	<i>P2₁/c</i>
<i>a</i> (Å)	9.6585(2)	9.5634(10)
<i>b</i> (Å)	30.6383(6)	30.431(30)
<i>c</i> (Å)	13.5943(3)	13.5025(14)
α (°)	90	90
β (°)	109.7840(10)	109.994(2)
γ (°)	90	90
Volume (Å ³)	3785.38(14)	3692.8(7)
<i>Z</i>	4	4
<i>R</i> _{int}	0.0915	0.0597
<i>R</i> ₁ [<i>F</i> ² >2σ(<i>F</i> ²)]	0.1475	0.1512
<i>wR</i> ₂ (all data)	0.1811	0.0822
Goodness of fit	1.072	1.014

Table S2. Crystallographic data for **2a**, **3a**, **3b'**, **3b**, **3c** (at 228 K and 298 K) and **3d**.

	2a	3a	3b'	3b
Molecular formula	C ₃₆ H ₃₆ N ₂₄ O _{35.20} Cl ₈	C ₃₆ H ₃₆ N ₂₄ O ₂₆	C ₃₆ H ₃₆ N ₂₄ O _{13.04}	C ₃₆ H ₃₆ N ₂₄ O _{12.25}
Formula weight (g mol ⁻¹)	1651.69	1220.89	1013.53	1000.89
Temperature (K)	100	298	100	298
Crystal system	Hexagonal	Trigonal	Trigonal	Trigonal
Space group	<i>P6/mmm</i>	<i>R$\bar{3}$</i>	<i>R$\bar{3}$</i>	<i>R$\bar{3}$</i>
<i>a</i> (Å)	14.5025(2)	32.059(8)	31.5521(11)	31.5982(18)
<i>b</i> (Å)	14.5025(6)	32.059(8)	31.5521(11)	31.5982(18)
<i>c</i> (Å)	10.7201(3)	12.502(3)	24.9516(10)	25.1371(15)
α (°)	90	90	90	90
β (°)	90	90	90	90
γ (°)	120	120	120	120
Volume (Å ³)	1952.61(12)	11128(6)	21512.2(17)	21736(3)
Z	1	9	18	18
R _{int}	0.0227	0.1015	0.2568	0.1270
R1 [<i>F</i> ² >2σ(<i>F</i> ²)]	0.1393	0.1551	0.2155	0.1170
wR2 (all data)	0.4435	0.2475	0.2263	0.1320
Goodness of fit	1.034	0.999	1.012	1.019

Table S2 continued.

	3c		3d
Molecular formula	$C_{37.22}H_{36}N_{24}O_{14.44}$	$C_{36.60}H_{36}N_{24}O_{13.20}$	$C_{38.76}H_{36}N_{24}O_{17.52}$
Formula weight (g mol ⁻¹)	1118.35	1023.29	1118.35
Temperature (K)	228	298	298
Crystal system	Trigonal	Trigonal	Trigonal
Space group	$R\bar{3}$	$R\bar{3}$	$R\bar{3}$
<i>a</i> (Å)	31.878(3)	31.816(4)	31.9244(10)
<i>b</i> (Å)	31.878(3)	31.816(4)	31.9244(10)
<i>c</i> (Å)	12.4212(11)	12.4167(10)	12.3993(4)
α (°)	90	90	90
β (°)	90	90	90
γ (°)	120	120	120
Volume (Å ³)	10931(2)	10885(3)	10943.9(8)
Z	9	9	9
R_{int}	0.0981	0.3576	0.1819
$R1 [F^2 > 2\sigma(F^2)]$	0.2059	0.3586	0.2260
$wR2$ (all data)	0.4291	0.5185	0.2926
Goodness of fit	1.311	1.280	1.005

Table S3. Crystallographic data for **4a**, **5**, **6a** and **6b**.

	4a	5	6a	6b
Molecular formula	C ₄₈ H ₆₂ N ₃₂ O ₃₉ Cl ₄	C ₅₃ H ₄₈ N ₃₂ O _{46.46}	C ₄₈ H ₄₈ N ₃₂ O _{35.28} Cd _{1.50} Cl ₁₀	C ₄₈ H ₄₈ N ₃₂ O ₄₂ Cd _{0.50} Cl ₆
Formula weight (g mol ⁻¹)	1853.09	1879.90	2160.76	2014.08
Temperature (K)	298	100	298	298
Crystal system	Tetragonal	Trigonal	Tetragonal	Tetragonal
Space group	<i>I</i> 4 ₁ / <i>a</i>	<i>R</i> $\bar{3}$	<i>I</i> 4 ₁ / <i>a</i>	<i>I</i> 4 ₁ / <i>a</i>
<i>a</i> (Å)	28.059(8)	38.8330(13)	28.069(6)	28.0739(15)
<i>b</i> (Å)	28.059(8)	38.8330(13)	28.069(6)	28.0739(15)
<i>c</i> (Å)	21.887(6)	13.6824(6)	21.386(4)	21.3003(12)
α (°)	90	90	90	90
β (°)	90	90	90	90
γ (°)	90	120	90	90
Volume (Å ³)	17232(11)	17868.8(14)	16850(8)	16788(2)
Z	8	9	8	8
R _{int}	0.1590	0.2166	0.0684	0.1095
R1 [<i>F</i> ² >2σ(<i>F</i> ²)]	0.2519	0.2241	0.1947	0.1995
wR2 (all data)	0.4523	0.3797	0.5656	0.5211
Goodness of fit	1.245	1.145	1.068	1.181